Analysis of hard X-ray emission from selected very high energy γ-ray sources observed with *INTEGRAL*

Dissertation
zur Erlangung des Grades eines
Doktors der Naturwissenschaften
der Fakultät für Mathematik und Physik
der Eberhard-Karls-Universität Tübingen

vorgelegt von

Agnes Irene Dorothee
Hoffmann

aus Solingen

2009

Selbstverlegt von	A. Hoffmann Bruno-Matzke-Str.15, 72770 Reutlingen
Tag der mündlichen Prüfung:	13. November 2009
Dekan:	Prof. Dr. W. Knapp
1. Berichterstatter:	Prof. Dr. A. Santangelo
2. Berichterstatter:	Prof. Dr. K. Werner

ERWEITERTE DEUTSCHE ZUSAMMENFASSUNG

Hoffmann, Agnes

Analyse mit *INTEGRAL* beobachteter harter Röntgenemission ausgewählter Quellen sehr hochenergetischer Gammastrahlung

Die Ära der sehr hochenergetischen Gammastrahlungsastronomie begann vor wenigen Jahren, als die neueste Generation der die Atmosphäre abbildenden Čherenkov Teleskope (Imaging Atmospheric Čherenkov Telescopes, IACT), wie beispielsweise *H.E.S.S.*, ihre Arbeit aufnahm und einzelne TeV-Quellen aufgelöst werden konnten. Durch Beobachtungen in vielen verschiedenen Wellenlängenbereichen können diese Quellen identifiziert werden, woraus sich ergab, daß die entdeckten Quellen Supernovaüberreste und Kerne aktiver Galaxien, aber auch Pulsarwindnebel und einige wenige Doppelsternsysteme sind. Eine der noch offenen und intensiv diskutierten Fragen ist, wie diese Quellen in der Lage sind, Teilchen zu solch hohen Energien zu beschleunigen. Das Verständnis der zu Grunde liegenden Teilchenverteilung und der stattfindenden Beschleunigungsprozesse sowie die Kenntnis über die Strahlungsprozesse, welche die beobachtete Strahlung erzeugen, ist deshalb von entscheidender Bedeutung. Die Beobachtung der harten Röntgenstrahlung kann ein Schlüssel sein, um Informationen über die Teilchenverteilungen und die stattfindenden Prozesse zu erhalten. Wichtig für diese Arbeit sind der TeV und der harte Röntgenbereich. Die Instrumente *H.E.S.S.* und *INTEGRAL*, deren Daten verwendet wurden, werden daher genauer beschrieben.

Der Hauptteil dieser Arbeit ist dem Röntgendoppelsternsystem LS 5039/ RX J1826.2−1450 gewidmet. Dieses System wurde in mehreren Energiebereichen beobachtet. Die Natur des kompakten Objekts ist noch immer unbekannt. Es wurden sowohl ein Mikroquasarsystem als auch ein nicht-akkretierendes Pulsarsystem als möglicher Objekttyp vorgeschlagen. Die beobachtete TeV-Emission moduliert mit der orbitalen Bewegung. Verschiedene Erklärungen für diese Variabilität wurden in den letzten Jahren diskutiert. Die *INTE-*

GRAL-Beobachtungen, die in dieser Arbeit präsentiert werden, liefern neue Informationen, um eine Antwort auf diese Frage zu finden. Darum war der Nachweis einer Detektion im harten Röntgenbereich und die Suche nach einer orbitalen Abhängigkeit erstrebenswert. Da jedoch LS 5039 eine sehr schwache Quelle ist und der Himmelsausschnitt, in dem sie sich befindet, sehr viele weitere Quellen enthält, war, neben einer sehr umsichtigen, nicht dem standardisierten Vorgehen folgenden Auswertung der *INTEGRAL*-Daten, auch eine Gegenprobe mit anderen Analysemethoden erforderlich, um verlässliche Resultate zu erzielen. Wir fanden, daß LS 5039 im harten Röntgenbereich Strahlung emittiert. Für den Energiebereich $25 - 200\,\mathrm{keV}$ konnte eine Flußrate und eine obere Flußgrenze abhängig von der orbitalen Phase bestimmt werden. Für die Phase der unteren Konjunktion wurde zudem ein Spektrum gewonnen, das gut durch ein Potenzgesetz mit einem Photonenindex von $\Gamma = 2.0 \pm 0.2$ beschrieben werden kann. Das wichtigste Ergebnis unserer Analyse ist jedoch, daß die harte Röntgenstrahlung innerhalb eines Umlaufs variiert und daß diese Modulation verhältnismäßig gut mit der TeV-Emission in Phase ist. Obwohl die Ergebnisse der *INTEGRAL*-Analyse keine Entscheidung zwischen dem Mikroquasar- und dem Pulsarszenario zulassen, läßt sich mit ihrer Hilfe die einfache Erklärung, daß die TeV-Variabilität eine Folge reiner Photon-Photon-Absorption sei, ausschließen. Daher diskutieren wir in dieser Arbeit mögliche alternative Erklärungen wie die adiabatische Kühlung von Elektronen als Ursache für die korrelierte Modulation. In diesem Fall ist die Variabilität einfach ein Resultat der orbitalen Bewegung, und der größere Faktor der Modulation im TeV-Energiebereich wird durch zusätzliche Prozesse wie γ-γ-Absorption und die Anisotropie der inverse Comptonstreuung verursacht.

Im zweiten Teil dieser Arbeit wird die $\mathrm{keV} - \mathrm{TeV}$-Verbindung von drei durch Rotation angetriebene Pulsarwindnebel (rotation-powered pulsar wind nebulae, RPWN) untersucht. Die Analyse ist konzentriert auf RPWNs, welche als TeV Plerions entdeckt wurden. Die zwei erzeugten Mosaikbilder beinhalten die Pulsare PSR J0835−4510 (Vela), PSR J1513−5908 (MSH 15−52) und PSR J1420−6048 (Kookaburra). Nur einige wenige Prozent aller mit *INTEGRAL* beobachteten RPWNs wurden als junge Pulsare oder Pulsare mittleren Alters identifiziert. Die Analyse der archivierten *INTEGRAL*-Daten weisen auf eine harte Röntgenemission an der Position von PSR J1420−6048 im "Kookaburra" TeV Plerion G313.3+0.6 hin, zusätzlich zu den schon bekannten *INTEGRAL*-Quellen. Der Pulsar PSR J1420−6048 gehört zu der Klasse der Pulsare mittleren Alters, in welchen der RWPN mit der rückwärts gerichteten Schockfront des Supernovaüberrestes wechselwirkt. Alles in allem deutet

diese Analyse auf einen tieferen Zusammenhang zwischen TeV Plerions und Pulsarwindnebeln, die mit *INTEGRAL* entdeckt wurden, hin.

Den letzten Teil dieser Arbeit widmen wir einer systematischen Analyse des für die Region um LS 5039 erzeugten Mosaikbildes. Auf den ersten Blick erscheint die 3×10^6 s tiefe *INTEGRAL*-Beobachtung zwar nur als Nebenprodukt, es lohnt sich jedoch, diese selbst genauer zu betrachten. Alle bekannten *H.E.S.S.*-Quellen und alle *INTEGRAL*-Quellen, die sich im Gesichtsfeld befinden, werden aufgelistet. Insbesondere zieht aber eine Quelle die Aufmerksamkeit auf sich. Dies ist das akkretierende und pulsierende Neutronensternsystem AX J1820.5−1434. Die Leuchtkraft von AX J1820.5−1434 scheint auch mit den Phasen von LS 5039 zu variieren. Durch die Analyse von RXTE / ASM Daten ergibt sich, daß dies ein Resultat des zufälligen Zusammentreffens zwischen hohen Flußzuständen von AX J1820.5−1434 und des gewählten Phasenintervals der unteren Konjunktion von LS 5039 ist.

ABSTRACT

Hoffmann, Agnes

Analysis of hard X-ray emission from selected very high energy γ-ray sources observed with *INTEGRAL*

A few years ago, the era of very high energy γ-ray astronomy started, when the latest generation of Imaging Atmospheric Čherenkov Telescopes (IACT) like *H.E.S.S.* began to operate and to resolve the sources of TeV emission. Identifications via multi-wavelength studies reveal that the detected sources are supernova remnants and active galactic nuclei, but also pulsar wind nebulae and a few binaries. One widely discussed open question is, how these sources are able to accelerate particles to such high energies. The understanding of the underlying particle distribution, the acceleration processes taking place, and the knowledge of the radiation processes which produce the observed emission, is, therefore, of crucial interest. Observations in the hard X-ray domain can be a key to get information on these particle distributions and processes. Important for this thesis are the TeV and the hard X-ray range. The two instruments, *H.E.S.S.* and *INTEGRAL*, whose data were used, are, therefore, described in detail.

The main part of this thesis is focused on the X-ray binary system LS 5039/ RX J1826.2−1450. It was observed in several energy ranges. The nature of the compact object is still not known, and it was proposed either to be a micro-quasar system or a non-accreting pulsar system. The observed TeV emission is modulated with the orbital cycle. Several explanations for this variability have been discussed in recent years. The observations with *INTEGRAL* presented in this thesis have provided new information to solve this question. Therefore, a search for a detection in the hard X-ray range and for its orbital dependence was worthwhile. Since LS 5039 is a faint source and the sky region where it is located is crowded, a very careful, non-standard handling of the *INTEGRAL* data was necessary, and a cross-checking with other analysis methods was es-

sential to provide reliable results. We found that LS 5039 is emitting in the hard X-ray energy range. A flux rate and an upper flux limit, dependent on orbital phase, were determined for the energy range $25-200\,\mathrm{keV}$. For the inferior conjunction phase, also a spectrum was obtained and found to be well described by a power law with a photon index of $\Gamma = 2.0 \pm 0.2$. Our main result is that the hard X-ray emission is modulated with the orbit and this modulation is comparatively in phase with the TeV emission. Although the results of the *INTEGRAL* analysis are not able to distinguish between the microquasar and the pulsar scenario, they rule out a simple explanation of the TeV variability as a consequence of pure photon-photon absorption. In our work we, therefore, discuss possible alternatives like adiabatic cooling of the electrons as a reason for the correlated modulation. In this case the variability is simply a result of the orbital motion and the larger factor of modulation in the TeV range is caused by additional processes like γ-γ absorption and anisotropic inverse Compton scattering.

In the second part of this thesis, the keV $-$TeV connection of three rotation-powered pulsar wind nebulae (RPWN) is studied. The analysis is focussed on RPWN which have been detected as TeV plerions and two mosaics are created which include PSR J0835$-$4510 (Vela), PSR J1513$-$5908 (MSH 15$-$52) and PSR J1420$-$6048 (Kookaburra). Only a few per cent of the RPWN observed by *INTEGRAL* have been identified with young or middle-aged pulsars. The analysis of archival *INTEGRAL* data, in addition to the already known *INTEGRAL* sources, reveals an evidence of hard X-ray emission at the position of PSR J1420$-$6048 from the "Kookaburra" TeV plerion G313.3+0.6. The pulsar PSR J1420$-$6048 belongs to the class of middle-aged pulsars where the RPWN interacts with the reverse shock of the supernova remnant. Altogether, this analysis indicates a deeper link between these TeV plerions and *INTEGRAL* detected pulsar wind nebulae.

The last part of the thesis is devoted to a systematic analysis of the mosaic obtained for the region around LS 5039. In the first place only seen as a byproduct, the 3×10^6 s deep *INTEGRAL* observation is worthwhile to be studied on its own. All public *H.E.S.S.* sources and all *INTEGRAL* sources located in the field of view are listed. One source in particular attracted our attention. This is the accreting pulsating neutron star system AX J1820.5$-$1434. The luminosity of this source seems to vary in phase with LS 5039. By analysing the RXTE / ASM data, this is found to be a result of a coincidence between high flux states of AX J1820.5$-$1434 and the inferior conjunction phase interval chosen for LS 5039.

TO MY PARENTS
who assisted me to let my dream become true.

TO MY 'TWIN COUSIN' BERND
who can't live his dream anymore.

CONTENTS

List of Tables xv
List of Figures xvii

1 Introduction 1
1.1 Thesis outline 2

2 X-ray and TeV binaries 5
2.1 Basics of single star evolution 5
2.2 High-energy range of the electromagnetic spectrum 8
2.2.1 X-ray band 10
2.2.2 γ-ray band 11
2.3 X-ray binaries 13
2.3.1 Accretion processes 13
2.3.2 High mass X-ray binaries – HMXRBs 16
2.3.3 Low mass X-ray binaries – LMXRBs 16
2.3.4 Radio-emitting X-ray binaries – REXRBs 18
2.4 Evolution of binary systems 18
2.5 TeV binaries 22

3 Astrophysical processes 27
3.1 Acceleration processes 27
3.1.1 Acceleration in shock fronts and clouds – Fermi mechanism first order 27
3.2 Radiation processes 30
3.2.1 Blackbody radiation 31
3.2.2 Synchrotron radiation 31
3.2.3 Synchrotron self-absorption 34
3.2.4 Inverse Compton scattering 35
3.2.5 Bremsstrahlung 38
3.2.6 Pair production 40

3.2.7 Electron-positron annihilation 41
3.2.8 Nucleon-nucleon interactions and inelastic p-p collisions 42
3.2.9 Decay of π-mesons 42
3.2.10 Nuclear processes 43
3.2.11 Photon-hadron interactions 43
3.3 Electron energy losses and cooling time 44

4 γ-ray instruments – *H.E.S.S.* and *INTEGRAL* 47
4.1 An historical recap of high energy astronomy and instrumentation 47
4.2 *H.E.S.S.* 49
4.2.1 The Imaging Air Čherenkov Technique 49
4.2.2 The telescope layout 56
4.2.3 Operating mode 57
4.2.4 Results – A new observable window to the universe . . 58
4.3 *INTEGRAL* 60
4.3.1 The satellite 60
4.3.2 Analysis method and coded mask technique 62

5 A TeV binary – LS 5039 69
5.1 The System LS 5039 69
5.2 Multi-wavelength observations 74

6 *INTEGRAL* Observations of LS 5039 89
6.1 Data selection 89
6.2 Analysis 90

7 Results and Interpretation 99
7.1 Results of the analysis of the *INTEGRAL* observation of LS 5039 99
7.2 Results of the analysis of *Suzaku* observations 99
7.3 Interpretation 102
7.3.1 Accretion mechanism in LS 5039 102
7.3.2 Possible production mechanisms of TeV γ-ray emission in LS 5039 105
7.3.3 Neutron star or black hole? 108
7.3.4 Microquasar versus non-accreting pulsar 108
7.3.5 Possible production sites of TeV γ-ray emission in LS 5039 111

7.3.6 The keV– TeV connection in LS 5039 112
7.4 Conclusions from *INTEGRAL* observations 114

8 TeV plerions **117**
8.1 Rotation-powered pulsar wind nebulae (RPWN) 117
8.1.1 VHE γ-ray / X-ray connection in RPWN 118
8.2 Analysis of selected RPWN 120
8.2.1 PSR J1513−5908 (MSH 15−52) 120
8.2.2 PSR J0835−4510 (Vela) 120
8.2.3 PSR J1420−6048 (Kookaburra) 121
8.3 Results 125
8.4 Conclusions 125

9 Other sources in the FoV **127**
9.1 A very crowded field 127
9.1.1 *H.E.S.S.* sources 127
9.1.2 *INTEGRAL* sources 128
9.2 AX J1820.5−1434 136

10 Summary & outlook **137**
10.1 LS 5039 137
10.2 TeV plerions 139
10.3 AX J1820.5−1434 140
Bibliography 141
Acknowledgments 149
Curriculum vitae 151

LIST OF TABLES

2.1 The currently confirmed TeV binary systems 26

5.1 Parameters of the binary system LS 5039 72

6.1 Summary of selected and analysed *INTEGRAL* data 90

8.1 Parameters of pulsars seen by *INTEGRAL* and *H.E.S.S.* . . . 126

9.1 References of *H.E.S.S.* sources 128
9.2 *H.E.S.S.* sources in the explored *INTEGRAL* FoV 130
9.3 *INTEGRAL* sources in the explored *INTEGRAL* FoV 132
9.4 Position of detected *INTEGRAL* sources in analysed mosaic . 134
9.5 Detected *INTEGRAL* sources in FoV - count rates and significances 135

LIST OF FIGURES

2.1 Energy ranges of the electromagnetic spectrum 8
2.2 Electromagnetic spectrum and the absorption in the Earth's atmosphere 9
2.3 Roche potential 15
2.4 Evolution of a high-mass X-ray binary 20

3.1 Synchrotron radiation spectrum 34
3.2 Compton scattering process 35
3.3 Inverse Compton spectrum 37
3.4 Dependence of inverse Compton spectrum on viewing angle . 38
3.5 Energy loss timescales (cooling times) for electrons 46

4.1 Čherenkov light emission principle 51
4.2 Čherenkov light emission spectrum 53
4.3 Image reconstruction for Air shower telescopes 54
4.4 Imaging Čherenkov technique 55
4.5 *H.E.S.S.* telescopes 56
4.6 *H.E.S.S.* survey of the inner Galaxy 59
4.7 *INTEGRAL* satellite 61
4.8 Coded mask technique 63

5.1 Sketch of the system LS 5039 70
5.2 Radio observation of LS 5039 76
5.3 Orbital dependence in soft X-rays of LS 5039 83
5.4 VHE γ-ray observation of LS 5039 with *H.E.S.S.* 86
5.5 Spectra of LS 5039 observed with *H.E.S.S.* 87
5.6 Broad-band spectral energy distribution for LS 5039 88

6.1 *INTEGRAL* image of LS 5039 observation 93
6.2 Power spectrum of *INTEGRAL* light curve 95

6.3 Orbital dependence on hard X-rays compared to VHE γ-rays . 96
6.4 Hard X-ray spectrum for LS 5039 at the inferior conjunction . 97

7.1 Hard X-ray flux variability of LS 5039 observed with *Suzaku* . 101
7.2 Microquasar and non-accreting young pulsar model 109

8.1 Sketch of a rotation-powered pulsar wind nebula 119
8.2 PSR J1513−5908 seen with *INTEGRAL* 122
8.3 PSR J1513−5908 seen with *H.E.S.S.* 122
8.4 Vela pulsar seen with *INTEGRAL* 123
8.5 PSR J0835−4510 seen with *H.E.S.S.* 123
8.6 Kookaburra region in $20 - 40\,\mathrm{keV}$ energy range 124
8.7 Kookaburra region seen with *H.E.S.S.* 124

9.1 *H.E.S.S.* sources in the *INTEGRAL* FoV of the observation of LS 5039 129
9.2 *INTEGRAL* sources in the *INTEGRAL* FoV of the observation of LS 5039 131
9.3 RXTE ASM light curve of AX J1820.5−1434 136

CHAPTER 1

Introduction

There are exciting laboratories of yet unknown physical properties out there in the universe. In contrast to laboratories on Earth, where the physicist can influence the conditions, the physical properties of galactic and extragalactic sources and their specific circumstances can only be observed. Nearly the only way to get information from these extraordinary environments is through electromagnetic radiation. It is worth mentioning that also particles emitted by these sources can reach us, yet particle astrophysics is still in its infancy. Charged particles (i. e. electrons and protons) can be deflected on the way by magnetic and electric fields and hence lose directional information. When penetrating the Earth's atmosphere, all massive particles (also uncharged ones like neutrons) cannot continue their way without interactions like scattering processes. In contrast, neutrinos can reach the Earth without interacting with the atmosphere or with particles and fields on their way to us, but this also means that they are prevented from being easily detected. The cross section of interaction of neutrinos with matter is too small. So the classical and deeper information from stars, galaxies, and other radiation emitting regions, in other words from celestial laboratories, is carried by photons.

Lower energetic photons, for instance at optical wavelengths, are mainly produced in stars, which means in thermal environments. The hottest objects emit in the keV energy range. For even more energetic photons, non-thermal environments and accelerators are necessary. Here particles or cosmic rays can be accelerated to energies up to $10^{20}\,\mathrm{eV}$. Information on location, nature, and efficiency of these extreme acceleration regions is carried by photons with energies of keV or higher, i. e. of X-rays, γ-rays, and very high energy γ-rays. X-rays are usually produced via synchrotron radiation or inverse Compton scattering due to electrons. But, besides this leptonic induced radiation, also radiation

caused by hadrons, mainly protons, can be emitted from such regions. While for X-rays the radiation processes can be revealed relatively straightforwardly, the situation changes for very high energy γ-rays. The determination and classification of the responsible radiation process is not easy, because several competing processes can dominate in this energy domain or even take place simultaneously. Some sources observed in the very high energy γ-ray range emit also in the hard X-ray/soft γ-ray range. The connection between keV and TeV ranges can be a key to decide which processes are present in a specific source and can provide information on the underlying particle distribution. In this thesis, we analyse the *INTEGRAL* emission of some specific TeV sources. Our main objects are LS 5039, a very challenging X-ray binary, and several pulsar wind nebulae.

1.1 Thesis outline

Chapter 2 gives an introduction to the electromagnetic spectrum, in particular the high energy ranges of X-rays, γ-rays, and very high energy γ-rays. Different kinds of accretion processes and several types of X-ray binaries are introduced and their evolution is described. This chapter closes with a presentation of the currently known TeV binaries.

In Chapter 3 several astrophysical processes are summarised. First, the acceleration processes in shock fronts and clouds, i. e. the Fermi acceleration mechanism of first order. Second, the basics of several leptonic and hadronic radiation processes are presented. These are blackbody radiation, synchrotron radiation and synchrotron self-absorption, inverse Compton scattering, bremsstrahlung, pair production, electron-positron annihilation, nucleon-nucleon interactions and inelastic p-p collisions, the decay of π-mesons, nuclear processes, and photon-hadron interactions. At the end of this chapter follows an overview on electron energy losses and of cooling times.

In Chapter 4, a description of the instruments important for this thesis and a recap of high energy astronomy and instrumentation is given. This is followed by a description of the Imaging Air Čherenkov Telescope *H.E.S.S.* and a short summary of the new observable window to the universe opened by this kind of instruments. An overview of the γ-ray satellite *INTEGRAL* follows, including, furthermore, a detailed depiction of the analyses procedure of *INTEGRAL ISGRI*.

The main part of the thesis (next three chapters) are dedicated to the TeV binary LS 5039. In Chapter 5, the system itself is presented, and an overview of the multi-wavelength observations performed for this source is provided. The *INTEGRAL* observation we analysed, the challenges we needed to overcome, and the results of the *INTEGRAL* analysis are given in Chapter 6. An interpretation of the results and the discussion of the source is then given in Chapter 7.

In Chapter 8, another type of sources, the rotation-powered pulsar wind nebulae, and the keV $-$TeV connection, which occurs in these sources, are presented.

The last Chapter 9 presents the complete sky region which we have explored. The *H.E.S.S.* and *INTEGRAL* sources are listed. We have a closer look at one single source, AX J1820.5$-$1434, at the end of this chapter.

Finally, a summary and outlook are given in Chapter 10.

CHAPTER 2

X-ray and TeV binaries

2.1 Basics of single star evolution

In this section, a concise overview of stellar evolution is given, introducing those terms and definitions that are important in this thesis. More details can be found in most good astrophysics textbooks, for example in Unsöld & Baschek (1999).

The evolution of a star can be traced by the position of the star in the Hertzsprung-Russell diagram. This diagram is constructed by measuring the same properties for all stars and plotting them against each other: the luminosity of the star is plotted on the y-axis, while surface temperature or spectral type is plotted on the x-axis. During its life, a star migrates through the diagram.

The origin of every star is a cloud of interstellar matter that collapses due to its own gravitational attraction. If the central temperature and density reaches specific values – the temperature has to be about $10^7\,\mathrm{K}$ or $1\,\mathrm{keV}$, the density about $10^{26}\,\mathrm{cm}^{-3}$ – nucleosynthesis starts, and the newborn star produces energy via hydrogen burning. In the Hertzsprung-Russell diagram, stars burning hydrogen are arranged in a diagonal line, called the main sequence. This line starts at high luminosities and high temperatures (these are massive, bright, blue stars of spectral type O and B) and ends at low luminosities and low temperatures (these are the not very massive, faint and red stars of spectral type K and M). This is also simultaneously a ranking from high masses and high surface temperatures to low masses and cold surface temperatures, so that the newly formed, young, main-sequence star is arranged on this line due to its mass.

Henceforward, evolution of the star depends on its mass. When the fuel in the core runs short the burning zone shifts to a shell. Subsequent and likewise

to hydrogen burning are helium burning, carbon and nitrogen burning, silicon burning etc.[1] starting in the core and later shifting to energy producing shells around the core. The burning ends, when the products of burning are the heaviest elements that can be produced by fusion. These are iron and nickel isotopes. The final stage of a star also depends on its mass and starts when there is no longer sufficient nuclear fuel in the core. In principle, because the radiation pressure can no longer balance the gravitational pressure, the star begins to contract under its own weight. The final stages a star can end up in can be divided into three types, depending on the mass.

A low mass star will finally become a white dwarf (WD) that has a mass lower than $1.44\,\mathrm{M}_\odot$, which is the so-called Chandrasekhar limit. The main-sequence star slowly expands and while it evolves into a red giant, it ejects large amounts of matter into the interstellar space. A planetary nebula is constituted. The remaining core of the star, the subsequent white dwarf, is stable, because the degenerate electron gas pressure balances the gravitational force.

When the mass exceeds the Chandrasekhar limit, protons and electrons in the core are turned into neutrons. This means, that a star with a core mass between $1.44\,\mathrm{M}_\odot$ and about $3\,\mathrm{M}_\odot$ (Oppenheimer-Volkoff limit) has another destiny. When the silicon burning is shifted to a shell, an iron/nickel core remains. Hence, no other elements can be produced by fusion, the star collapses, because the outward directed pressure generated by the preceding nuclear reactions vanishes abruptly. A supernova explosion takes place. This spectacular event blows material into the surroundings and produces elements beyond iron due to neutron-capture.[2] Supernovae are efficient sources of high neutrino fluxes. If the neutron-degenerate gas pressure can balance the gravitational force, a neutron star (NS) is formed. The matter in a NS has a very high density, $10^{11} - 2.5 \times 10^{12}\,\mathrm{kg\,cm^{-3}}$.

If the collapsing mass is larger than the limit of about $3\,\mathrm{M}_\odot$, the core continues to collapse and nothing can stop it. A black hole (BH)[3] is formed. These objects can be characterised by only three properties: mass, charge and angular momentum.

Amongst the neutron stars are some with extremely strong magnetic fields up to 10^{15} G which are called magnetars (Harding & Lai 2006). The magnetic

[1] The enabled burning processes depend on the mass of the star.

[2] Two different neutron-capture processes can be distinguish, the rapid r-process and the slow s-process.

[3] By theoretical definition this is an object, which is infinitely small and infinitely dense, in other words a singularity in space-time.

fields of NSs in accreting X-ray binaries are lower and range from about 10^8 G up to 10^{13} G. It is assumed that the high magnetic fields are intensified when the star collapses and a medium magnetic field of the precursor increases to the observed high values (see Harding & Lai 2006, and references therein)

In strong magnetised systems so-called jets can be observed. This term was defined for extragalactic sources by Bridle & Perley (1984) for an ejecta that is collimated to a beam with an opening angle less than $15°$. Mirabel & Rodríguez (1999) transferred this term to the equivalent phenomenon in Galactic X-ray binaries. Up to now it is an open question, how the collimation of the jet and the acceleration of particles in the jets are working, but yet the presence of collimated jets is associated with an existence of an accretion disc (Mirabel & Rodríguez 1999). If in addition the magnetic poles are not arranged at the rotational axis, an observer sees only short flashes, when the beam of the focused emitted radiation is adjusted into the direction of the observer. The object appears as a pulsar. The observed pulse period correlates with the spin period of the pulsar. These periods range between $\sim 1\,\mathrm{ms}$ and $\sim 10\,000\,\mathrm{s}$ (Liu et al. 2006).[4]

One can distinguish two main types of supernova remnants: shell type Supernova remnants and plerions. In the first type, the remaining NS clears its surroundings totally. The second type are plerions, which are a kind of filled shells. They are also called pulsar wind nebulae or Crab-like remnants, because the most famous exponent and prototype is the Crab nebula. Pulsar wind nebulae (PWN) are often found inside larger shells, material ejected from the late-type progenitor star. The powering source of such plerions is believed to be an active rotation-powered pulsar that blows out jets of very fast moving material. The nebula emits synchrotron radiation generated by the relativistic wind of particles in the strong magnetic field.

When the wind of particles interacts with the surroundings and is broken down to sub-relativistic speed, a shock front can be formed. These shocks are sites where particle acceleration can take place (see Section 3.1).

[4]One of the fastest rotating neutron stars is SAX J1808.4−3658 with a spin period of $2.5\,\mathrm{ms}$ (Kretschmar et al. 2004). 2S0114+65 is one of few very slow rotating pulsars with a spin period of $2.65\,\mathrm{h}$ (Farrell et al. 2008).

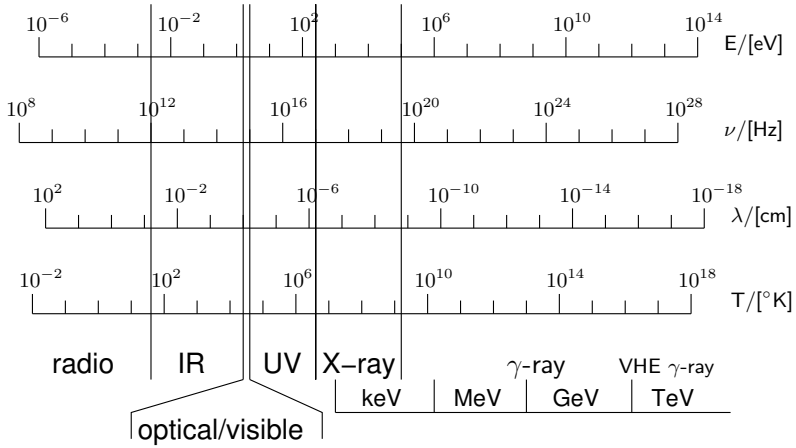

Figure 2.1: The energy ranges of the electromagnetic spectrum. The domains are often not clearly defined, i. e. the photons in the keV/ MeV range are called hard X-rays or soft γ-rays, depending on the observational range compared with. Adapted from Grupen (2000).

2.2 High-energy range of the electromagnetic spectrum

The observable electromagnetic spectrum ranges from radio wavelengths up to very high energies (VHE) in the TeV energy range, that is 21 decades.[5] Some energy ranges are defined in relatively strict limits, others are almost "open". Thus one talks about optical astronomy when observing photons in the wavelength range of $400 - 750\,\mathrm{nm}$, while e. g. the γ-ray domain has no upper energy limit.[6] Figure 2.1 shows the main parts of the electromagnetic spectrum

[5] In astronomy it is still usual to work with cgs units instead of SI units. Depending on the energy range astrophysicists working in, the energy of electromagnetic waves is given in Hertz (radio astronomy), Ångstrøm or nm (optical astronomy) or in electron volt, eV (X-ray to VHE γ-ray astronomy). The conversion factor is $1\,\mathrm{eV} = 1.60217646 \times 10^{-19}$ J and $1\,\mathrm{TeV} = 10^{12}\,\mathrm{eV}$.

[6] Sometimes this can cause confusion, because e. g. photons observed in the energy range of about $E \sim 20 - 300$ keV are called *γ-rays* by an observer dealing usually with data from an X-ray telescope like *XMM-Newton* observing in the energy range $0.3 - 10$ keV, while a scientist working with *H.E.S.S.* data would prefer to talk about the same *INTEGRAL* data as *hard X-rays*. The correct distinction would be to talk about X-rays in the keV energy range and to differ the γ-ray domain into MeV, GeV, and TeV γ-rays. Nevertheless, *INTEGRAL* then would still be a hard X-ray / soft γ-ray instrument. In nuclear physics, the X- and γ-ray ranges are defined by the gener-

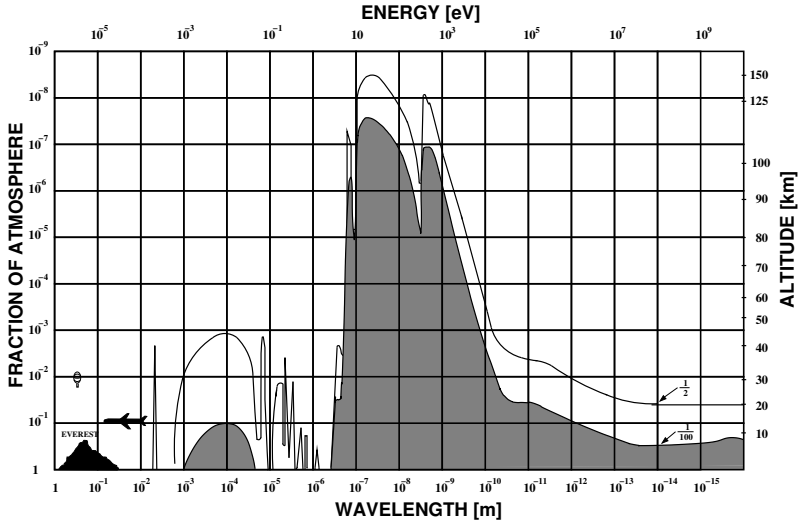

Figure 2.2: The electromagnetic spectrum and the absorption in the Earth's atmosphere. Only two observational windows are open at the Earth's surface, the radio and the optical energy ranges. Figure from Giacconi et al. (1968).

from radio to very high energy γ-rays.

For observational astronomy, the Earth's atmosphere is a problem, because only two observational windows are open through the atmosphere, the optical and the radio energy band. Figure 2.2 shows the absorption coefficient of the Earth's atmosphere depending on wavelength. X-rays and γ-rays are absorbed in the atmosphere. Therefore it is necessary to go into space or at least to the upper layers of the atmosphere to observe the sky in these energy ranges. For energies larger than GeV, the fluxes decrease rapidly and become too small to be detected with current satellites and with feasible satellite detector volume. But the photons have energies high enough to initiate air showers. Thus the Earth's atmosphere can be used as a detector. This is the case of the Imaging Atmospheric Čherenkov Telescopes. With the use of this successful technique,

ating processes. De-excitation transitions in the atomic shell induce the emission of X-rays, while γ-rays occur when the atomic nucleus is transformed. The X-ray/γ-ray dividing line induced with this definition is $E \sim 100$ keV.

the relatively young area of VHE-astronomy began to rise.

In the following paragraphs, the energy ranges relevant to this thesis are discussed separately, especially to give an overview of the observational techniques. The observational techniques of the two telescopes *H.E.S.S.* and *INTEGRAL* are described in Chapter 4 in detail.

2.2.1 X-ray band

Detection mechanism

The reflectivity of X-rays and γ-rays requires new techniques to build imaging telescopes that could collect and focus high energy photons. Although it is complicated to construct X-ray imaging devices, due to the properties of reflectivity[7] of X-rays, nowadays there are three different and successful approaches to build an X-ray telescope. All three solutions are on board actually operating satellites. The three different methods are:

1. Collimator technique:
   This technique is based on the tight constriction of the observed field of view (about 1° in the case of RXTE) and a scanning across the sky to image a sky region. Therefore the detector needs not to be sensitive in position. This technique is used on board the satellite RXTE, which operates in an energy range from 2 to $250\,\mathrm{keV}$. For a description see e. g. Rothschild et al. (1998).

2. Coded mask technique:
   The basis of this technique is the principle of a pinhole camera. The instruments on board the satellite *INTEGRAL*, which observe in the energy range $15\,\mathrm{keV} - 10\,\mathrm{MeV}$, use this technique (Winkler et al. 2003).

3. Wolter telescopes:
   X-rays with energies below $15\,\mathrm{keV}$ are reflected by grazing incidence. A combination of mirrors with paraboloidal and hyperboloidal surfaces (Wolter 1952a,b) is necessary to focus them. So-called Wolter telescopes, e. g. on board the satellites *XMM-Newton* and *Chandra*,

[7] X-ray and γ-rays are absorbed by conventional mirrors used in the optical energy range. Soft X-rays with photon energies below $15\,\mathrm{keV}$, can be reflected by grazing incidence.

are such thin combined mirrors with decreasing diameter stacked into each other.

Many different types of detectors can be used to detect X-rays. For example, crystal spectrometer, proportional counter, photomultiplier, semiconductors or X-ray Charge-Coupled Devices (CCD) are in use. The detectors on board the current X-ray satellites are able to detect single X-ray photons and determine their energy and origin direction. The main instrument for this thesis is the hard X-ray/soft γ-ray telescope *IBIS* on board the *INTEGRAL* satellite. The imaging method is based on the coded-mask technique.

Sources of X-rays

Celestial sources of X-rays are stars, pulsars, binaries, supernova remnants, galaxies, galaxy clusters – all environments where hot plasmas exist or particles are accelerated to high energies. X-rays are generated through several production mechanisms, e. g. by thermal black body radiation, synchrotron radiation, bremsstrahlung, and by the inverse Compton effect. A detailed overview of these production mechanisms is given in Chapter 3.

2.2.2 γ-ray band

Thermal radiation reaches only under extreme conditions, energies of keV or higher. Nevertheless, particles and photons of higher energies as well as of non-thermal nature can be observed in the universe. To know more about sources and acceleration mechanisms for such very high energetic particles is currently a hot topic in astronomy. Theoretical considerations as well as observational identifications are necessary to study and understand the extreme particle accelerators in the universe. In addition, the propagation and interactions of non-thermal populations of particles, as well as the interplay between cosmic rays and magnetic fields, are important to understand the evolution of star populations, galaxies and the universe.

The acceleration of particles is a result of different mechanisms (see Section 3.1). High energetic photons are almost always secondary products of the cosmic accelerators, but can be produced by various mechanisms (see Section 3.2). Photons as uncharged particles have the advantage compared to charged particles like protons or electrons, because they do not lose information about their direction when propagating from the site of generation through

the universe towards the Earth and their detection.[8] Details on the detection methods of γ- and VHE γ-rays are given in Chapter 4.

Sources of γ-rays and VHE γ-rays

On one hand, the γ-ray sky at energies higher than $100\,\mathrm{MeV}$ shows a diffuse emission in the Galactic plane. This emission is generated by the interaction of cosmic rays with the interstellar medium. On the other hand, several point sources can be determined. The Galactic sources are identified as pulsars, supernova remnants and binaries (e. g. Crab pulsar, Vela region, LS 5039), whereas the extragalactic sources are blazars and AGNs (e. g. 3C 279, Mkn 421). Additional sources of γ- and VHE γ-rays are Gamma-Ray bursts (GRB), whose origin is not definitely solved yet, but which are thought to be supernovae of very massive stars. The explosion is accompanied by the generation of a black hole and the accretion disc around the black hole and the formation of a jet, which permeates the layers of the former stellar surface and is observed as a short lasting[9] γ-ray flash.

Production mechanism of γ-rays and VHE γ-rays

As already mentioned, in the VHE γ-ray band several radiation processes can be responsible for the observational features. Sometimes two or more radiation processes contribute to the same energy interval, and it is not clear which of these processes dominates. To identify unambiguously the production mechanism of the γ-rays observed in a specific source, one needs to know the characteristic features of the relevant processes and their relationship to each other. γ-rays are produced via synchrotron radiation, bremsstrahlung, inverse Compton effect, π^0 decay, annihilation of matter/antimatter, and nuclear transitions. These production mechanisms are described in Chapter 3.

[8] That is also true for neutrinos, but neutrinos are much more difficult to detect due to their small cross section.

[9] GRB flashes last about a few seconds and are followed by an afterglow in X-rays which lasts about $10^6\,\mathrm{s} \approx 10\,\mathrm{d}$. Although these GRBs are short lasting, they are called 'long-duration' γ-ray bursts, to distinguish them from the 'short-duration' γ-ray bursts, which last between milliseconds and two seconds.

2.3 X-ray binaries

Up to 50% of all stars in the night sky occur as binaries or multiple systems (Karttunen et al. 2007). A subclass of all binaries are the so-called close binary systems, where the two components are in a close orbit around the barycentre of the system. Among these binaries, there are some which emit in the X-ray energy range, called X-ray binaries (XRBs). XRBs consist of a NS or BH as compact object and a common companion star, often a main-sequence star. Although, up to now, about 250 X-ray binaries are known in our Galaxy (Aharonian 2004; Rosswog & Brüggen 2007), only a few of them contain a BH. Since BHs and NSs are products of supernovae (Section 2.1), the remaining binaries need to survive the explosion. This catastrophic event can destroy the entire system or at least eject the whole binary system out of the Galactic plane (so-called runaway systems). Two types of X-ray binaries are usually defined: Low-mass X-ray binaries (LMXRBs) and High mass X-ray binaries (HMXRBs).

2.3.1 Accretion processes

Accretion of matter is one of the most effective energy producing processes in astronomy. Gravitational energy is set free and converted into radiation. Regarding the accretion phenomena in close binaries, it is seen as an exchange of matter. This exchange is basically caused by the evolution of a single component (Section 2.1).

When describing accretion in binaries, one should have a closer look at two parts of the system. First the material ejection: The mass loss of the companion star depends on the spectral type, the evolutionary state and also on the ratio of masses of the two binary components. Between the two components of an XRB, mass transfer is taking place (Rosswog & Brüggen 2007). The entire X-ray emission is typically dominated by the X-ray emission of the compact object, originating in the accretion of matter. Three main scenarios can be distinguished. The criterion is the way the compact object of the X-ray binary accretes matter: Roche-lobe overflow and formation of an accretion disc (e. g. Her X-1), accretion from a high velocity wind of an early type star (e. g. Vela X-1) or accretion from an extended low-velocity envelope around a Be star (e. g. A0535+26).

Roche-lobe overflow

Figure 2.3 shows the equipotential surfaces of a close binary and is called Roche potential. The largest closed Roche potential surface encloses the Roche volume. The Roche volume also defines the largest volume in the binary configuration. There are five points of equilibrium in a Roche potential, called the Lagrangian points, where the gravitational and the centrifugal forces of both binary components balance each other. The one exactly in between the two stars is the inner Lagrangian point L_1 and is very important. Because, if the donor star fills its Roche volume, which is the volume inside the Roche surface, matter can be transferred via the L_1, forming an accretion stream towards the compact object. In general, systems which undergo Roche-lobe overflow can be discovered on the basis of the large luminosities in the X-ray energy range and typical emission line features they show in the optical wavelength range (McSwain & Gies 2002).

Wind accretion

If on the other hand the donor star has a strong particle wind the compact object can capture a part of the matter transferred via the wind. The luminosity a wind accreting HMXRB can reach depends on the parameters of the system, like the system separation, the mass-loss rate, the velocity of the wind, and the mass of the accretor (McSwain & Gies 2002). One relevant parameter that determines the fraction of stellar wind finally captured by the compact object, is the speed of motion of the compact object relative to the velocity of the wind (Reig et al. 2003). Spherically symmetric Bondi-Hoyle accretion shows typical features in observations, like a rather sharp increase of the X-ray flux at the periastron passage.

Accretion in Be/X-ray binaries

Be stars are fast rotating stars of spectral type B that are forming a circumstellar equatorial disc. In Be/X-Ray binaries, the compact object orbits the massive companion in an eccentric orbit. Around periastron, the compact object enters into the low velocity and high density Be envelope and captures the material.

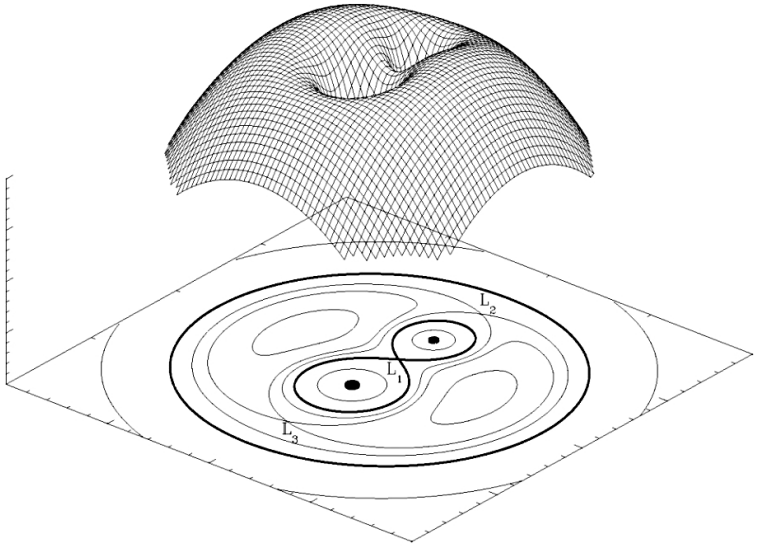

Figure 2.3: The Roche potential. The gravitational and the centrifugal forces of the binary components balancing each other at the equipotential surfaces. L_1, L_2 and L_3 are the Lagrangian points, points of equilibrium in the Roche potential. Roche-lobe overflow takes place via the inner Lagrangian point, L_1. The figure is taken from an online lecture script provided by Pennsylvania State University `www.e-education.psu.edu/astro801/content/l6_p6.html`.

Even though Bondi-Hoyle accretion[10] (Bondi & Hoyle 1944; Bondi 1952) is very sensitive to the properties of the system, which are the relative velocity of the orbiting compact object with respect to the circumstellar material and the velocity and density of the Be envelope, this accretion mechanism is not a rare phenomenon. Observations reveal that the conditions in Be/X-ray binaries are nearly ideal for accretion. The majority of the known HMXRBs are Be/X-ray systems.

The second interesting region in the close binary systems is the region where

[10]The simplest spherically symmetric model of accretion was introduced by Bondi & Hoyle (1944) and is, therefore, called Bondi-Hoyle accretion.

the material falls onto the compact object. Here one needs to distinguish between four different phenomena, depending on the mass accretion rate and the magnetic field strength of the compact object. Due to the angular momentum of the accreted plasma around the compact object, an accretion disc can be formed. This is observable as a strong blue continuum or optical emission lines in the spectra. The disc is generated, if the mass accretion rate is high enough. However, if the magnetic field strength of the compact object is high, the matter can connect to the magnetic field lines and is accreted directly to the vicinity of the magnetic poles. When falling onto the surface of a neutron star, the matter can form shocks, is heated up, and radiation in the X-ray energy range is emitted.

2.3.2 High mass X-ray binaries – HMXRBs

The donor star of a HMXRB is a young, optically bright and massive O or B star with a mass $M_\star > 10\,\mathrm{M}_\odot$ (Unsöld & Baschek 1999). These stars have strong winds. The systems are located in star-forming regions, in particular close to the spiral arms in the Galactic plane (Rosswog & Brüggen 2007). The NSs in these systems have strong magnetic fields ($B_{\mathrm{NS}} = 10^{12} - 10^{13}$ G), which have strong influence on the inflowing matter. The matter is diverted along the magnetic field lines and crashes onto the NS at the magnetic poles. The temperature at the poles increases to $T \approx 10^8$ K, and the rotating NS can appear as a pulsar, if the rotational axis has a suitable inclination. The pulse periods are in the range of $0.7\,\mathrm{s}$ to a few $100\,\mathrm{s}$ and are related to the rotational period of the NS. Due to angular momentum transfer, the neutron star can suffer a spin-up or a spin-down. The orbital periods of such systems are typically a few days. Inhomogeneities in the mass flow, such as blobs, can produce additional variations in the X-ray light curve. Instead of a NS, a BH can also be the compact object. More than 30 years ago, X-ray observations revealed the first HMXRBs. So the massive binaries were one of the first classes of X-ray objects detected and identified (Motch et al. 1997). Two examples for this object class are Her X-1, a binary accreting via Roche-lobe overflow, and the wind accreting system Vela X-1.

2.3.3 Low mass X-ray binaries – LMXRBs

In contrast to HMXRBs, the donor star in LMXRBs are mostly main-sequence stars (often of spectral type G or M) with a low mass of $M_\star \lesssim 1.4\,\mathrm{M}_\odot$. Due to the low mass, the donor star evolves slowly, and the systems are usually old

systems with typical lifetimes of $10^7 - 10^9$ years (Rosswog & Brüggen 2007). So the systems undergo a long LMXRB phase during their lifetime. The accretion in these systems is driven by Roche-lobe overflow from matter of the donor star towards the compact object. When transferring mass and angular momentum to the object, an accretion disc can be formed (Section 2.3.1). LMXRBs are strong sources in the soft X-ray band ($L_\mathrm{X} > 10^{34}\,\mathrm{erg/s}$). The spectrum of the accretion disc dominates the X-ray spectrum and also the spectral energy distribution (SED) of the entire binary ($L_\mathrm{X}/L_\mathrm{opt} = 10^2 - 10^4$). The observation of the companion star is often difficult and is usually only possible if the system has a large orbital separation. LMXRBs have orbital periods that range from minutes up to several days. In general, LMXRBs are rather old objects and their NSs have weaker magnetic fields than in HMXRBs (about $B = 10^8 - 10^{12}\,\mathrm{G}$).

Usually, the emission of LMXRBs is not pulsed (Unsöld & Baschek 1999). A subclass of LMXRBs, however, are the so-called millisecond pulsars. These systems harbour NSs as compact objects with short rotation periods, which seem to have larger masses than standard NSs, i. e. $1.35\,\mathrm{M}_\odot$, but less strong magnetic fields of $\approx 10^9\,\mathrm{G}$ that have decayed during the long LMXRB phase from the typical magnetic fields ($B \approx 10^{12}\,\mathrm{G}$) with which NSs are born. The long accretion phase with the transfer of a substantial amount of mass and angular momentum can be also responsible for the spinning up of the NS to periods of milliseconds.

Phenomena that occur in LMXRBs are X-ray bursts. They are generated when material, which is mostly hydrogen, is accreted to the weakly magnetised surface and is burnt into helium. The conditions on the NS surface are such that the helium is degenerate and a thermonuclear explosion on the NS surface takes place. After the helium is ignited, a runaway burning process starts, and a rapid increase of the X-ray luminosity with a typical duration of about $1\,\mathrm{s}$ takes place. Then the material cools again, and the luminosity drops back to its original state within tens of seconds. Besides these short X-ray bursts, outbursts with longer (which means hours) duration can appear. Explosive carbon burning in deeper layers of the accreted material is thought to be the origin for these so-called super-bursts.

Many LMXRBs are transients, i. e. they suffer long periods of very low accretion rates and therefore low luminosities ($L_\mathrm{lowstate} \approx 10^{30} - 10^{32}\,\mathrm{erg/s}$). These phases are interrupted by periods with large accretion rates and high luminosities ($L_\mathrm{highstate} \approx 10^{38}\,\mathrm{erg/s}$), most likely through disc instabilities and subsequent changes in viscosity and accretion rates.

2.3.4 Radio-emitting X-ray binaries – REXRBs

About 10% of the known Galactic XRBs show radio emission (Mirabel & Rodríguez 1999, and references therein). These so-called Radio emitting X-ray binaries (REXRBs) or radio loud XRBs are among the most efficient radio sources in the Galaxy. Their radio emission is usually of non-thermal synchrotron origin and is sometimes dramatically related to violent and exotic phenomena, such as the relativistic ejection of plasma clouds in a scaled down microquasar scenario (see e. g. Mirabel & Rodriguez 1998 for a review). Today not more than 30 REXRBs are identified, and the precise mechanisms and the reason why some systems are radio loud are still not completely understood. Amongst the radio loud HMXRBs are e. g. SS 433, Cyg X-1, Cyg X-3, CI Cam, LS I $+61°303$ and, LS 5039 (Charles & Seward 1995).

Besides these XRBs, important for this thesis, there are other types of binaries which emit in the X-ray energy range, such as e. g. cataclysmic variables (CVs). CVs consist of a main-sequence star and a matter accreting white dwarf. The X-ray emitting binaries can appear in several kinds like transients or eclipsing binaries.

2.4 Evolution of binary systems

Binaries appear in several evolutionary stages, since in principle the binary components evolve like single stars (Section 2.1). In addition to the single star evolution, in a binary the components influence each other when they evolve. In the following section, an overview of the binary system evolution is given. The description is divided into two possible evolutionary sequences depending on whether the system will last a long time as HMXRB or as LMXRB.

Most of the binaries or multiple star systems are already formed during the birth of the stars in an interstellar cloud. As a consequence of the growing gravitational forces of the more and more massive proto-stars and the conservation of angular momentum, two originated main-sequence stars orbit each other and build a binary. The more massive star is called primary and evolves faster and explodes in a supernova or ejects its outer shells during the life as a red giant. A compact object remains. The type of the compact object can be every type at the end of stellar evolution: a white dwarf, a neutron star or a stellar black hole. If the binary has rather massive components, like a primary with a mass

of 14.4 $\mathrm{M}_\odot$ and an 8.0 $\mathrm{M}_\odot$ star as secondary, it will evolve via a stage in which it appears as a HMXRB towards a double neutron-star system, one NS of which is a radio pulsar. If the stars are less massive in the beginning, e. g. 15.0 $\mathrm{M}_\odot$ and 1.6 $\mathrm{M}_\odot$, only the more massive star has enough mass to become a NS. The binary evolves via the stage of a LMXRB towards a NS-WD binary, the NS in which is a millisecond radio pulsar.

In the following description, the several stages of a HMXRB are displayed in detail, whereas the characteristics of the LMXRB evolution are mentioned afterwards for completeness. Figure 2.4 illustrates the evolutional scenario. The numbers for star masses and timescales given are examples. They are typical and calculated consistently (Bradt 2008).

In this example, the binary main-sequence stars orbiting each other in a circular orbit have an orbital period of the order of several hundred days in the beginning. This stage lasts rather long (about several million years) and ends, when the more massive component evolves into a red giant. Then it begins to fill its Roche lobe and an overflow of a large amount of matter toward the less massive star begins. A Roche-lobe overflow takes place. The main part of mass ejected by the red giant is caught by the former lower mass star, until the mass ratio between the two components is inverted. The former about 14 $\mathrm{M}_\odot$ star ends up as a 3.5 $\mathrm{M}_\odot$ star, the 8.0 $\mathrm{M}_\odot$ star increases its mass to 16.5 $\mathrm{M}_\odot$. The transferred matter is mostly the product of hydrogen burning, helium, so the secondary becomes a helium star. The remnant of the primary undergoes a core collapse, a supernova (SN) explosion takes place. Two consequences follow from this SN explosion. Firstly, the surviving system has a large eccentricity and a wide orbit. The eccentricity reached is directly related to the amount of mass lost in the SN event. Secondly, the entire system suffers a kick (McSwain & Gies 2002). The runaway velocity also depends on the mass loss in the SN and can be measured. Not before some tens of million years pass in this quiet stage, does the secondary begin to evolve into a red giant. While the star expands and loses 10% of its mass due to strong stellar winds, an additional rearrangement takes place. The eccentricity of the orbit decreases due to tidal forces, until the orbit is close to a circular orbit. Close to filling its Roche lobe, the secondary ejects a large amount of mass due to its strong stellar wind. This ejected matter is captured in the gravitational potential of the NS and afterwards accreted onto it. The accretion leads to strong X-ray emission, a HMXRB can be observed. In general, the Roche lobe is not filled and therefore no Roche-lobe overflow occurs in these systems. But the evolution

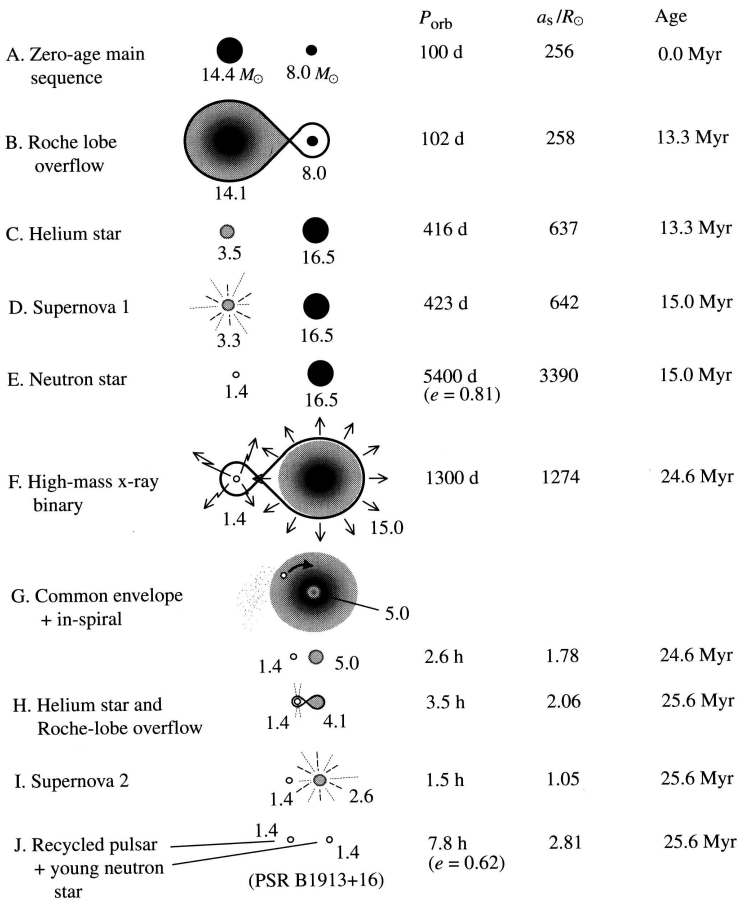

Figure 2.4: This sketch shows the evolution of a binary system, which includes the evolutionary stage of a Be-star/HMXRB. A detailed description can found in the text. Figure from Bradt (2008), which was adapted from Tauris & van den Heuvel (2003).

of the secondary continues, it further expands and reaches its Roche volume. The resulting Roche-lobe overflow is not stable. Due to the large mass ratio of the two binary components, the separation is reduced very fast, and the neutron

star is soon embedded in the envelope or in other words the atmosphere of the secondary. During this very short lasting[11] common envelope phase, the NS undergoes a so-called rapid spiral-in, and, in addition, a large amount of mass is ejected. At the end, only the helium core, which is a star with mass of about $5\,\mathrm{M}_\odot$, and the NS survive in a detached binary system. The orbital period has changed from values of $P_{\mathrm{orb}} \approx 1000\,\mathrm{d}$ in the HMXRB stage to values of about only a few hours. When, after about 1 Myr, the helium star will evolve, mass transfer towards the primary NS will take place via a stellar wind or a Roche-lobe overflow. This mass loss from the secondary could go along with X-ray emission. When reaching a mass of about $2.6\,\mathrm{M}_\odot$, the helium star will explode in a supernova. The resulting binary is again a double-neutron star, one component of which is a pulsar and the other a young neutron star. Therefore radio pulses can be observed. PSR B1913+16 is an example of such a system.

The evolutionary sequence comprising the stage of a LMXRB starts e. g. with a primary of mass $15.0\,\mathrm{M}_\odot$ and a secondary of mass $1.6\,\mathrm{M}_\odot$. The orbit is circular and the orbital period can be thousand days or more. As in the scenario described above, the primary evolves to a red giant after a few tens of million years, fills its Roche lobe, and matter is transferred towards and accreted by the secondary. This stage is unstable, whereupon the system separation decreases, the stars enter a common envelope and a rapid spiral-in phase. The outer layers of the giant are ejected and leave a close binary system behind containing a helium and a normal star orbiting each other with orbital periods of fractions of one day. Under the assumption that the secondary has survived these incidents essentially intact, which is likely the case, the catastrophic event in the evolutionary sequence is the following: The helium star explodes in a supernova. The surviving binary system contains a $1.3\,\mathrm{M}_\odot$ neutron star orbiting the $1.6\,\mathrm{M}_\odot$ normal star in a slightly eccentric ($e = 0.24$) and wider orbit than it was before ($P_{\mathrm{orb}} = 2.08\,\mathrm{d}$). Afterwards nothing happens for a long time period of about $t = 2.24\,\mathrm{Gyr}$. Then the normal star evolves and expands to a red giant, fills its Roche lobe, and mass is transferred to the NS via a Roche-lobe overflow. A LMXRB is born. The LMXRB state again lasts a long time, about $400\,\mathrm{Myr}$, and the source emits in the X-ray energy range. These are the reasons why the number of detected LMXRBs in the X-ray domain is comparatively high. While the mass of the primary is less than the secondary mass, the separation between the stars decreases. As soon as the masses are equalised, the mass transfer effects an increasing distance. Nevertheless, the overflow

[11] The time period is only about ten thousand years.

continues due to the expansion of the donor star. The final act in the binary evolution scenario starts when the material in the red giant envelope is running short. The accretion spins up the NS to spin periods as rapid as 2 ms. A detached system containing a NS, which is a millisecond pulsar, and a WD is left over. The pulsar is seen in the radio as soon as its surroundings clear up.

2.5 TeV binaries

VHE γ-ray emission from X-ray binaries or cataclysmic variables was not expected primarily because observations in other wavelength ranges give no evidence of emission in the PeV $-$TeV energy range. Therefore, non-thermal processes were not required for modelling the observations (Weekes 1992). The detection of X-ray binaries as VHE γ-ray sources, hence, was serendipitous and controversially discussed. Since the detection of microquasars (Mirabel & Rodríguez 1994), including the observation of relativistic jets in Galactic sources, it is generally accepted that non-thermal processes play an important role in accretion-driven sources. Binaries became more interesting as possible sources of VHE γ-rays. The mechanisms that are important for the VHE γ-ray production are listed in Section 2.2.2 and explained in Chapter 3.

The currently known TeV binaries are Cyg X-1, LS I $+61°303$, PSR B1259–63 and LS 5039. In the following paragraphs, the three first mentioned sources confirmed by the new generation of Imaging Atmospheric Čherenkov Telescopes (*H.E.S.S.*, MAGIC, VERITAS) as TeV binaries are presented, and the basic parameters for all four systems are collected in Table 2.1 at the end of this chapter. Detailed information about LS 5039 is given in Section 5 and Chapter 6. In addition, the prototype of the microquasar class, SS 433, is listed, because TeV emission has been expected from this source.

Cyg X-1

Cyg X-1 is a persistent source consisting of a BH and an O star. The O star has a strong stellar wind and nearly fills its Roche lobe. Hence, the wind is focused and strongly asymmetric. As a black hole system, Cyg X-1 undergoes several states: the low/hard and high/soft state supplemented by the intermediate and quiescent state, at which the spectrum, timing and luminosity of the system

change dramatically.[12] Theoretically, this is explained by a change of the mass accretion rate and a change of the accretion geometry in the system. A recent review and new studies on this source can be found in Fritz (2008).

Albert et al. (2007) reported evidence for VHE γ-ray emission observed with MAGIC for this source. This is the first observation of VHE γ-rays generated in a Galactic stellar mass BH and, in addition, for an accreting binary system. These authors can give only an upper limit for a steady VHE γ-ray flux of 1%-5% of the flux of the Crab Nebula in the energy range from $150\,\mathrm{GeV}$ up to $3\,\mathrm{TeV}$. However, they detected VHE γ-ray emission in a short time interval (about $79\,\mathrm{min}$ on 24 September 2006) near the inferior conjunction phase interval of the optical star, which is correlated with the hard X-ray emission simultaneously observed by *Swift* and *INTEGRAL*. Therefore, they suggested that the hard X-rays and VHE γ-rays are produced in regions related to the jet.

LS I $+61°303$

The source LS I $+61°303$ is a binary containing a rapidly rotating early type B0 Ve star and a NS, which is a moderately young pulsar ($10^4 - 10^5\,\mathrm{yr}$) orbiting each other with an orbital period of $P_{\mathrm{orb}} = 26.5\,\mathrm{day}$. Multiwavelength observations reveal the source to be an unusually variable, non-thermal radio source associated with the optical star LS I $+61°303$ and also a counterpart of a γ-ray source (Albert et al. 2006). The morphology of the radio emission changes with the orbital phase (Dhawan et al. 2006). This supports the interpretation of this source as a non-accreting young pulsar, having been classified as microquasar formerly. Following the suggestion of Rees & Gunn (1974) for explaining the observations of the crab nebula pulsar and the physical properties in the surrounding area, it is also assumed for LS I $+61°303$ that the pulsar loses its rotational energy via a relativistic wind.[13]

In the colliding region between the relativistic wind and the wind of the primary star, a shock front is formed. Here, particle acceleration takes place, and the pulsar power is converted into radiation in various frequency bands, e. g. optical photons of the primary are Compton-scattered by relativistic electrons generated by the pulsar. Compared to isolated pulsars like the Crab pulsar or the Vela pulsar, the particle energies generated in the shocks are much higher.

---

[12] Low and high states are named according to the luminosity, while hard and soft state are defined by the index of the power law, the spectrum can fit with. It appears that low luminosity comes along with a hard spectrum and high luminosity with a soft spectrum.

[13] A relativistic wind consists of electromagnetic waves and relativistic particles.

Recently, Jogler et al. (2009) published MAGIC and VERITAS observations that exhibit regular periodic VHE γ-ray outbursts from this source. These outbursts did not appear at periastron passage, but remarkably coincide with X-ray outbursts and also feature a similar shape. This correlation forces the idea that TeV γ-ray as well as X-ray emission is initiated by one and the same physical mechanism or at least by one accelerated particle population and its secondaries.

PSR B1259–63

The system PSR B1259−63 / SS 2883 is a binary consisting of a radio pulsar orbiting a Be-type star in a highly eccentric $e = 0.87$ orbit. The pulsar has a rotational period of $P_{\rm spin} = 47\,{\rm ms}$, a strong surface magnetic field $B_{\rm NS} \approx 3.3 \times 10^{11}\,{\rm G}$ and consequently a strong relativistic wind which makes accretion of the wind of the massive star impossible. But the relativistic wind of the pulsar interacts with the wind of the massive star. In the interaction region, a shock forms, particles can be accelerated up to TeV energies, and VHE γ-rays are produced. This becomes most effective around the periastron passage when the compact object is enclosed by the disc-like, structured, dense bulge around the Be star. The dependence of the VHE γ-ray emission on the orbital phase was observed by Aharonian et al. (2005c). Different models for the VHE γ-ray generation are discussed. On the one hand, it is expected that this high energy emission is generated by electron-positron pair production and annihilation (Grove et al. 1995; Tavani & Arons 1997). On the other hand, it can also be inverse Compton scattering of soft radiation from the massive star (Kirk et al. 1999). Also, a hadronic model was inserted into discussion (Kawachi et al. 2004; Neronov & Chernyakova 2007).

SS 433

SS 433 is the prototype of the so-called microquasar class and a very exotic source. Because the source shows properties as they occur in Galactic binaries as well as properties observable from radio galaxies and quasars, its nature has been puzzling for a long time. For this reason, Charles & Seward (1995) dedicated a whole chapter in their textbook to this single source. Nowadays, it is generally believed that SS 433 is the remnant of the exploded progenitor star of the supernova producing the SNR W50 and is located at a distance of $5.5\,{\rm kpc}$ within our Galaxy. The system contains a 14 magnitude bright optical star of

the spectral type B and a compact object which is a BH with a mass of $M_{\rm co} = 30{-}60\,{\rm M}_\odot$ orbiting each other with an orbital period of about $13\,{\rm days}$. Directly observable radio emission reveals a pair of oppositely directed jets. These jets are perpendicular to the accretion disc and moving with a relativistic speed of about $v = 0.26\,c$ which corresponds to about $78\,000\,{\rm km\,s^{-1}}$. The disc, and as a result also the jets, precess with a period of $164\,{\rm days}$ around the common axis. Hence, the jets show a corkscrew motion. The relativistically moving material must produce a strong shock when colliding with the slower moving gas in the surrounding shell. In this shock the matter heats up to temperatures at which X-rays are emitted. The jet velocity of exact $v = 0.26\,c$ can lead to an acceleration of the jet material due to radiation pressure. The jets have a mass-loss rate of $\dot{M} > 5 \times 10^{-7}\,{\rm M}_\odot\,{\rm yr}^{-1}$ and a kinetic luminosity of $L_{\rm kin} > 10^{39}\,{\rm erg\,s^{-1}}$. Thus, a very high mass transfer rate is expected, if the source is a direct descendant of a HMXRB in which the more massive companion star now fills its Roche lobe and is transferring mass on a thermal time-scale. Although SS 433 is a hot candidate for VHE γ-ray emission, only an upper limit could be determined, as yet (Saito et al. 2009).

Further TeV binary candidates

Some more binaries, especially microquasars, are thought to be possible sources of VHE γ-rays, but have not been explicitly detected yet. Saito et al. (2009) determined upper limits for GRS 1915+105 and Cyg X-3. These authors also observed SS 433 and Cyg X-1. Recently, HESS J0632+057 has been supposed to be a new TeV binary (Hinton et al. 2009; Acciari et al. 2009). Although the detection is not confirmed yet, this source shows remarkable similarities to LS I $+61^\circ303$.

References for Table 2.1 displayed on the next page.

[a] McSwain et al. (2004)
[b] Moldon et al. (2009)
[c] Aragona et al. (2009)
[d] Casares et al. (2005b)
[e] Dhawan et al. (2006)
[f] Zdziarski et al. (2008)
[g] Esposito et al. (2007)
[h] Casares et al. (2005a)
[i] Uchiyama et al. (2009)
[j] Sierpowska-Bartosik & Bednarek (2008)
[k] Fritz (2008)

Table 2.1: The currently confirmed TeV binary systems. * The two values are results from the determination of an orbital solution and are in principle both possible. ** The lower value is the wind velocity at apastron, the higher value at periastron passage.

	LS 5039	LS I +61°303	PSR B1259−63	Cyg X-1
nature of compact object	NS/BH ?	NS/pulsar [e]	NS/pulsar [f]	BH [k]
system type	HMXRB/MQ?	Be/XRB / pulsar [e]	Be/XRB / pulsar [i]	HMXRB/MQ [k]
spectral type	ON6.5((f)) [a]	B0 Ve [c]	B2e [i]	O9.7Iab [k]
$L_\star$ [erg s^{-1}]	7×10^{38} [b]	1.3×10^{38} [f]	3.3×10^{37} [j]	10^{39} [k]
$L_{\rm co}$ [erg s^{-1}]		$\sim 10^{33}$ [g]	8.3×10^{35} [j]	4×10^{37} [k]
$f(m)$ [M$_\odot$]	0.00261 ± 0.00036 [c]	0.0124 ± 0.0022 [c]		0.252 ± 0.010 [k]
$M_\star$ [M$_\odot$]	$22.9^{+3.4}_{-2.9}$ [d]	12.5 ± 2.5 [f]	10 [j]	17.8 [k]
$M_{\rm co}$ [M$_\odot$]	$1.49 - 1.81 < M < 8 - 10$ [d]	1.4 (NS) [4 (BH)]*		8.7 ± 0.1 [k]
$R_\star$ [cm]	7×10^{11} [d]	4.7×10^{11} [f]	4.2×10^{11} [j]	11.8×10^{11} [k]
$R_{\rm co}$ [km]				30 [k]
$\dot{m}_w$ [M$_\odot$ yr^{-1}]	7×10^{-7} [b]		$\sim 2 \times 10^{-7}$ [j]	3×10^{-6} [k]
v_w [km s^{-1}]		$1\,000 - 7\,500$ ** [e]	~ 2000 [j]	2100 [k]
$P_{\rm spin}$ [ms]			47.7 [j]	
$P_{\rm orb}$ [d]	3.90608 ± 0.00010 [c]	26.4982 ± 0.0076 [c]	1236.72 [j]	5.59974 ± 0.00008 [k]
e	0.337 ± 0.036 [c]	0.537 ± 0.034 [c]	0.87 [j]	
$\phi_{\rm periastron}$	0.0	0.275 [c]		
ω [°]	236.0 ± 5.8 [c]	40.5 ± 5.7 [c]		
$a_1 \sin i$ [R$_\odot$]	1.435 ± 0.066 [c]	8.64 ± 0.52 [c]		
$a \sin i$ [km]				$5.82 \pm 0.08 \times 10^6$ [k]
i	$13° < i < 64°$ [d]	$10° < i < 60°$ [h]	$\sim 36°$ [j]	$31° < i < 44°$ [k]
d [kpc]	2.5 ± 0.1 [d]	2.0 ± 0.2 [g]	$1.5 - 4.5$ [j]	2.5 ± 0.3 [k]

CHAPTER 3

Astrophysical processes

3.1 Acceleration processes

All VHE γ-ray production mechanisms are based on particles or cosmic rays that have been accelerated to very high energies. The highest energetic cosmic rays are accelerated to energies up to 10^{20} eV, and already for this reason an extreme accelerator is necessary. Different acceleration processes can cause such high accelerations, but the efficiency of the diverse acceleration mechanisms differs. In general, cosmic acceleration mechanisms are based on magnetohydrodynamics in hot plasmas.

In astrophysical sources, particles are mainly accelerated in shock fronts or in moving magnetic plasmas (Klapdor-Kleingrothaus & Zuber 1997). The main mechanism that occurs in such surroundings is the Fermi acceleration mechanism.

3.1.1 Acceleration in shock fronts and clouds – Fermi mechanism first order

Fermi acceleration (Fermi 1949) is the acceleration of relativistic particles in strong shock waves (first order) or in statistically distributed magnetic plasma clouds (second order). The nomenclature comes from the dependence of energy gain on particle velocity, $\beta = v/c$. Since the acceleration in shock fronts is very effective and fast, it is the dominant acceleration process in many astrophysical sources of high energetic particles, like e. g. jets and is, therefore, described in detail in the following section. The description is based mainly on Rieger et al. (2007) and Longair (1994).

The principle of Fermi acceleration is based on the elastic scattering of relativistic charged particles in a non-stationary magnetic field, from which the

particles gain energy in every single scattering process. However, particles only gain energy if the collision happens head-on or in overtaking.

An environment for effective particle acceleration is e. g. a strong nonrelativistic shock wave that propagates through a plasma with a velocity V. In the co-moving frame of the shock front, the regions ahead and behind the shock front appear to have different velocities. The region ahead of the shock front is called the upstream region and its velocity u_{up} is much higher than the velocity behind the shock, in the downstream region u_{down}. In the frame of the upstream or the downstream region, the respective other region approaches with $u = u_{\mathrm{up}} - u_{\mathrm{down}}$. Therefore, a particle crossing the shock front will always suffer a head-on collision and will gain the average energy

$$\left\langle \frac{\Delta E}{E} \right\rangle = \frac{2}{3}\frac{V}{c} \quad . \tag{3.1}$$

The particle will migrate in the reached region due to random scattering processes without losing energy and will recross the shock again, so after one crossing cycle the total energy the particle has gained is

$$\left\langle \frac{\Delta E}{E} \right\rangle = \frac{4}{3}\frac{V}{c} \quad . \tag{3.2}$$

The acceleration time t_{acc} depends on the times, the particle remains in the upstream and the downstream region. The spectrum that results for particles accelerated via the first order Fermi mechanism is a power law $N(E) \propto E^{-x}$. The spectrum depends only on the shock compression $\rho = u_{\mathrm{up}}/u_{\mathrm{down}}$, which is in the range of $1 < \rho \leq 4$

$$x = \frac{\rho + 2}{\rho - 1} \quad . \tag{3.3}$$

For strong shocks the shock compression is $\rho = 4$ in the test particle limit and, therefore, $x = 2$.

To estimated the power-law shape of the spectrum we can consider the escape probability of the particle from the acceleration region. For a mean particle energy after one collision, $E = \epsilon E_0$ and a particle escape probability P from the acceleration region the spectrum is

$$\frac{\mathrm{d}N(E)}{\mathrm{d}E} \propto E^{-1+\left(\frac{\ln P}{\ln \epsilon}\right)} = E^{-k} \quad , \tag{3.4}$$

where $k = 1 - (\ln P / \ln \epsilon)$ is the power-law index (Rosswog & Brüggen 2007).

A particle remains in the acceleration region with a probability of $P = 1 - u_{\rm up}/c$. Because $u_{\rm up} \ll c$, and taking into account the continuity equation[1] as well as the assumption of a completely ionised gas, which means that $u_{\rm down} = \frac{1}{4}V$, it follows that the energy increases linear with the shock velocity, $\epsilon = (\Delta E)/(E) = (u_{\rm up})/(c)$. Consequently, because

$$\frac{\ln P}{\ln \epsilon} = \frac{-\frac{u_{\rm up}}{c}}{\frac{u_{\rm up}}{c}} = -1 \Longrightarrow \frac{{\rm d}N(E)}{{\rm d}E} \propto E^{-2} \quad , \tag{3.5}$$

the spectrum has a power-law index of 2. Since the observed power-law index of cosmic rays is about $\Gamma \sim 2.7$, and although this acceleration mechanism is a simple explanation, it is a justification for the interpretation that Fermi acceleration is taking place, that different astrophysical environments show energy spectra with the same power-law index of roughly $\Gamma \sim 2$.

Two problems appear in this basic explanation. First, an effective acceleration due to first-order Fermi acceleration is only possible if the particles have already been preaccelerated. This could be solved by a kind of "electromagnetic wave surfing" of the particles. Second, the highest energies reached by this mechanism are about $E = 100\,{\rm TeV}$ (Grupen 2000). This mechanism is still not sufficient for the production of the most energetic cosmic rays. However, this could be solved by a combination of Fermi first-order acceleration mechanism with different alternative acceleration mechanisms, like e. g. gradual shear acceleration (Rieger et al. 2007).

Discussion

The details of Fermi-type shock acceleration in relativistic shocks have recently become a matter of controversy. While initial calculations by Kirk & Schneider (1987), Achterberg et al. (2001), and Ostrowski (1991) indicated an efficient acceleration of particles following a universal power-law type distribution, recent calculations have revealed substantial difficulties in accelerating particles to form a power-law type particle distribution (Niemiec & Ostrowski 2006; Lemoine et al. 2006). Moreover, detailed studies of particles-in-cell distributions of shocks forming in flows with different magnetisation have not been found to show any non-thermal acceleration at all (Spitkovsky 2005).

[1] The continuity equation is $\rho_{\rm up} u_{\rm up} = \rho_{\rm down} u_{\rm down}$.

While the issue is currently not settled, it appears worthwhile to consider alternative mechanisms to explain the acceleration of particles in ultrarelativistic shocks. An interesting alternative has been proposed by Hoshino et al. (1992) and Arons & Tavani (1994). They suggested a process in which gyrating and reflecting ions dissipate energy in magnetosonic waves in the downstream region. These ions are absorbed by the pair-plasma to form a power-law type spectrum. An important prediction of this model is that the maximum energy achievable in this type of acceleration is given by $\gamma m_i c^2/Z$, where m_i indicates the mass and Z the charge of the ions.

Possible acceleration sites are e. g. pulsars, binary systems, supernovae and their remnants, active galactic nuclei (AGN), the surroundings of black holes, Gamma ray bursts (GRBs), and, in general, all sites where shock waves appear and/or extreme electric or magnetic fields occur, e. g. accretion discs (Grupen 2000).

3.2 Radiation processes

When one wants to interpret an astronomical observation, it is essential to identify the relevant radiation mechanism or mechanisms unambiguously. Therefore, it is necessary to know the typical features of the radiation processes. In each wavelength range – except for the γ-rays – one or two basic radiation mechanisms are dominant and, therefore, characterise the corresponding energy band. In the γ-ray energy range, numerous processes compete with each other and contribute to the observed γ-ray flux in the same energy interval to a similar degree. Then, the observation can be equally well explained with one or with several radiation mechanisms, and it is not possible, or at least very complicated, to distinguish between them.

In the following section, an overview of the most important mechanisms is given, especially those which are necessary to explain the phenomena which occur in sources emitting in the X-ray, γ-ray, and/or VHE γ-ray ranges. Detailed reviews are given by Aharonian (2004); Rybicki & Lightman (1979); Grupen (2000); Charles & Seward (1995); Longair (1992); Shu (1991); Blumenthal & Gould (1970); Ginzburg & Syrovatskii (1965); Reynolds (1982), which are also references for the following summary. The formulae are from Aharonian (2004), Rybicki & Lightman (1979) or Longair (1992), if not mentioned otherwise.

3.2.1 Blackbody radiation

A plasma which is in thermal equilibrium with itself emits so-called blackbody radiation. This radiation process is the most important in the universe, because it describes the shape of stellar spectra. The total spectrum is given by the Planck spectrum

$$B_\nu = \frac{2h\nu^3}{c^2} \frac{1}{e^{(h\nu/kT)} - 1} \quad , \tag{3.6}$$

where ν is the frequency, T the temperature of the emitting plasma, h the Planck constant, k the Boltzmann constant, and c the speed of light. The maximum frequency is directly proportional to the blackbody temperature. So, sources with temperatures of a few $10^6 - 10^8\,\mathrm{K}$ emit thermal blackbody radiation in the X-ray energy range. Thermal blackbody radiation emitted by the hottest objects in the universe, like e. g. accretion discs around black holes, is in the range of $10\,\mathrm{keV}$ ($10^8\,\mathrm{K}$).

For hard X-rays, γ-rays, and VHE γ-rays, thermal blackbody radiation is negligible, because the corresponding temperatures are extremely high. Other radiation processes dominate in this energy regime and generate these very high energetic photons. This is mainly emission from scattering processes of very high energetic particles and emission induced by bending the trajectory of the very high energetic particles in magnetic or electric fields. The spectrum of the very high energetic particles or cosmic rays is specified by a power-law distribution. Hence, also the non-thermal emission has a spectral shape following a power law.

3.2.2 Synchrotron radiation

Synchrotron radiation, also called magnetobremsstrahlung, is the electromagnetic radiation which is emitted when a relativistic charge is deflected in a magnetic field.[2] The force acting onto the charged particle due to the magnetic field causes a helical motion of the particle around the magnetic field lines, which can be treated as an accelerated movement of the charged particle. Consequently, electromagnetic radiation is emitted.

From electrodynamics and for the case of a single, circular moving, accelerated electron with mass m_e and charge e follows the emitted radiation:

$$P_\mathrm{synch} = \frac{2}{3} r_0^2 c \beta_\perp^2 \gamma^2 B^2 \quad , \tag{3.7}$$

[2] For non-relativistic particles, this process is called cyclotron radiation.

where γ is the Lorentz factor, r_0 is the Lorentz radius, B is the energy density of the magnetic field, $\beta_\perp = \frac{v_\perp}{c}$ is the electron velocity perpendicular to the $\vec{B}$-field, and $\sigma_\mathrm{T} = (8\pi r_0^2)/3 = (8\pi e^4)/(3m_\mathrm{e}^2 c^4)$ the Thomson cross section.[3]

The acceleration happens perpendicular to the $\vec{B}$-field, and for a circular motion it is

$$\frac{v_\perp}{R} = \frac{eB}{\gamma m_\mathrm{e} c} = \frac{\omega_\mathrm{L}}{\gamma} = \omega_\mathrm{B} \quad , \tag{3.8}$$

where R is the radius of the orbit, also called Lamor radius, and $\omega_\mathrm{L} = 2\pi\nu_\mathrm{L}$ is the Lamor frequency. Numerical values for the Lamor frequency and the Lamor radius are

$$\nu_\mathrm{L} = 2.8\,\mathrm{MHz}\cdot\frac{B}{1\,\mathrm{G}} \tag{3.9}$$

and

$$R = \frac{\gamma\nu_\perp}{\omega_\mathrm{L}} \approx 2\,\mathrm{AU}\cdot\frac{E}{1\,\mathrm{GeV}}\cdot\left(\frac{B}{10^{-6}\,\mathrm{G}}\right)^{-1} \quad . \tag{3.10}$$

Integrating over all electrons and assuming an isotropic velocity distribution results in an emission power of

$$P_\mathrm{synch} = \frac{4}{3}\sigma_\mathrm{T} c\beta^2\gamma^2\frac{B^2}{8\pi} \sim 1.6\times10^{-2}\,\mathrm{eV\,s^{-1}}\cdot\left(\frac{B^2}{8\pi}\right)\left(\frac{E}{m_\mathrm{e}c^2}\right)^2 \quad , \tag{3.11}$$

since $E = \gamma m_\mathrm{e} c^2$. Important is the dependence $P \propto E^2 B^2$. Synchrotron radiation from charged particles with larger mass, like protons or nuclei, is in general inefficient and, therefore, negligible, since the emitted power $P_\mathrm{synch} \propto \sigma_\mathrm{T} \propto m_\mathrm{e}^{-2}$. Therefore, electrons are the predominant generators for synchrotron radiation in cosmic magnetic fields.[4] The emitted spectrum is continuous. Nevertheless, in regions where ultra-relativistic particles appear, the synchrotron cooling time[5] (Section 3.3) of protons can be comparable to the cooling time of other radiation processes. This timescale can be easily calculated when re-scaling the Lamor frequency by the factor $m_\mathrm{p}/m_\mathrm{e} = 1836$.

Two additional features for the single electron spectrum should be mentioned. First of all, the emitted radiation has a dipole characteristic and is

[3]The value for the Thomson cross section σ_T for non-relativistic energies is $\sigma_\mathrm{T} = (8\pi r_0^2)/3 = 6.652\times10^{-25}\,\mathrm{cm}^2$, where $r_0 = e^2/(m_\mathrm{e}c^2) = 2.82\times10^{-13}\,\mathrm{cm}$ is the classical electron gyro radius. This is also called the Lorentz radius and is equal to the Thomson scattering length.

[4]m_e is the mass of the accelerated particle which, in general, is an electron in a cosmic environment.

[5]Electrons or other particles in a plasma lose energy due to the emission of radiation e. g. synchrotron radiation and, therefore, cool down. An example for typical cooling times is given in Figure 3.5.

beamed forward into a cone due to the relativistic motion. The opening angle of this beaming cone is $\Delta\Theta \sim 1/\gamma$. Taking the circular motion and the Doppler effect into account leads to a pulsed single electron spectrum with a pulse duration of $\tau = (1-\beta)\Delta t$.

If the electron is ultra-relativistic, i. e. $\beta = v/c \sim 1$, the pulse lasts $\tau = 1/(\gamma^2\omega_\mathrm{L})$, where $\omega_\mathrm{L} = (eB)/(m_\mathrm{e}c)$ is the already introduced Lamor frequency. The characteristic frequency of the radiation is then given by Bradt (2008) as:

$$\omega_\mathrm{c} = \gamma^2\omega_\mathrm{L} = \frac{eB}{m_\mathrm{e}c}\left(\frac{E}{m_\mathrm{e}c^2}\right)^2 \quad . \tag{3.12}$$

Electrons with velocities of $\gamma \sim 10^6$ in typical magnetic fields of 10^{-4} G, for instance, emit photons in the optical wavelength range. If the velocity distribution of the electrons is a power law,

$$n(\gamma)\mathrm{d}\gamma = n_0\gamma^{-p}\mathrm{d}\gamma \quad , \tag{3.13}$$

the emitted radiation is called non-thermal synchrotron radiation. Such a distribution can originate from different acceleration processes (see Section 3.1). The resulting spectral energy distribution P_ν of an electron with total energy $E = \gamma m_\mathrm{e}c^2$ is then (based on Equation 3.11)

$$P_\nu(\gamma) = P_\mathrm{synch}\phi_\nu(\gamma) = \frac{4}{3}\sigma_\mathrm{T}c\beta^2\gamma^2\frac{B^2}{8\pi}\phi_\nu(\gamma) \quad , \tag{3.14}$$

where $\phi_\nu(\gamma)$ is the spectral shape function, which describes the frequency distribution of an individual electron. The spectral shape function has a maximum at $\gamma^2\nu_\mathrm{L}$. After integration, the total non-thermal synchrotron power emitted follows also a power law:

$$P_\nu = \frac{2}{3}c\sigma_\mathrm{T}n_0\frac{B^2}{8\pi\nu_\mathrm{L}}\left(\frac{\nu}{\nu_\mathrm{L}}\right)^{-\frac{p-1}{2}} \quad . \tag{3.15}$$

So in the end, the individual electron spectra add up to a superposed power-law spectrum.

The second feature of synchrotron radiation worthy of mention is polarisation. The beaming of the synchrotron radiation emitted by the relativistic electrons leads to a net polarisation of the observed light. The degree of linear

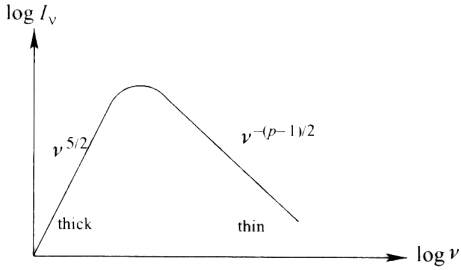

Figure 3.1: Synchrotron radiation spectrum. Figure from Rybicki & Lightman (1979).

polarisation of particles with a power-law distribution of energies (see Equation 3.13) is basically defined by

$$\frac{P_\perp - P_\parallel}{P_\perp + P_\parallel} = \frac{p+1}{p+7/3} \quad , \tag{3.16}$$

where $P_\perp$ and $P_\parallel$ are the emitted power per unit frequency in the direction parallel and perpendicular, respectively, to the projection of the magnetic field on the plane of the sky. p is the power-law index defined in Equation 3.13. If the magnetic field is inhomogeneous, the degree of polarisation can decrease. Moreover, polarisation can occur for other reasons also, for example, when the magnetic field component dominates along the line of sight.

For astrophysical sources, especially for pulsars or supernova remnant analysis, the life-time of particles of the energy E is a key parameter:

$$t_{\rm synch} \sim \frac{E}{P} \propto \frac{1}{B^2 E} = 1.2 \times 10^3 \left(\frac{B}{10\,\mu{\rm G}}\right)^{-2} \left(\frac{E_{\rm e}}{100\,{\rm TeV}}\right)^{-1} {\rm yr} \quad . \tag{3.17}$$

3.2.3 Synchrotron self-absorption

At low frequencies, the synchrotron emitting electrons can absorb synchrotron photons. This process is called synchrotron self-absorption. Then, a power-law electron distribution ${\rm d}N/{\rm d}E \propto E^{-p}$ has a total spectral shape which is divided into two parts. For low frequencies, the emitted radiation is $P_\nu \propto B^{-1/2}\nu^{5/2}$, and for large frequencies $P_\nu \propto \nu^{-(p-1)/2}$. Whether absorption of

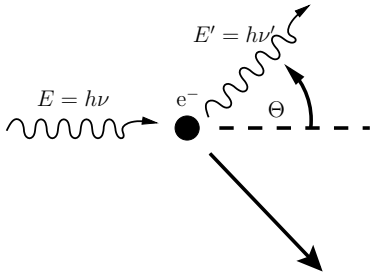

Figure 3.2: Geometry of a Compton scattering process. Before the scattering process the electron is at rest. Figure adapted from Rybicki & Lightman (1979).

the emitted synchrotron emission takes place, depends on the optical depth of the surroundings (Figure 3.1). The threshold is at an optical depth $\tau = 1$. The optical depth τ itself is proportional to the size of the emitting region R, i. e. more compact regions are optically thick, whereas more extended regions are optically thin. The cut-off frequency can be used to determine the strength of the magnetic field. At very high frequencies, an additional break occurs due to electron energy losses (Section 3.3).

3.2.4 Inverse Compton scattering

A typical Compton scattering process is shown in Figure 3.2. A photon is scattered off an electron in rest and loses energy in this process and transfers the energy in the form of kinetic energy to the electron. The final energy of the photon is (Bradt 2008)

$$E' = h\nu = \frac{E}{1 + \frac{E}{mc^2}(1 - \cos\,\Theta)} \quad , \tag{3.18}$$

where Θ is the angle of direction change of the photon and E and E' the energies of initial and scattered photon, respectively.

For scattering processes, it is important to know the differential cross section, which was explored in the scope of quantum electrodynamics by Heitler (1954) for unpolarised radiation (Rybicki & Lightman 1979):

$$\frac{\mathrm{d}\sigma_{\mathrm{IC}}}{\mathrm{d}\Omega} = \frac{3}{16\pi}\sigma_{\mathrm{T}}\left(\frac{E'}{E}\right)^2\left(\frac{E}{E'} + \frac{E'}{E} - \sin^2\Theta\right) \quad . \tag{3.19}$$

If this well-known Klein-Nishina formula is integrated over all scattering angles, the result is the Klein-Nishina cross section, which describes the cross section for a photon scattering off an electron that is in rest (Rybicki & Lightman 1979):

$$\sigma_{\mathrm{IC}} = \frac{3}{4}\sigma_{\mathrm{T}}\left[\frac{1+x}{x^3}\left(\frac{2x(1+x)}{1+2x} - \ln y\right) + \frac{1}{2x}\ln y - \frac{1+3x}{y^2}\right] \quad , \tag{3.20}$$

where $x = E/m_{\mathrm{e}}c^2$ and $y = 1+2x$. For large energies $x \gg 1$, i. e. $E \gg m_{\mathrm{e}}c^2$ and unpolarised radiation, the Klein-Nishina formela can be approximated by:

$$\sigma \approx \frac{3}{8}\sigma_{\mathrm{T}}\frac{1}{x}\left(\ln 2x + \frac{1}{2}\right) \tag{3.21}$$

Inverse Compton scattering is the vice-versa process, i. e. photons are scattered off energetic electrons and, hence, change their direction and gain energy.[6] The mean free path describes the average distance between two scattering events: $\langle l \rangle = 1/(n\sigma)$, where n is the number of scattering particles or photons. In the case of photons, the mean free path is the distance that corresponds to an optical depth of $\tau = 1$.

The energy gain of the photon field depends on the electron distribution. One needs to distinguish between thermal and non-thermal inverse Compton scattering processes. While the thermal inverse Compton processes (also called Comptonisation) is important in many astrophysical sources, in this thesis the non-thermal inverse Compton scattering plays the leading role. For the description of Comptonisation it is referred to Rybicki & Lightman (1979), Longair (1992), and Bradt (2008). For the case of non-relativistic electrons (Thomson regime, $\gamma\hbar\nu << m_{\mathrm{e}}c^2$) the net power gain of the photon field can be calculated (Rybicki & Lightman 1979)

$$P_{\mathrm{compt}} = \frac{4}{3}\sigma_{\mathrm{T}}c\gamma^2\beta^2 U_{\mathrm{rad}} \quad , \tag{3.22}$$

where $U_{\mathrm{rad}} = \int E\, V(E)\, \mathrm{d}E$ is the initial photon energy density, while $V(E)$ is the photon energy density distribution and is related to the phase space density $n(p)$ via

$$V(E)\, \mathrm{d}E = n(p)\, \mathrm{d}^3p \quad . \tag{3.23}$$

[6] The limit of Compton scattering at low energies is the well known Thomson scattering. Here the initial and the final wavelength are identical.

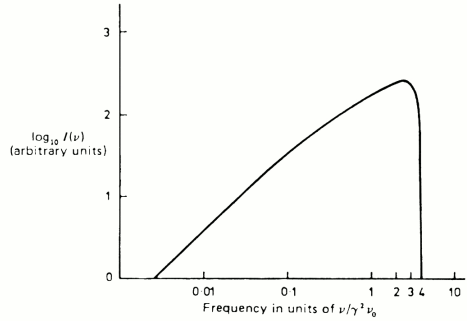

Figure 3.3: The emission spectrum of inverse Compton scattering. The incident isotropic photon field is assumed to be monochromatic with a frequency ν_0. The exact calculation is not trivial and can be found in Blumenthal & Gould (1970). Figure from Longair (1992).

The general case is not trivial to calculate and an exact formula of the emitted Compton spectrum, if the initial electron spectra is a power law, is given by Blumenthal & Gould (1970). Figure 3.3 shows the resulting inverse Compton spectrum.

Inverse Compton scattering depends on the angle between the propagation directions of the electron and the photon, respectively. Therefore, the resulting spectrum of scattering processes of an electron distribution of photons from a point-like source or a source with finite size will have a dependence on the viewing angle. Figure 3.4 shows two calculations for this dependence, for the Thomson and the Klein-Nishina regime, which correspond typically to electron energy ranges of $10^3 < \gamma_\mathrm{e} < 10^5$ and $10^5 < \gamma_\mathrm{e} < 10^7$, respectively.

One fact should be mentioned in addition: the so-called Compton catastrophe.

Power is emitted by synchrotron radiation proportional to the magnetic field of an energy density $U_\mathrm{B} = B^2/(8\pi)$. In magnetised plasmas, synchrotron photons are inverse Compton scattered by the electrons. The ratio of emitted

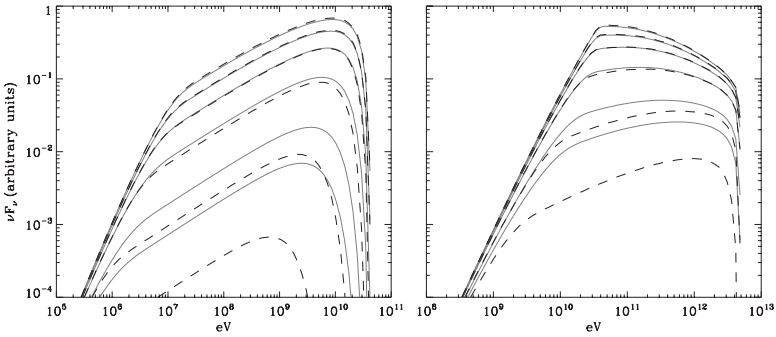

Figure 3.4: Dependence of the inverse Compton spectrum on the viewing angle. The *left* panel is the calculation for the Thomson regime, the *right* one for the Klein-Nishina regime. The photon source is assumed to be a star with a temperature of $kT = 1\,\mathrm{eV}$ and the source of electrons follows a power law $\mathrm{d}n_\mathrm{e} = \gamma^{-2}\,\mathrm{d}\gamma_\mathrm{e}$ and is located at a distance of $d = 2\,\mathrm{R}$, where $R_\star$ is the radius of the star. The viewing angles shown are from bottom to top: $15°$, $30°$, $60°$, $90°$, $120°$, and $180°$. Solid and dashed lines correspond to a finite size and a point source approximation for the star size, respectively. Figure from Dubus et al. (2008).

powers is then (considering Equation 3.14 and Equation 3.22)[7]

$$\frac{P_\mathrm{compt}}{P_\mathrm{synch}} = \frac{U_\mathrm{rad}}{U_\mathrm{B}} \quad . \tag{3.24}$$

For $U_\mathrm{rad} > U_\mathrm{B}$ and, hence, $P_\mathrm{compt} > P_\mathrm{synch}$, the synchrotron photon field will undergo a dramatic amplification, and the result is very efficient cooling of electrons by inverse Compton losses. A further result is that the brightness temperature of radio sources is limited to $10^{12}\,\mathrm{K}$.

3.2.5 Bremsstrahlung

Bremsstrahlung, which is also called free-free radiation, is the radiation that originates when a charge is accelerated in a Coulomb field of another charge. The most important interactions are electron-electron, electron-proton, electron-positron and electron-nucleus bremsstrahlung. Among these interactions, the

[7] This is a direct consequence of the fact that (in QED) the synchrotron radiation is inverse Compton scattering of virtual photons of the magnetic field.

electron-proton interactions dominate, e. g. over proton-proton bremsstrahlung. For particle-nucleus bremsstrahlung, the acceleration of electrons is much more significant than the acceleration of other particles. Nevertheless, bremsstrahlung is among the most effective processes resulting in high and very high energy γ-ray emission. Bremsstrahlung is mainly caused by electrons, and the following description is focused on bremsstrahlung of electrons.

As for each radiation process, one should distinguish also bremsstrahlung into thermal and non-thermal, and into relativistic and non-relativistic bremsstrahlung. Thermal bremsstrahlung is emission from a plasma of thermal particles, the velocities of which follow a Maxwell-Boltzmann distribution. Accordingly, for non-thermal bremsstrahlung, the initial distribution of velocities needs to be known.

Let us first have a look at thermal bremsstrahlung. To create a photon, the incident velocity v of the electron must be at least $h\nu \leq \frac{1}{2}mv^2$, because otherwise a photon of energy $E = h\nu$ could not be created. This lower limit of the integration over electron velocities is called photon discreteness effect.

The total power emitted per unit volume for thermal bremsstrahlung and for an isotropic distribution of electron velocities is

$$\begin{aligned} \epsilon^{ff} = \frac{\mathrm{d}W}{\mathrm{d}t\mathrm{d}V} &= \left(\frac{2\pi kT}{3m_\mathrm{e}}\right)^{1/2} \frac{2^5\pi e^6}{3hm_\mathrm{e}c^3} Z^2 n_\mathrm{e} n_\mathrm{i} \bar{g}_\mathrm{B}(T) \\ &= 1.4 \times 10^{-27} T^{-1/2} Z^2 n_\mathrm{e} n_\mathrm{i} \bar{g}_B(T) \quad , \end{aligned} \tag{3.25}$$

where n_e is the electron density and n_i is the ion density. Furthermore, $\bar{g}_\mathrm{B}(T)$ is the frequency average of the velocity averaged Gaunt factor $\bar{g}_{ff}$. The Gaunt factor is introduced as a quantum mechanics correction factor into the classical derivation values ranging between 1.1 and 1.5. The numerical values are given in cgs units, i. e. $[\mathrm{erg\ s^{-1}\ cm^{-3}}]$.

The inverse process to bremsstrahlung is absorption by a free moving electron. If an astronomical source radiates bremsstrahlung purely, both emission and absorption show up in the spectrum, i. e. the dependence of frequency on the intensity is proportional to ν^2 for lower frequencies[8] corresponding to a rather flat spectrum at high frequencies.

When examining relativistic bremsstrahlung, one needs to consider collisions between an electron and a heavy ion of charge Ze. In general, the ion

[8] cf. Rayleigh Jeans dependence

moves more slowly in comparison with the electron, so the relativistic bremsstrahlung can be regarded as the Compton scattering of a virtual quantum of the ion's electrostatic field seen in the electron's frame.

The spectral shape of the bremsstrahlung γ-ray spectrum simply reflects the initial shape of the electron spectrum $Q(\varepsilon_\mathrm{e}) \propto \varepsilon_\mathrm{e}^{-\Gamma}$, i. e. the bremsstrahlung γ-ray spectrum is a power law with the same power-law index as the initial spectrum of the accelerated electrons.[9]

The lifetime of electrons due to bremsstrahlung losses is

$$t_\mathrm{brems} = \frac{\varepsilon_\mathrm{e}}{-\mathrm{d}\varepsilon_\mathrm{e}/\mathrm{d}t} \approx 4 \times 10^7 \left(\frac{n}{1\ \mathrm{cm}^{-3}}\right)^{-1} \mathrm{yrs} \quad , \tag{3.26}$$

where n is the particle number density of the ambient gas.

3.2.6 Pair production

If the energy density of very intense photon radiation is high enough, electron positron pairs can be generated. The reaction is $\gamma+\gamma \rightarrow e^+e^-$, and the process is called pair production. The cross section for this process is

$$\sigma_{\gamma\gamma} = \frac{\pi r_0^2}{\epsilon^2}\left(\left(2+\frac{2}{\epsilon^2}-\frac{1}{\epsilon^4}\right)\ln\left(\epsilon+\sqrt{\epsilon^2-1}\right)-\sqrt{1-\frac{1}{\epsilon^2}}\left(1+\frac{1}{\epsilon^2}\right)\right) \quad , \tag{3.27}$$

where the photon energy E_ph needs to be $\epsilon = E_\mathrm{ph}/m_\mathrm{e}c^2 \gtrsim 1$ in the centre of mass reference frame to produce an electron positron pair. These energies can be reached e. g. by comptonised soft photons. At the lower energy end, a cut-off occurs due to the high annihilation probability of the created pairs (Section 3.2.7).

In sources of a size R, the optical depth for photon-photon interactions at typical photon energies of $E \sim m_\mathrm{e}c^2$ is:

$$\tau_{\gamma\gamma} = n_\gamma \sigma_{\gamma\gamma} R \sim n_\gamma \sigma_\mathrm{T} R \quad , \tag{3.28}$$

where n_γ is the photon density and $\max(\sigma_{\gamma\gamma}) \approx \sigma_\mathrm{T}$.

[9] Of course this is only true, if the energy losses are dominated by bremsstrahlung. If other processes dominate, a change of the power-law spectrum can occur. In hydrogen gas, ionisation dominates over bremsstrahlung at energies below about $700\, m_\mathrm{e}c^2 \approx 350\,\mathrm{MeV}$.

Pair production is particularly important in the context of cascades in optically thick environments. These cascades are electron-photon showers,[10] which are characterised by the radiation length and the critical energy. To reach an effective multiplication of particles in a cascade, it is necessary to have energies larger than the critical energy $\epsilon \geq \epsilon_{\mathrm{crit}}$ or, in other words, the depth needs to exceed the radiation length.[11] Below this critical energy, a photon loses energy by ionisation rather than by producing more γ-rays. The inverse to photon-photon pair production is electron-positron annihilation.

3.2.7 Electron-positron annihilation

The reaction of an electron annihilating with a positron is $e^+e^- \longrightarrow 2\gamma$. Annihilation of thermalised positrons with comparatively cold thermal electrons in the ambient matter, which could be gas or plasma, manifests itself in the annihilation line at $m_{\mathrm{e}}c^2 = 0.511\,\mathrm{MeV}$.

The cross section for annihilation in the centre of mass system, where $\beta_{\mathrm{c}} = v_{\mathrm{CM}}/c$, is

$$\sigma_{e^+e^-} = \pi r_0^2 \left(\frac{1-\beta_{\mathrm{c}}^2}{4\beta_{\mathrm{c}}}\right)\left(\frac{3-\beta_{\mathrm{c}}^4}{\beta_{\mathrm{c}}}\ln\left(\frac{1+\beta_{\mathrm{c}}}{1-\beta_{\mathrm{c}}}\right) + 2(\beta_{\mathrm{c}}^2 - 2)\right) \quad . \tag{3.29}$$

So far, the processes described can appear as leptonic or as hadronic ones. Usually the leptonic type prevails, i. e. interactions of electrons and positrons dominate due to their lower mass and the dependence of the emitted power on the inverse square of the mass. But VHE γ-rays can also be produced by hadronic interactions. These are synchrotron radiation, bremsstrahlung, and inverse Compton scattering initiated by protons, but also the decay of particles like pions. In general, the unstable particles are created by hadronic interactions.

[10] This is an electromagnetic shower as described in Section 4.2.1.

[11] For hydrogen gas, the radiation length is $X_0^{(m)} \approx 60\,\mathrm{g\,cm^{-2}}$, and the critical energy is $\epsilon \approx 700\,m_{\mathrm{e}}c^2$ (Aharonian 2004).

To give a general idea as to which energy ranges are important for which kind of process, one can say that leptonic radiation processes dominate at energies lower than $E = 70\,\mathrm{MeV}$, inverse Compton processes dominate at very high energies, i. e. in the $\mathrm{GeV} - \mathrm{TeV}$ range, and in the energy range in between, hadronic processes are the dominant ones.

3.2.8 Nucleon-nucleon interactions and inelastic p-p collisions

Interactions of high energetic protons with matter or, in other words, nucleon-nucleon interactions, are mainly inelastic scattering, generating mostly mesons like pions (π^0,π^+, and π^-), but also kaons, nucleons (neutrons n and protons p) and hyperons (Δ, Λ, Σ, and Ξ). Of course, if fragments of the target nuclei survive, they can also be products of such reactions. In the collision processes, a fraction of the kinetic energy of the high energetic proton, $E_{\mathrm{kin}} = E_{\mathrm{p}} m_{\mathrm{p}} c^2$, is transferred to the secondary particle. One of the most important reactions taking place is the interaction of two protons producing a neutral pion, such as $p + A \rightarrow p' + A' + \pi^+ + \pi^- + \pi^0$, where A is a gas nucleus. To produce a π^0-meson the protons need to have a kinetic energy of more than $E = 2 m_{\pi^0} c^2 (1 + m_{\pi^0}/4 m_{\mathrm{p}}) \approx 280\,\mathrm{MeV}$, where $m_{\pi^0} = 134.97\,\mathrm{MeV}$ is the π^0-meson mass.

3.2.9 Decay of π-mesons

The decay of π-mesons, especially the decay of the neutral pion π^0, is among the most effective processes resulting in high and VHE γ-ray emission. Moreover, these decays are important processes in hadronic air shower cascades (see Section 4.2.1). The neutral pion lifetime is very short, only about $\tau_{\pi^0} = 8.4 \times 10^{-17}\,\mathrm{s}$.

The generated π^0-decay γ-ray spectrum shows a maximum at $E_\gamma = m_\pi c^2/2 \approx 67.5\,\mathrm{MeV}$, because the decay into two γ-rays with approximately identical energy, i. e. $\pi^0 \rightarrow \gamma + \gamma$, is favoured. This maximum is independent of the kinetic energy distribution of the inducing protons. The resulting total γ-ray spectrum follows the shape of the initiating proton spectrum and gives, therefore, information on the acceleration spectrum of these primary particles.

It should be mentioned that the decay of charged pions[12] produces ν_{e} and ν_μ neutrinos. The spectrum of the generated neutrinos is quite similar to the

[12] See Section 4.2.1 in the paragraph about hadronic air showers for more details like reaction equations and lifetime.

spectrum of the γ-rays produced by π^0-decay.

The emissivity of γ-rays is (Aharonian 2004)

$$q_\gamma(E_\gamma) = 2 \int_{E_{\min}}^{\infty} \frac{q_\pi(E_\pi)}{\sqrt{E_\pi^2 - m_\pi^2 c^4}} \mathrm{d}E_\pi \quad , \tag{3.30}$$

where $E_{\min} = E_\gamma + m_\pi^2 c^4 / 4E_\gamma$. It depends directly on the pion emissivity, $q_\pi(E_\pi)$, which, in turn, depends on the cross section of inelastic p-p collisions producing pions $\sigma(E_\pi, E_\mathrm{p})$.

3.2.10 Nuclear processes

Emission of high energetic γ-rays can occur when radioactive isotopes decay, mostly this happens via β decay. These radioactive isotopes are generated in supernova explosions, e. g. $^{60}\mathrm{Co} \rightarrow {}^{60}\mathrm{Ni}^{**} + e^- + \bar{\nu}_\mathrm{e}$, and the excited nickel isotope emits two γ-rays, one with an energy of $1.17\,\mathrm{MeV}$ and the other with an energy of $1.33\,\mathrm{MeV}$. These processes produce line emission and are dominant in the energy range of several hundred keV up to several MeV, and, hence, play a minor role in the production of VHE γ-rays.

3.2.11 Photon-hadron interactions

In several astrophysical environments, the radiation density is sufficiently high to exceed the density of matter by orders of magnitudes. Then, the probability of interactions between high energetic hadrons and photons is higher than that of interactions between the same hadrons and other particles.

Different photon-hadron interactions are possible, such as the already discussed inverse Compton scattering, $p + \gamma \rightarrow p + \gamma'$. Compared to the inverse Compton scattering of electrons, the proton energy loss rate is suppressed by a factor of $(m_\mathrm{e}/m_\mathrm{p})^4 \approx 10^{-13}$, and, therefore, inverse Compton scattering of protons plays a minor role in astrophysical surroundings.

Also, the second possible process, the pair production assisted by protons, $p + \gamma \rightarrow p + e^+ + e^-$, has a very small proton energy loss rate. The process is only possible, if the kinetic energy of the proton in its rest frame exceeds $\sim 1\,\mathrm{MeV}$, and it dominates only in a very small energy interval of the interacting protons, $E_\mathrm{p} \approx (1-100) \times 10^{15} (\omega_0 / 1\,\mathrm{eV})^{-1}\,\mathrm{eV}$, where ω_0 is the average energy of the target photons.

The third photon-hadron process that can take place in radiation dense regions is photodisintegration of nuclei, $A + \gamma \rightarrow A' + kN$. But the amount of high energy γ-rays produced in the wake of this process is not significant.

The most important photon-hadron interaction is the production of mesons assisted by hadrons, $p+\gamma \rightarrow p+\pi^0$, $p+\gamma \rightarrow n+\pi^+$, and generally speaking, $N + \gamma \rightarrow N + k\pi$. To induce this process, the rest frame energy of the nuclei needs to be higher than $140\,\mathrm{MeV}$. In consequence of the pion generation, first, the pions can decay and produce, besides γ-rays, also secondary electrons. But, due to the conditions of the production regions (extremely dense radiation fields), the electrons and γ-rays cannot escape from this region and induce electromagnetic cascades. As a second possibility, the secondary $\pi^{\pm}$-mesons can interact with photons, before they decay.

As a result, the lower energetic γ-rays, which are produced in the cascade and eventually escape from the acceleration region, no longer carry information about the accelerated protons. This information is or would be[13] available due to secondary neutrinos, while the γ-rays give information on the total hadronic power of the source.

An interesting upcoming idea is that the conditions in relativistic flows (like jets in GRBs and AGNs) can be responsible for the existence of the highest energy cosmic rays ($E \geq 10^{20}\,\mathrm{eV}$). The mixed hadronic/electromagnetic cascades can possibly constitute surroundings, where multiple conversion from charged to neutral states of relativistic particles proceed. Hence, they can boost protons to these extremely high energies.

3.3 Electron energy losses and cooling time

Particles lose their energy due to different radiation processes on different timescales. As an example, the electron energy-loss timescales in a SNR are calculated for typical values for the SNR shock region and the ISM: $n_{\mathrm{SNR}} = 4\,\mathrm{cm}^{-3}$, $B_{\mathrm{SNR}} = 20\,\mu\mathrm{G}$, $n_{\mathrm{ISM}} = 1\,\mathrm{cm}^{-3}$, $B_{\mathrm{ISM}} = 5\,\mu\mathrm{G}$, and an electron temperature of $T_{\mathrm{e}} = 10^8\,\mathrm{K}$. They are plotted in Figure 3.5.

It can be easily seen that Coulomb losses dominate below $100\ \mathrm{MeV}$, bremsstrahlung losses dominate near $1\ \mathrm{GeV}$, and synchrotron losses dominate above

[13] Neutrino astronomy will evolve in the coming years due to projects like IceCube and hopefully will observe adequate neutrino fluxes from 'normal' astrophysical sources on a day not long from now.

100 GeV. It is also obvious that electrons with kinetic energies near 1 GeV have the longest energy-loss timescale.

In addition, the typical photon energy emitted via a special mechanism by an electron with given kinetic energy (specified on the x-axis) is marked on the corresponding radiative loss curve. For instance, a 1 TeV electron produces X-ray emission via synchrotron radiation processes, VHE γ-rays via inverse Compton scattering ($\sim$ GeV), and bremsstrahlung ($\sim$ TeV).

If an electron source were turned off, photon emission would last a typical time depending on the radiation process. For example, radio synchrotron emission and GeV γ-ray bremsstrahlung last longest, while MeV bremsstrahlung, keV synchrotron emission, and TeV emission due to inverse Compton scattering will decrease rapidly.

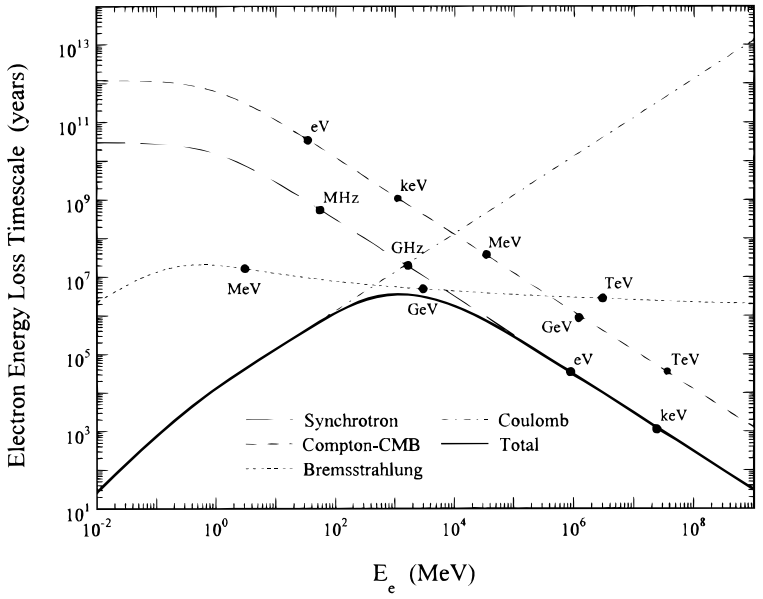

Figure 3.5: Electron energy-loss timescales $t = E/(\mathrm{d}E/\mathrm{d}t)$ due to different radiation processes for typical properties in a SNR. Plotted are losses due to synchrotron emission, bremsstrahlung, Compton scattering of the CMB (2.7 K), and Coulomb collisions. Figure from Sturner et al. (1997).

CHAPTER 4

γ-ray instruments – *H.E.S.S.* and *INTEGRAL*

X-, γ-, and VHE γ-rays as well as cosmic rays interact with particles and molecules high above the Earth's surface in the atmosphere (see Section 2.2 and Figure 2.2).

While for very high energetic γ-rays the atmosphere is used as a kind of detector, and, therefore, ground based telescopes can be used to observe the reaction products, for X- and γ-ray observations balloon flights or satellites are necessary. After a short historical outline of the evolution of astronomy in the high energies (X-ray energies and larger) and the progress of instruments in these energy ranges, the description of the two instruments *H.E.S.S.* and *INTEGRAL* follows. The focus of this thesis is the *INTEGRAL* analysis of *H.E.S.S.* sources, so the detection methods and also the *INTEGRAL* analysis method are the main subjects of this chapter.

4.1 An historical recap of high energy astronomy and instrumentation

The era of X-ray astronomy started in the early 1960's, when Riccardo Giacconi and Bruno Rossi, as pioneers in this field, searched for extrasolar X-rays. Their studies were based on rocket flight observations. The first X-ray satellite *UHURU* was then launched in December 1972. The observations of this satellite revealed many bright X-ray sources such as e. g. Her X-1 and Cyg X-1.

It is possible to focus X-rays and, therefore, image X-ray sources (see Section 2.2). This is implemented in satellites like *XMM-Newton* and *Chandra*. Telescopes observing hard X-ray/soft γ-rays are based on a so-called coded

aperture imaging system (Goldwurm et al. 2001). The principle of coded aperture imaging technique and the reconstruction of the sky images is the subject of Section 4.3.

An important advance in the field of γ-ray astronomy was the launch of the Compton Gamma Ray Observatory (CGRO) by NASA in 1991. The telescope was operational for 9 years and had four instruments on board: the Burst And Transient Source Experiment[1] (BATSE), the Imaging Compton Telescope[2] (COMPTEL), the Energetic Gamma Ray Experiment Telescope[3] (EGRET), and the Oriented Scintillation Spectrometer Experiment (OSSE). The instruments scanned the whole the sky for the first time in the wavelength range from 30 keV to $30\,\mathrm{GeV}$.

Although hundreds of point sources in the energy range $20\,\mathrm{MeV} - 30\,\mathrm{GeV}$ were detected by EGRET many of these sources are still unidentified today (Hartman et al. 1999), due to the poor angular resolution ($5 - 30\,\mathrm{arcmin}$) of this instrument. About one year ago, the launch of the satellite Fermi-GLAST once again opened the energy range from about $10\,\mathrm{MeV}$ to $100\,\mathrm{GeV}$.

In contrast to the Imaging Atmospheric Čherenkov Telescopes (IACT) these observatories observe the high energetic γ-rays directly.

For γ-ray energies higher than $100\,\mathrm{GeV}$ IACTs are used. The technique was developed between the 1960s and 1980s at the Fred Lawrence Whipple Observatory in Arizona, which operates in the energy range $100\,\mathrm{GeV} - 10\,\mathrm{TeV}$.

The first ground based detection by VERITAS/Whipple, the supernova remnant of the Crab Nebula, was announced in 1989 (Weekes et al. 1989). New generations of IACTs like VERITAS, MAGIC[4], and *H.E.S.S.* increase the number of detected and identified sources up to now to several tens of sources. More details on the detected sources and the sources types are given in Section 4.2.4.

By now, the next generation of IACTs is planned. The Čherenkov Telescope Array project (CTA) will contain ~ 100 telescopes. The improvement which this instrument is intended to achieve is an enlargement of the energy range from $20\,\mathrm{GeV}$ up to about $100\,\mathrm{TeV}$ and enhances the sensitivity by about a factor of 10.

---

[1] BATSE was an all-sky monitor sensitive in the hard X-ray energy range $20 - 600\,\mathrm{keV}$.

[2] COMPTEL (Schoenfelder et al. 1993) was operating in the soft γ-ray energy range $0.8 - 30\,\mathrm{MeV}$.

[3] EGRET was observing in the energy band from about $30\,\mathrm{keV}$ up to $30\,\mathrm{GeV}$.

[4] MAGIC contains of 2 telescopes with a facet mirror of about $17\,\mathrm{m}$ in diameter. MAGIC and VERITAS observe the northern hemisphere.

4.2 *H.E.S.S.*

4.2.1 The Imaging Air Čherenkov Technique

Every time a high energy γ- or a cosmic ray enters the Earth's atmosphere, it interacts with the particles, nuclei, and molecules in the air. The entering primary particle or photon generates secondary particles in a first interaction. Following this first interaction, the interaction products cause further interactions. Then a cascade of secondary particles called extended air shower is generated. The particle content and the morphology of the extended air showers depend on the type and energy of the primary particle. There are two types of air showers. Most extended air showers are caused by cosmic rays, which are nuclei of helium and a few nuclei of heavier elements and – mainly – protons. These give rise to hadronic cascades. A very small fraction, only about 0.2 % of all cascades, are electromagnetic showers.

Electromagnetic showers are generated by γ-rays, electrons, positrons, and high energy neutrinos. An electromagnetic cascade forms due to the radiation processes ionisation, bremsstrahlung, and pair production (see Section 3.2.5 and Section 3.2.6). The first interaction happens high above the ground, the production of particles reaches a maximum at approximately 10 km height and decreases when the shower proceeds to deeper and, therefore, denser layers of the atmosphere. The duration of such electromagnetic showers is only a few tenth of μs.

Hadronic cascades are generated when a hadron interacts with an air nucleus. The reactions are caused almost exclusively by strong interaction force and the products are in the majority of cases mesons like neutral and charged pions, kaons, nucleons and hyperons. Also fragments of the target nucleus can emerge as results of such interactions. The neutral pions decay almost immediately into two γ-rays ($\pi^0 \rightarrow 2\gamma$). The neutral pion lifetime is about $\tau_{\pi^0} = 8 \times 10^{-17}$ s. Charged pions decay into muons via $\pi^+ \rightarrow \mu^+ + \nu_\mu$ and $\pi^- \rightarrow \mu^- + \bar{\nu_\mu}$ with a muon lifetime of $\tau_{\pi^\pm} = 2.6 \times 10^{-8}$ s. The muons decay afterwards into electrons and positrons via $\mu^+ \rightarrow e^+ + \nu_\mathrm{e} + \bar{\nu_\mu}$ and $\mu^- \rightarrow e^- + \bar{\nu}_\mathrm{e} + \nu_\mu$. Therefore, hadronic as well as electromagnetic subshowers arise. It should be mentioned that, first, the longer lifetime of charged pions

increases the probability of interactions with particles in the air before they decay and second, that the muons interact less with air nuclei. Due to the larger muon mass ($m_\mu \approx 207\, m_\mathrm{e}$) they hardly lose energy due to bremsstrahlung.[5] The energy loss is mainly due to ionisation and excitation of atoms. Therefore, muons can reach the ground. For this reason the muon fraction is called the hard component of the secondary radiation. Altogether, hadronic cascades are mainly composed of three components: the electromagnetic component initialised by neutral pion decay, the strong meson component initialised by the decay of generated charged pions and the nucleonic component generated by nuclei collisions.

The showers are distinguishable due to different shower shapes and energy distributions among the particles. Since hadrons penetrate, due to their larger mass, deeper into the atmosphere and suffer more elastic collisions, the lateral extension is larger compared to the shape extension of electromagnetic showers. In addition, hadronic showers are less regular.

[5] The intensity of bremsstrahlung depends on m^{-2}.

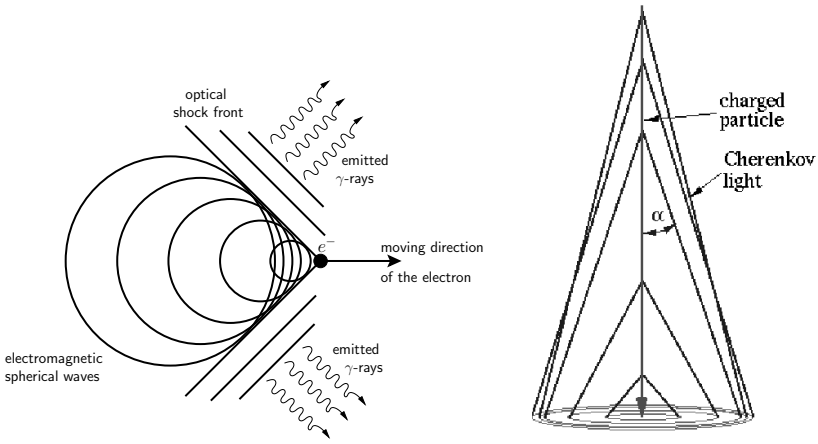

Figure 4.1: *Left* sketch: Čherenkov light is emitted when a particle moves in a medium faster than the local speed of light. Figure adapted from Grupen (2000). *Right* sketch: A Čherenkov light cone is generated with a typical opening angle of $\approx 1 - 2^{\circ}$. Figure from webpage of MPIK Heidelberg (`http://www.mpi-hd.mpg.de/hfm/CosmicRay/ChLight/Cherenkov.gif`).

Čherenkov light emission

The cosmic rays and also the secondary particles generated by an energetic γ-ray photon entering and propagating through the Earth's atmosphere have a very high velocity. They move faster in the medium than the speed of light in the medium. The light speed in air is the speed of light divided by the refractive index of the air. When a charged particle is moving in a medium faster than the local speed of light, Čherenkov emission[6] is generated. The left pattern of Figure 4.1 shows the principle of the generation of this emission and it can be illustrated as a sort of sonic boom of light. The Čherenkov light is emitted on a narrow cone around the moving direction of the particle. The characteristic angle is

$$\cos\alpha = \frac{1}{n\beta} \quad . \tag{4.1}$$

[6]The nature of Čherenkov light emission was discovered by two Russian physicists, P.A. Čherenkov and S.I. Vavilov, in 1934. Čherenkov gave his name to this kind of radiation.

Dry air has a refractive index of $n = 1.0003$ under normal conditions (Stöker 2000). Together with the limit speed of $v \sim c$, the emitting cone has an opening angle of $\alpha \approx 1.4°$. In principle, the cone of a GeV-electron has an opening angle α of less than $1.4°$, but this opening angle is a function of the density of the air and, thus, increases when the particle is propagating downwards. Since a particle emits light at every part of its track through the atmosphere, each of these parts produces a Čherenkov light ring illuminating the ground (see right pattern of Figure 4.1). The superposition of all the rings produced by all shower particles, is, in the end, the image that could be observed. The total Čherenkov light image depends on the kind of the primary particle and its energy. For example, when taking into account the above-mentioned maximum of particle production and the dependence of the cone opening angle on the air density, the observed cone extension is a function of the height where the maximum of emission is generated. Čherenkov light appears as a faint UV light observable due to atmospheric absorption as blue light with a wavelength of about $\lambda \approx 330\,\mathrm{nm}$. The spectrum depends mainly on the type of particle and the composition of the atmosphere. For a wavelength range from λ_1 to λ_2 the number of emitted Čherenkov photons per unit path length is

$$\frac{\mathrm{d}N}{\mathrm{d}x} = 2\pi\alpha z^2 \int_{\lambda_2}^{\lambda_1} \left(1 - \frac{1}{(\beta\, n(\lambda))^2}\right) \frac{1}{\lambda^2}\,\mathrm{d}\lambda \quad , \tag{4.2}$$

where $\alpha \approx 1/137$ is the fine structure constant, z is the particle charge, $\beta = v/c$ is the particle velocity, and $n(\lambda)$ the index of refraction which depends on the wavelength λ (Bernlöhr 2000). Figure 4.2 shows a typical Čherenkov light spectrum, which was calculated for the HEGRA Imaging Air Čherenkov Telescope system (*left* panel). The *right* panel displays the dependence of the number of emitted Čherenkov photons on different atmospheric models. The maximum of photon numbers occur at an altitude of about approximately 8 to $10\,\mathrm{km}$ height, also depending on the atmosphere assumed in the calculation.

A faint UV light means in this context that only about 100 photons per m^2 reach the ground, if a primary TeV energy γ-ray enters the atmosphere. The cone is directed into the original direction of the primary γ-ray. For a primary γ-ray the typical opening angles of about $1° - 2°$ illuminate an area of a circle with about $250\,\mathrm{m}$ in diameter on the ground. The time the air shower takes to arrive and, consequently, the time of a Čherenkov flash lasts only a few nanoseconds. In comparison to the almost sharp light ellipse generated by a photon, hadronic initialised Čherenkov light is a composition of many ellipses or circles generated by each shower particle so that the observed shower image

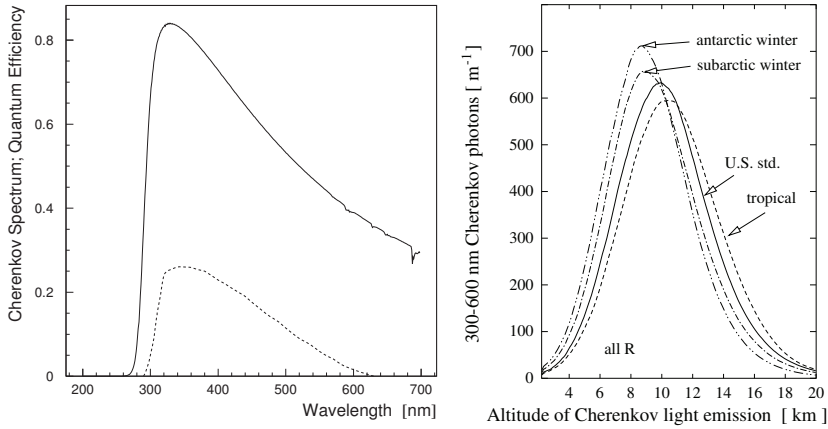

Figure 4.2: *Left* panel: A typical spectrum of Čherenkov light. The spectrum was calculated for the HEGRA Imaging Air Čherenkov Telescope system and assumed vertical TeV air showers and an altitude of 2200 m above sea level. The units are arbitrary units. In addition, the quantum efficiency of the used photomultipliers is shown (*dashed* line). Figure from Döring et al. (2001). *Right* panel: The Čherenkov light emission depends on the altitude and the conditions of atmosphere. Shown is the average Čherenkov light emission of all emitted photons along the shower axis. Assumed are vertical 100 GeV γ-rays, an altitude of 2200 m above sea level and no absorption. The calculations were made for different atmospheric profiles. Figure from Bernlöhr (2000).

is more widely spread and smeared out (Figure 4.3). Therefore, it is possible to distinguish clearly between the different primary particles.

Detection and analysing method – The Imaging Air Čherenkov Technique

Since γ-rays, as well as the electromagnetic showers they generate, do not reach the ground,[7] the observation of Čherenkov light by an IACT is the only method to observe the high energetic γ-rays (Grupen 2000). The basic principle

[7]The induced showers reach the Earth's surface when the primary photon energy is larger than 10^{15} eV. At this energy, however, only the local universe ($< 100\,\mathrm{kpc}$) is observable, because more energetic photons (> 100 TeV) interacts with the 2.7 K cosmic microwave background. This $\gamma - \gamma$-interaction causes a horizon for extremely high energy γ-ray astronomy.

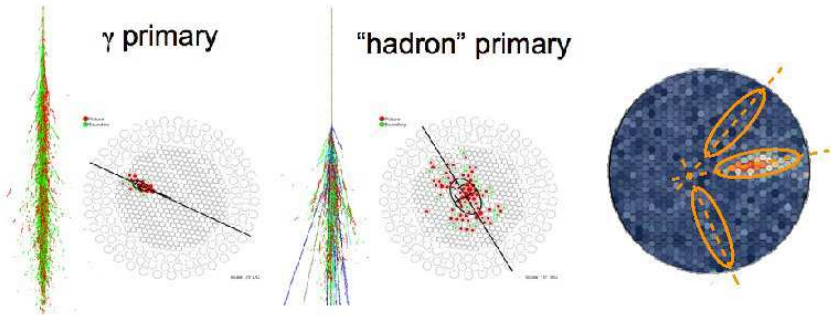

Figure 4.3: *Left:* Shower structure and Čherenkov light image for a γ-ray as primary. *Middle:* The same for a primary hadron particle. A hadronic event is obviously more widely spread than a γ-ray event. Thus the events can be easily distinguished from each other and the particle background can be suppressed for VHE γ-ray observations. The figures are from `http://veritas.adlerplanetarium.org/project/Gamma_hadron.gif`.
Right: Reconstruction principle of the sky image for an observation performed with four telescopes arranged in a square. The colour scale shows the track of the air shower of one telescope. The direction of the shower shape points back towards the origin where the initial γ-ray came from. The orange ellipses display the shower images from three telescopes and indicate the shower shape. The superposition of all direction determinations reveal the orientation of the incident γ-ray. From this information the final sky image is reconstructed. This figure is based on the figure `http://www.mpi-hd.mpg.de/hfm/HESS/pages/about/telescopes/images/detection4s.jpg` provided by MPIK Heidelberg.

of analysing observations by an IACT is to record the image of the Čherenkov light, reconstruct from these images the shower parameters and finally determine the energy, direction, and nature of the primary particle. Therefore, the telescopes need to be sensitive and fast enough to be able to detect these short and faint Čherenkov light flashes. The light flashes are collected by the large effective mirror area and are focused to the sensitive photomultipliers of the camera. The light flashes are recorded with a high timing resolution and, hence, an image of the track is obtained.

A stereoscopic reconstruction of the shower geometry is possible if one uses the multiple telescopes arrangement. The origin and energy of the primary pho-

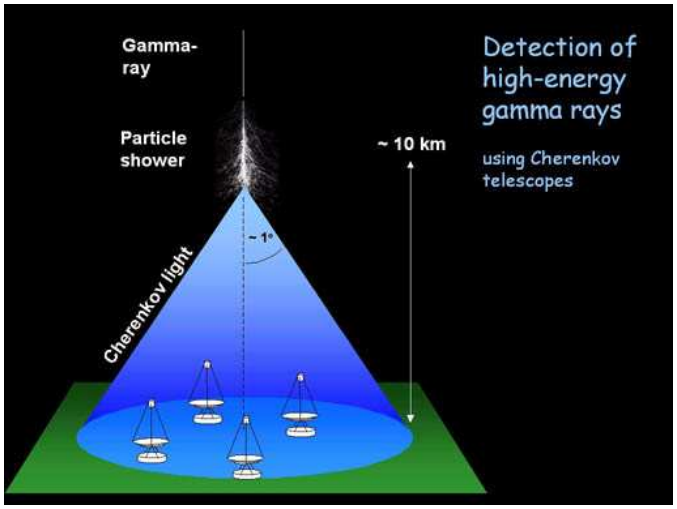

Figure 4.4: Principle of Imaging Čherenkov technique for detection of a VHE γ-ray. The particle shower induces a Čherenkov light cone which is recognised by several telescopes located in a defined area on the ground. Afterwards the sky image is reconstructed and the primary properties are calculated in consideration of the stereo images. Figure from `http://www.mpi-hd.mpg.de`.

ton can be determined in this way. The direction, where the VHE γ-ray originates from, is revealed by connecting the different information of the single telescopes. Each telescope records the track of the air shower from a slightly different direction, so the superposition of the observed tracks gives a point in the sky the primary photon came from. The energy of the primary γ-ray can be reconstructed out of the intensity of the image. Figures 4.3 and 4.4 show an image of the principle of detection with imaging Čherenkov telescopes.

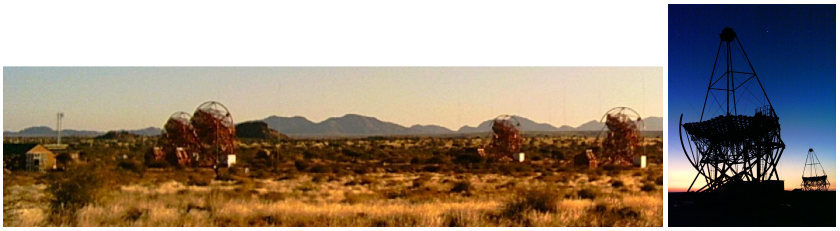

Figure 4.5: The *H.E.S.S.* telescopes. Both pictures were taken during an observation shift stay in June 2007. *Left:* The four *H.E.S.S.* Phase I telescopes are arranged in a $120\,\mathrm{m}$ square in the Khomas Highlands in Namibia. *Right:* Two telescopes during operation.

4.2.2 The telescope layout

The High Energy Stereoscopic System (*H.E.S.S.*) (Hofmann & The H. E. S. S. Collaboration 2001) is a system of four imaging Čherenkov telescopes located in the Khomas Highlands at the farm Goellschau in Namibia (see Figure 4.5). The telescopes are arranged in the corners of a square, $120\,\mathrm{m}$ by $120\,\mathrm{m}$, and are about $13\,\mathrm{m}$ high. Each telescope consists of a dish with a diameter of $12\,\mathrm{m}$ equipped with 382 individual round mirrors, $60\,\mathrm{cm}$ diameter each. The total area of the facet mirror is $107\,\mathrm{m}^2$ for each telescope. The mirrors focus the observed light onto a camera located at the primary focus at $f = 15\,\mathrm{m}$. The camera is composed of 960 photomultipliers, which cover an area of about $1.4\,\mathrm{m}$ diameter. This is equivalent to a Field of View (FoV) of $5°$. The first telescope of *H.E.S.S.* Phase I went into operation in 2002, the whole system was inaugurated in autumn 2004. The energy observed ranges from $100\,\mathrm{GeV}$ to $100\,\mathrm{TeV}$. The energy resolution is about $15\,\%$ and the angular resolution is $0.1°$ per event. The *H.E.S.S.* Phase I telescopes have a sensitivity of about $1\%\,\mathrm{Crab}$ in $50\,\mathrm{h}$ integration time.

Currently, the telescope array is being extended. *H.E.S.S.* Phase II, an additional telescope located in the centre of the square, is in preparation. It will have a diameter[8] of about $24\,\mathrm{m}$, which will reduce the the lower energy threshold to about $20\,\mathrm{GeV}$. *H.E.S.S.* Phase II is scheduled to go into operation in 2010.

[8] The dish of *H.E.S.S.* Phase II will be a rectangle which is $32\,\mathrm{m}$ high and $24\,\mathrm{m}$ wide. More information on the *H.E.S.S.* project can be found at `http://www.mpi-hd.mpg.de/hfm/HESS/`.

4.2.3 Operating mode

One of the main challenges when observing the faint Čherenkov light of particle showers in the atmosphere is to reduce the background. In fact, there are two different backgrounds, which should be reduced.

Most of the up to 300 air showers, that can be observed by the telescopes every second, are generated by cosmic rays atomic nuclei that enter the atmosphere. Fortunately, one can distinguish between the different initiating particles due to the image structures they create in the camera.

Next to this cosmic ray background, there is the background in the optical range. To observe the faint Čherenkov light all distracting sources of optical light need to be suppressed. Therefore, an isolated telescope site had been chosen and only operation on moon-less nights is possible. Furthermore, it is essential, that the integration time intervals are very short, because otherwise the faint Čherenkov flashes would be drowned in the background light of night sky (Rosswog & Brüggen 2007).

Hence, two technical issues need to be solved to ensure proper observations. Due to the low fluxes in this energy range the collection area needs to be large. Therefore, the total facet mirror area which focuses the incident light on the light detector (the camera), needs to be large enough to collect a sufficient number of photons. It is also necessary that the camera has a fast enough response.

In the end *H.E.S.S.* can schedule $1\,000$ hours of observation each year. The observations are separated into so-called runs with about 28 min length. While the strongest γ-ray sources can be detected with a few minutes of observation time, fainter sources need observations with an integration time of tens of hours.

The main task of the analysis software is to reject the unwanted signals from cosmic rays and select the tracks of γ-rays. This is done in situ to get a first impression of data quality and afterwards in a final analysis with different software packages.[9] The analysis software compares the observed data with results of Monte Carlo simulations of air showers of several types of particles.

[9]The different software packages are developed at several institutes that are part of the *H.E.S.S.* collaboration.

4.2.4 Results – A new observable window to the universe

The very successful VHE γ-ray telescopes *H.E.S.S.* and MAGIC opened a new observable window to the universe. Due to the good sensitivity and the large FoV it was possible to image our Galaxy in very high γ-rays. In the process, it was possible to detect individual sources and in some cases identify them afterwards due to follow-up multi-wavelength observations. This started a new era of astronomy,[10] the VHE γ astronomy. This new energy range provides new knowledge of the non-thermal processes and particle acceleration taking place in the universe. Hence, astronomical observation can contribute to give additional insight into fundamentals of physics, e. g. to the still open questions in particle physics. Astronomical sources that are observed in the VHE regime are accelerators of cosmic particles. So the γ-rays, generated in the surroundings of the accelerators, travel unhindered through the universe, and hopefully observed by IACTs, can image the accelerator sides.

Figure 4.6 shows the inner part of the Galactic plane in VHE γ-rays (Aharonian et al. 2006b). The sources detected with *H.E.S.S.* in the Galactic region are Supernova remnants like RX J0852.0−4622, the so-called Vela Junior, binaries like PSR B1259−63 or LS 5039 (see Chapter 5), pulsar wind nebulae like MSH 15−52 (see Chapter 8), and AGN like the first AGN detected, the BL Lac object Mkn 421, as extragalactic sources. Today, in total, *H.E.S.S.* proclaims 54 VHE γ-ray sources; about 25 are extragalactic sources.[11] For actual catalogues have a look at the *H.E.S.S.* Source Catalog[12] or a total catalogue of VHE γ-ray sources[13] detected by currently operating IACTs and listed by R. Wagner from the 'Max-Planck-Intitut (MPI) für Physik' in Munich.

[10] Of course there were experiments operating before *H.E.S.S.* and MAGIC, but for doing astronomy it is necessary to identify the observed sources. Therefore, good angular resolution is essential. *H.E.S.S.* and MAGIC go one step further than previous telescopes.

[11] The VHE AGN are mainly blazars but also two radio sources are verified.

[12] `http://www.mpi-hd.mpg.de/hfm/HESS/pages/home/sources/`

[13] `http://www.mpp.mpg.de/~rwagner/sources/`

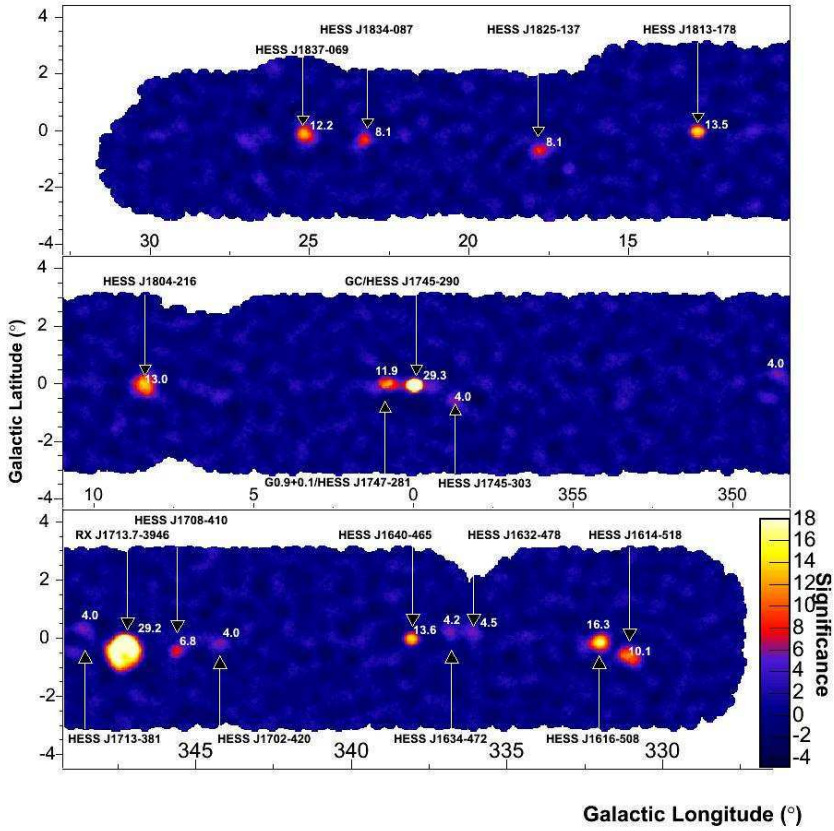

Figure 4.6: The *H.E.S.S.* survey of the inner Galaxy in very high energy γ-rays. Shown is the significance map which is truncated at a significance of $18\,\sigma$. The numbers given in the map for the single sources are post-trial significances. Most sources appear as extended sources, e. g. obvious at the supernova remnant RXJ 1713.7−3946 and the Galactic centre. The observations were made during the Galactic plane survey in 2004 and re-observations of single sky regions afterwards. The energy threshold is typically 250 GeV. Figure from Aharonian et al. (2006b).

4.3 *INTEGRAL*

4.3.1 The satellite

The International Gamma-Ray Astrophysics Laboratory, named *INTEGRAL*, (Winkler et al. 2003) is a medium sized ESA γ-ray space mission and was launched on 17th of October 2002 from Baikonur/Kazakhstan. *INTEGRAL* is still, beside the Japanese satellite *Suzaku* ($0.2 - 600\,\mathrm{keV}$, launched on 10th July 2005) and Fermi-GLAST ($8\,\mathrm{keV} - 300\,\mathrm{GeV}$, launched on 11th June 2008), one of the major instruments exploring the sky in the hard X-ray/soft γ-ray domain. A main challenge for the *INTEGRAL* satellite was the regular scan of the Galactic plane (GPS).[14] In addition, a focus of the scientific programme is the exploration of the Galactic centre region, realised in the Galactic Centre Deep Exposure (GCDE) (Winkler 2001).

The orbit of *INTEGRAL* is highly eccentric with a period of $72\mathrm{h}$. In the following paragraphs an overview of the instruments on board and of the analysis procedure is given. Figure 4.7 shows an artist's impression of the satellite. A detailed description of the instrument can be found in Winkler et al. (2003).

On board configuration

Four scientific instruments are on board the *INTEGRAL* satellite:

- the *Spectrometer on INTEGRAL* (SPI, $20\,\mathrm{keV} - 8\,\mathrm{MeV}$, Vedrenne et al. 2003),
- the *Imager on-Board INTEGRAL Satellite* (IBIS, $15\,\mathrm{keV} - 10\,\mathrm{MeV}$, Ubertini et al. 2003),
- the *Joint European X-Ray Monitor* (JEM-X, $3 - 35\,\mathrm{keV}$, Lund et al. 2003),
- and the *Optical Monitoring Camera* (OMC, Mas-Hesse et al. 2003).

The two main γ-ray instruments, SPI and IBIS, have good spectral and angular resolution, but are differently optimised. In total, an energy range from

[14] Since the 6th Announcement of Opportunity (AO-6) this regular scan was omitted in favour of observations of the Core region and observations of specific targets.

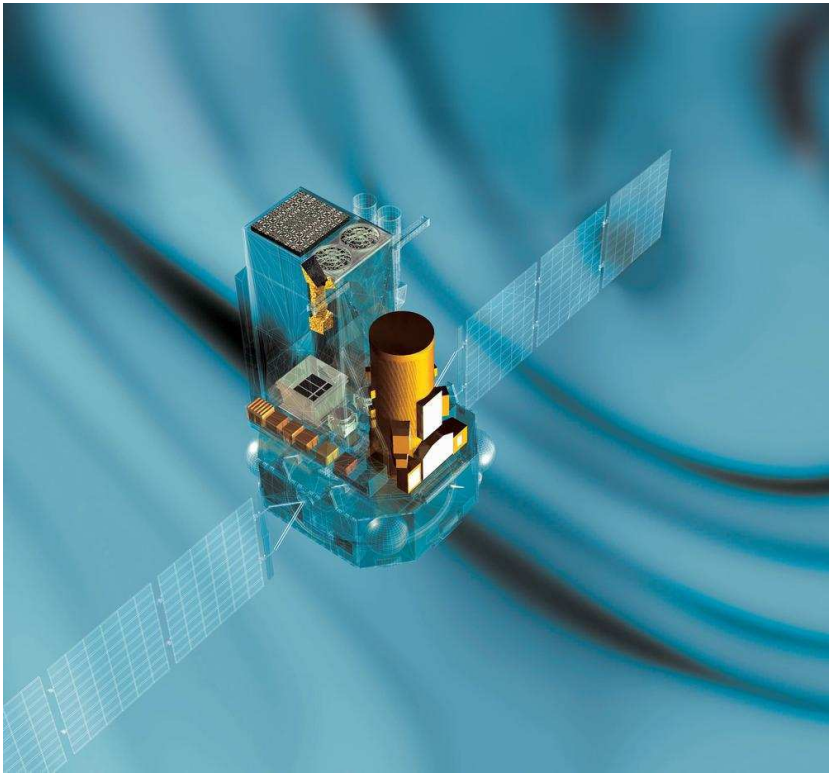

Figure 4.7: The *INTEGRAL* satellite in a partly transparent artist's impression. The yellow tube is the SPI instrument. Behind SPI the rectangular tube of the two JEM-X telescopes and the IBIS instrument is disposed. The coded mask of IBIS as well as the detector plane is visible in this picture. The small yellow tube next to the JEM-X is the OMC. The figure is from `http://isdc.unige.ch/index.cgi?Home+images`.

$\sim 3\,\mathrm{keV} - 10\,\mathrm{MeV}$ is covered. The spectral energy resolution of SPI is $3\,\mathrm{keV}$ at $1.7\,\mathrm{MeV}$ and for IBIS $8\,\mathrm{keV}$ at $100\,\mathrm{keV}$.

In the following short summary I focus on IBIS/ISGRI, because in this thesis only data of this instrument and detector are used. Details for the other detector and the other instruments can be found in several articles (Ubertini et al. 2003; Winkler et al. 2003; Goldwurm et al. 2001).

IBIS provides high-resolution sky images, i. e. a fine angular resolution of about $12\,\mathrm{arcmin}$ (FWHM), with an extension of $29^\circ \times 29^\circ$ for a declined sensitivity of zero at the edges, in an energy range from $15\,\mathrm{keV}$ to $10\,\mathrm{MeV}$. The FoV has to be distinguished into two parts: the fully coded FoV (FCFOV) and the partly coded FoV (PCFOV), which span $8^\circ \times 8^\circ$ and $19^\circ \times 19^\circ$ at half sensitivity, respectively.[15]

The coded mask used for IBIS is a $16\,\mathrm{mm}$ thick tungsten mask with a dimension of about 1 square meter. One half each of the cells is opaque and 'open' to photons in the operational energy range. The mask pattern is optimised for high angular resolution. The detector plane located at a distance of $3.2\,\mathrm{m}$ below the mask consists of two detectors: ISGRI and PICsIT.

ISGRI (Lebrun et al. 2003) is a multilayer CdTe semiconductor detector. The 128×128 pixels, each with dimension $4 \times 4 \times 2\,\mathrm{mm}$, provide a detector area of $\approx 2600\,\mathrm{cm}^2$. This detector array is optimised for low energies, i. e. $15 - 1000\,\mathrm{keV}$. The second detector of IBIS is sensitive to higher energies between $0.175\,\mathrm{MeV}$ and $10\,\mathrm{MeV}$ and is located $94\,\mathrm{mm}$ below the ISGRI plane. Unfortunately, the background is very high for this detector, so that the analysis of PICsIT data is complicated and not qualified for faint sources. ISGRI and PICsIT are surrounded by an anticoincidence VETO System. This is necessary to minimise the background. As already mentioned, in this energy range the environment in space is strongly dominated by high energy protons and electrons. The sensitivity that is reached with *INTEGRAL* in an integrated overall exposure time of $10^6\,\mathrm{s}$ is about $1\,\mathrm{mCrab}$ at $100\,\mathrm{keV}$ ($3\,\sigma$ detection). The two additional instruments JEM-X and OMC are monitoring instruments in the X-ray and optical range, respectively.

4.3.2 Analysis method and coded mask technique

The coded mask technique is conceptually very simple. A mask consisting of equal-sized transparent and opaque areas arranged in a specific pattern projects a shadowgram onto the detector plane, where it is recorded. The images of the sky are reconstructed afterwards by decoding the recorded detector shadowgram with the mask pattern. This is easy, when only one source is in the FoV,

[15] Fully coded Field of View (FCFOV) is the sky region where radiation of all sources directed towards the detector plane is modulated by the mask. In comparison, only the radiation of a fraction of the sources directed towards the detector plane is modulated by the mask in the case of partially coded FoV (PCFOV). The FoV depends on the dimension of mask, detector and the distance between both, of course.

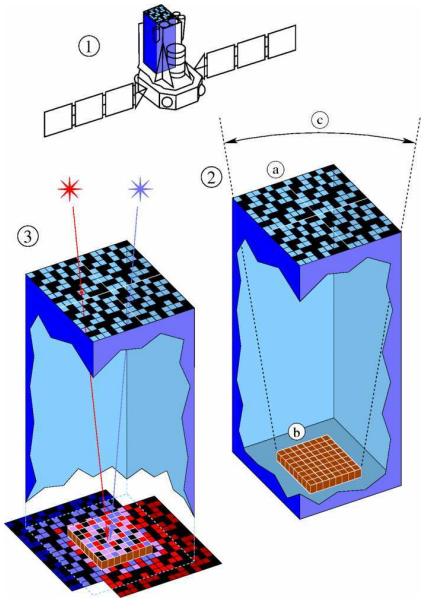

Figure 4.8: Principle of coded mask technique as it is implemented in the *IBIS ISGRI* instrument. Sketch 1 shows the location of the *IBIS* instrument on board the *INTEGRAL* satellite. In sketch 2 the size of the mask (a) and the detector (b) and the distance between the two layers define the sky angle (c) of the fully coded field of view (FCFOV). In the sketch 3 the overlapping of the shadowgrams cast by two stars (blue and red) onto the detector is shown. The Figure is from `http://isdc.unige.ch/index.cgi?Home+images`.

but becomes complicated if there are many sources in the observed sky region. Figure 4.8 shows the principle of the coded mask technique.

More precisely, photons originating from a point source or from a diffuse emitting sky region in the field of view (FoV) project a shadow image of the mask on the detector, equal in structure but displaced by an offset to the corresponding in-falling direction and also different in strength, which corresponds to the brightness of the sources. The sum of all the shadows produced by all sources in the FoV of the telescope, is measured by the detector and needs to be deconvolved again to reconstruct the image of the sky. The detector needs

to be sensitive in position and needs to have a spatial resolution which is sufficient to match the mask-pattern grid size. To get a reliable sky image at the end, it is necessary that each source produces a distinctive shadow pattern on the detector, i. e. that the unambiguous encoding of the sky position is feasible.

The Standard IBIS/ISGRI science analysis procedure comprehends the reconstruction, cleaning, and combining of IBIS/ISGRI sky images. The Offline Scientific Analysis (OSA) is the official analysis Software package of *INTEGRAL*. The first step is the image reconstruction for each single Science Window, a step in the code called IMA. Included in the IMA step, or also executable as a separate operation by rerunning the IMA step on a list of already reconstructed ScW[16] images, is the mosaic building step. In this step the single reconstructed ScW are rotated and added up to an overall sky image. The final ISGRI mosaic image is sampled into pixels of $5'$ size. After building the mosaic a search for point-like sources is performed. The detected and identified (due to comparison with the INTEGRAL Reference Catalog) sources are stored in a source list.

Continuative, spectra and light curves for the detected sources can be established. This procedure is based on simultaneous fitting of sources and background shadowgram models to the detector images.

In Ubertini et al. (2003) the OSA analysis is described in detail. Only a few generic aspects (Goldwurm et al. 2001), important for the analysis of LS 5039 (see Chapter 6) should be mentioned in the following paragraphs.

To get rid of the background that dominates the count rate in the γ-ray domain, an inversion of the shadow building leading to a distinctive image of the mask on the detector is used. The simultaneous measurement of source and background is possible, since, roughly spoken, the transparent mask elements observe source plus background while the opaque elements observe only the background. The design of the mask pattern is such that for sources in the fully coded FoV the shadowgram is unique. Summarised in an equation the recorded image on the Detector is equal to the sky modulated by the mask plus the detector background:

$$\mathrm{Detector} = \mathrm{Sky} * \mathrm{Mask} + \mathrm{Background} \tag{4.3}$$

Detector, Sky, Mask and Background can be described as matrices which are stored in the OSA code as arrays. Therefore, Equation 4.3 can also be understood as a mathematical equation.

[16] A 'Science Window' (ScW) is the elementary observation interval of *INTEGRAL* and lasts about 1 800 s.

The assembling of the mask is of crucial importance. *INTEGRAL* uses a so-called Modified uniformly redundant array (MURA) (Gottesman & Fenimore 1989), a total mask pattern based on cyclic replication of the same basic pattern. The advantage of a MURA mask pattern is, due to the relatively simple correlation between the mask array and the detector array, the deconvolution which provided a sky image in which point sources appear as spikes with flat sidelobes. The size (FWHM) of these spikes is approximately one projected mask element, which is in the case of ISGRI/IBIS a size of about 12'.

So, it is, in principle, possible to reconstruct (deconvolute) the sky image, when one knows the mask pattern and knows or at least assumes the background. In the ideal case, there are only sources in the fully coded field of view, which then cast a unique shadowgram each on the detector, respectively. Thus, no ambiguities arise and an unambiguous reconstruction of the sky image is possible. Of course, in reality other sources that are only partially coded are in the surroundings. These sources induce so-called ghost sources.

It is possible to extend the discrete deconvolution valid in the FCFOV to the total field of view (FC+PC)FOV. Next to the source peak, eight main ghosts of the source peak appear in the deconvoluted image. These 'ghost sources' are placed at distances as multiples of the mask basic pattern in the PCFOV.

To get a sky image that is totally cleaned of ghost sources, it is necessary to take all sources into account that contribute somehow to the image. For crowded sky regions like the Galactic plane, this is impossible due to limitations in computing time and space.

An observation performed by *INTEGRAL* is divided in an elementary observation interval, called 'Science Window' (ScW). If the telescope is pointing towards a specific source the ScW is declared as 'pointing', if the telescope moves towards another source the declaration of the ScW is 'slew'. During image reconstruction an exposure map is also computed, which is an array of exposures for each pixel, calculated from information of good time intervals (GTI), gaps of telemetry or data, deadtimes, lifetime of each pixel, and low energy thresholds.

After deconvolution of the sky image, a search for sources takes place. The search for sources is an iterative process that looks for significant peaks in the image. This iterative process proceeds in the following way: once a source is identified, a model of the shadowgram projected onto the detector plane by the source at the derived position is computed. The resulting model detector image is decoded and normalised to the observed excess. Finally this model image is subtracted from the sky image. The user handling the OSA can influence the

source detection by setting the signal-to-noise level (S/N) of detection or giving an input catalogue of known sources. The level of S/N as well as the choice of the input catalogue is a very sensitive process.

After the single pointing science windows are reconstructed and cleaned to single sky images, they are added up to a mosaic image. Therefore, they are rotated, projected over a reference image (which is the first ScW of the ScW list) and summed, taking into account a proper weighting of their variance and exposure time. When the mosaic step is finished once again the point source searching routine is executed on the composite sky image. An input catalogue can be specified again. Source identifications are based on this input catalogue or on the IBIS/ISGRI Reference Catalogue[17] provided by ISDC. As a result a list of all detected and possibly identified sources, including positions and observed fluxes, is exported to a FITS-file.

Moreover, it is possible to start the mosaic step separately, which is recommended for large ScW lists and for crowded FoVs, where the input catalogue needs to be carefully aligned. If the catalogue is not appropriate, structures can appear in the images or pseudo new sources can be detected.

In the Standard OSA procedure the image building is followed by the spectrum and light curve extraction. Based on the determined source positions an extraction of source fluxes and spectra can be performed for each ScW. For this spectral extraction the same routine, which computed the model of the source shadowgram on the detector plane, is used. The parameters of each source, position, flux, and significance are fitted. It is possible for the user to fix the position of a source. This is especially important for transient and for faint sources, which are not detected in each ScW. The energy bins the spectra are extracted in, are fixed, but it is, in principle, possible to rebin by changing the default values. However, it is important to fit all active sources in the FoV simultaneously. Thus, contamination of the interested spectrum by other sources can be avoided. All spectra of one source in each single ScW are added up to an average spectrum. The production of light curves is continued in a similar procedure to the spectral step, it only differs in the number of energy bands and number of time intervals. The final results are a spectrum and a light curve for each source in the spectral source catalogue.

The spectral and light curve extraction can be complicated, especially for sky regions with many sources. The procedure is based on simultaneous fitting

[17] The Reference Catalogue is provided by the ISDC and available at `http://isdc.unige.ch/index.cgi?Data+catalogs`.

of source and background shadowgram models to the detector images (Goldwurm et al. 2003) and, therefore, depends on the number of sources that are contemporaneously fitted. The analysed FoV in Chapter 5 includes more than 65 sources.

Limitations of Analysis

In principle, it could be that ScWs are not correctly reconstructed. In cases of wrong deconvolution single ScW can show structures, like e. g. a chequerboard pattern. The problems appear mainly, if ScWs of crowded sky regions are deconvolved. This holds true, especially for regions near the Galactic centre and is not difficult to understand, since every source produces one shadow which superimposes with every shadow of all other sources. For such sky regions it is recommended to look at each single ScW image. This, of course, enhances the needed disc space and computing time exponential. The Standard OSA procedure has, therefore, a significance limit for automatically detected sources for each ScW of $6\,\sigma$, i. e. only about $3-5$ sources are bright enough to be detected with this significance in an exposure time of about 30 min. When these images are superimposed, 'ghost sources' could appear, because the single ScWs were not cleaned by the fainter sources, which, after being added up, appear in the mosaic. Hence, the single ScW needs to be extracted with an external catalogue of all sources, which have significances larger than 6σ in the mosaic. The only way to produce such a catalogue is to build it up iteratively on the basis of the IBIS/ISGRI Reference Catalogue. It makes sense to use positions from the Reference Catalogue, but not the whole Catalogue, because there are many sources listed, which are too faint for *INTEGRAL*. Since the spectral extraction requires the simultaneous fitting of all sources brighter than the source interested in, the results for crowded fields and, hence, large numbers of simultaneous fitted sources, may be not fully reliable. Because of that the Standard procedure of OSA has a limit of 30 sources to extract in the computational step of spectrum creation. Thus, a larger catalogue needs to be used and, in the end, a cross-check with the results of the image reconstruction is advisable.

CHAPTER 5

A TeV binary – LS 5039

5.1 The System LS 5039

The binary LS 5039 is one out of only four TeV emitting X-ray binaries. All members of this very small object group are listed and briefly discussed in Section 2.5.

The multi-wavelength range for emitted and observed information on the high mass X-ray binary system LS 5039 / RX J1826.2−1450 extends from radio to γ-rays. After introducing the system itself, I summarise the observations of this source made in several energy ranges in Section 5.2. One of the still open questions concerning this binary is the powering source of the multi-wavelength emission. It is either accretion in a microquasar system or wind interaction in a system containing a young non-accreting pulsar. These two possibilities of interpretation are discussed in Section 7.3. Also the nature of the compact object is still under debate.

The optical component of the HMXRB is the bright variable star named LS 5039 or also V479 Sct in the small constellation Scutum in the northern sky.[1]

Based on optical photometry in the B and V bands, Casares et al. (2005b) calculate the distance of LS 5039 to be $d = 2.54 \pm 0.04\,\mathrm{kpc}$. Earlier calculations provided values up to $d \approx 3.2\,\mathrm{kpc}$ (e. g. Motch et al. 1997; Clark et al. 2001). As a lower limit, McSwain et al. (2004) determined a distance of $d \approx 1.9\,\mathrm{kpc}$ by observing the reddening and comparing it with nearby stars in the line of sight.

[1] This counterpart gave its name to the whole binary. The brightness in the optical wavelength range is $V \sim 11.32$ (Clark et al. 2001).

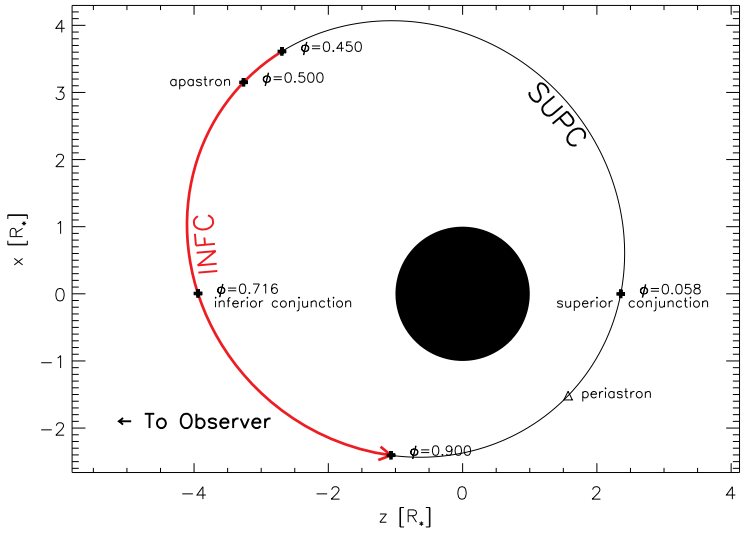

Figure 5.1: A sketch of the system. Orbital values are taken from Casares et al. (2005b) and are listed in Table 5.1. The definition of the phase intervals follows Aharonian et al. (2006c).

By employing radial velocity measurements of optical absorption lines, a determination of the system parameters was possible (see e. g. Casares et al. 2005b; Aragona et al. 2009). One of the main issues to understand a binary system is the determination of its orbital period. For LS 5039, the identification of the orbital period was not easy. First, Clark et al. (2001) excluded orbital modulations between three and fifteen days from optical and near-IR photometric and spectroscopic observations. High-resolution spectroscopic studies (with a resolution of $\lambda/\delta\lambda = 4000$ and $\lambda/\delta\lambda = 9000$, respectively) enabled McSwain et al. (2001) to reveal a short orbital period of $P_{\rm orb} = 4.117 \pm 0.011\,{\rm d}$, a highly eccentric orbit with $e = 0.41 \pm 0.05$, and a quite low mass function of $f(m) = 0.00103 \pm 0.00020\,{\rm M}_{\odot}$. The mass function points to a neutron star (NS), but does not rule out the possibility of a black hole (BH) as compact object, if the inclination were low. In further and advanced spectroscopic studies, Casares et al. (2005b), McSwain et al. (2004), and recently Aragona et al. (2009) determined the currently accepted orbital parameters listed in Table 5.1. Figure 5.1 shows a sketch of the system based on the parameters determined

by Casares et al. (2005b). In particular, the orbital period of $P_{\rm orb} = 3.903\,{\rm d}$ seems to be the correct one in the end (Aragona et al. 2009).

The inclination of the system is not yet known accurately. The lower limit of $i > 9^\circ$ is given by the limitation of the rotational speed of the optical star (McSwain et al. 2001), because exceeding this velocity would result in a breakup. On the other side, the lack of X-ray eclipses implies an upper limit of $i < 64^\circ$ (Aharonian et al. 2006c) for the inclination. Recent measurements claim a range from $i = 11^\circ$ to $i = 75^\circ$ (Moldon et al. 2009).[2]

The inclination directly affects the calculation of the mass of the compact object. For example, if the compact object is a NS, the inclination angle needs to be between $i = 40^\circ$ and $i = 60^\circ$ (Combi et al. 2004). If the compact object is a BH, the inclination angle should be lower. For instance, if the inclination is $i \approx 9^\circ$, the compact object would have a mass of $M_{\rm co} < 8\,{\rm M}_\odot$ (Martocchia et al. 2005).

Typically, stars of spectral type O6.5V((f)) have masses of about $M_\star \approx 40\,{\rm M}_\odot$ and radii of about $R_\star \approx 10\,{\rm R}_\odot$ (Howarth & Prinja 1989). The mass of the star LS 5039 is in the range of $M_\star = 20 - 35\,{\rm M}_\odot$ (McSwain et al. 2004). This is consistent with the discovery by Kaper (2001) that OB stars which are a component of an X-ray binary, are undermassive compared to single stars of the same spectral type. Recent calculations from the newest orbital parameter determination yield a mass of the optical star of $M_\star = 23\,{\rm M}_\odot$ and, thus, lead then to two possible natures for the compact object: a NS with a mass of $M_{\rm co} = 1.4\,{\rm M}_\odot$ or a BH with a mass of $M_{\rm co} = 3.7\,{\rm M}_\odot$ (Aragona et al. 2009). This is also consistent with the range that Moldon et al. (2009) give for the compact object mass ($M_{\rm co} = 1.5 - 8\,{\rm M}_\odot$).

The wind terminal velocity is $V_\infty = 2449 \pm 190\,{\rm km\,s^{-1}}$ (McSwain et al. 2004). This is well within the range of typical velocities of O-type star winds ($V_\infty = 2\,000 - 3\,000\,{\rm km\,s^{-1}}$, Kaler 1994). From the strength of emission in Hα, it is possible to derive the strength of the stellar wind and, hence, the mass-loss rate (Puls et al. 1996).[3] This is important when thinking about the accretion mechanism present in the system. In LS 5039, most likely a wind powered mechanism is present.

---

[2]The inclination angle i is defined so that an observer sees the system edge-on at an inclination angle of $i = 90^\circ$.

[3]Based on the observational equivalent width W_λ of Hα, Puls et al. (1996) show, how the Hα profile in O stars grows from a pure absorption feature to a broad and strong emission line with increasing stellar wind mass-loss rate.

Table 5.1: Orbital and system parameters of the binary LS 5039 (Casares et al. 2005b; Aragona et al. 2009) and phase interval definitions (Aharonian et al. 2006c). The values of Casares et al. (2005b) are used in the *INTEGRAL* analysis, the values of Aragona et al. (2009) are the most recent ones. Periastron passage is at T_0 at phase $\phi = 0.0$. Values marked with ^{b} are from Moldon et al. (2009).

	(Casares et al. 2005b)	(Aragona et al. 2009)
$P_{\rm orb}$ [d]	3.90603 ± 0.00017	3.90608 ± 0.00010
T_0 [HJD]	$2\,451\,943.09 \pm 0.10$	$2\,452\,825.985 \pm 0.053$
e	0.35 ± 0.04	0.337 ± 0.036
ω [°]	226 ± 8	236.0 ± 5.8
K_1 [$\mathrm{km\,s^{-1}}$]	19.4 ± 0.9	19.74 ± 0.86
$a_1 \sin i$ [$\mathrm{R_\odot}$]	1.42 ± 0.07	1.435 ± 0.066
$f(m)$ [$\mathrm{M_\odot}$]	0.0025 ± 0.0004	0.00261 ± 0.00036
i	$13° < i < 64°$	
d [kpc]	2.5 ± 0.1	
INFC	$0.45 < \phi \leq 0.90$	
SUPC	$0.90 < \phi \leq 1.45$	
$R_\star$ [$\mathrm{R_\odot}$]	$9.3^{+0.7}_{-0.6}$	
$= R_\star$ [cm]	$\approx 7 \times 10^{11}$	
$M_\star$ [$\mathrm{M_\odot}$]	$22.9^{+3.4}_{-2.9}$	
$\log(L_{\rm opt}/\mathrm{L_\odot})$	5.26 ± 0.06	
$L_{\rm opt}$ [$\mathrm{erg\,s^{-1}}$] ^{b}	7×10^{38}	
$\dot{m}_w$ [$\mathrm{M_\odot\ yr^{-1}}$] ^{b}	7×10^{-7}	
$M_{\rm co}$ [$\mathrm{M_\odot}$] ^{b}	$1.49-1.81 < M < 8-10$	
i *	$24\overset{\circ}{.}9 \pm 2\overset{\circ}{.}8$	
$M_{\rm co}$ [$\mathrm{M_\odot}$] *	$3.7^{+1.3}_{-1.0}$	

* From the dynamical solution in combination with the assumption of pseudo-synchronisation (Casares et al. 2005b).

This was suggested by Paredes et al. (2002), who folded the optical light curve with the orbital period (in this case the former period of $P_{\rm orb} = 4.117\,{\rm d}$). No modulation has been seen, which affects the conclusion that either the optical companion underfills its Roche lobe or the orbital inclination is very low.

The former was confirmed by the lack of significant emission lines, especially of $\rm H\alpha$ emission, which would have been an indicator of high mass transfer rates via Roche-lobe overflow (McSwain et al. 2001; McSwain & Gies 2002). There was no evidence of spectral variation with orbital phase in the optical observations, which establishes the wind of the primary as the region where the weak emission lines in the spectrum are formed and, hence, accretion through capture of the primary's stellar wind flow and not through an accretion stream. Additionally, this is supported by the fact that the radius of the optical star is far from the critical Roche-lobe radius at periastron in all models.

The progenitor of the compact object has lost a large amount of mass at the end of its life during a supernova explosion. $5\,{\rm M}_\odot$ to $17\,{\rm M}_\odot$ have been lost, which is more than 81 % of the mass of the pre-supernova star (McSwain & Gies 2002).[4]

The LS 5039 system is moving away from the Galactic plane with a systemic velocity of $v_{\rm system} \approx 150\,{\rm km\,s^{-1}}$ (Martí et al. 2004; Combi et al. 2004), including a component perpendicular to the plane that is larger than $v_\perp = 100\,{\rm km\,s^{-1}}$ (Ribó et al. 2002). This is a direct consequence of the SN explosion (Section 2.4).

Interstellar and intrinsic absorption is detected in observations of LS 5039 in several wavelength ranges. Most of the interstellar absorption takes place below $E = 2.5\,{\rm keV}$. Therefore, the difference between the extinction obtained by optical observations and the one obtained via X-ray observations like BeppoSAX might be caused by the different sensitivity of the optical photometric indicators and the hydrogen column density determined from X-ray observations to the different types of absorption: atmospheric, interstellar, and intrinsic (Reig et al. 2003). Different X-ray observations of LS 5039 show slightly different values of the photoelectric absorption from $N_{\rm H} = 0.70 \pm 0.05 \times 10^{22}\,{\rm cm^{-2}}$ (Martocchia et al. 2005) up to $N_{\rm H} = 1.0^{+0.4}_{-0.3} \times 10^{22}\,{\rm cm^{-2}}$ (Reig et al. 2003). This value is consistent with the values obtained from optical reddening (see e. g. Motch et al. 1997). Hence, there might be a local absorption, but this could not be very high, at least at the observational epochs, e. g. during the *XMM-Newton* observation (Martocchia et al. 2005). The reason for the

[4]For comparison, a star loses typically a fraction of 35 % in a SN (McSwain & Gies 2002).

slight variability in absorption column may be inhomogeneities in the velocity and/or the spatial distribution of the stellar wind. Other wind-fed accreting systems show changes in the hydrogen column density too, e. g. the X-ray pulsar binary system GX 301−2 (White & Swank 1984).

5.2 Multi-wavelength observations

During the last decade, the binary LS 5039 / RX J1826.2−1450 was the target of many observations in nearly all energy bands, which were performed by several instruments and telescopes. The great interest in this source started when Motch et al. (1997) systematically cross-correlated the positions of OB catalogue stars in the SIMBAD Astronomical Database[5] and a selected part of the ROSAT all-sky survey (RASS) that included the early type OB stars. Associating the bright catalogue star LS 5039 with the source RX J1826.2−1450 observed with the *Röntgensatellit* ROSAT, these authors proposed the system LS 5039 / RX J1826.2−1450 to be a new massive X-ray binary. Shortly after, Marti et al. (1998) observed a bright and unresolved radio source, whose position was consistent with both the optical and the X-ray position. The source has been, therefore, identified as one of the few radio emitting HMXRBs that constitute a new class of objects: the radio-loud high mass X-ray binaries.

Radio

The radio range is the lowest energy band in which LS 5039 was detected (Marti et al. 1998). The unresolved radio emission appeared persistent and non-thermal as well as variable and without strong radio outbursts (Ribó et al. 1999). McSwain et al. (2001) reported also a non-thermal radio emitter and associated the radio emission with the binary. The origin of the radio emission is synchrotron radiation from particles accelerated to high energies (Aharonian et al. 2005b). Observations with EVN and MERLIN enabled Paredes et al. (2002) to resolve the radio emission into a bipolar emission emanating from the central core. Recently, Moldon et al. (2009) have published new analyses of $\lambda = 5\,\mathrm{GHz}$ observations from June 2000 at VLBA (Very Long Baseline Array) and VLA (Very Large Array) of the National Radio Observatory (NRAO).

[5]The SIMBAD Astronomical Database is available at
`http://simbad.u-strasbg.fr/simbad/` .

These observations also show that the resolved radio emission can be separated into a core component with constant flux density and elongated extended emission over a length of $l = 6\,\mathrm{mas}$, that is rapidly changing in morphology and position angle, but not in flux density. Assuming a distance of $d = 2.5\,\mathrm{kpc}$, Casares et al. (2005b) determined that the extension ranges between $2\,\mathrm{AU}$ and about $1\,000\,\mathrm{AU}$.

Although, the radio emission shows variability, no bursting activity or periodicity has been detected up to now (Marti et al. 1998; Ribó et al. 1999; Moldon et al. 2009). The observation at $\lambda = 1.4\,\mathrm{GHz}$ showed also no radio pulses (Morris et al. 2002). To explain the non-detection of radio pulses for a possible pulsar, Moldon et al. (2009) suggest that free-free absorption within the stellar wind can smear out the pulsations at the observed frequencies.

The spectrum can be fitted by a power law with a spectral index $\alpha = -0.46 \pm 0.01$ (Marti et al. 1998). This spectral index suggests a non-thermal synchrotron origin of the emission and shows a moderate, but not periodic variability (Combi et al. 2004).

Looking for phase dependence of the radio emission morphology, Moldon et al. (2009) use two VLBA and phased VLA self-calibrated images (Figure 5.2). Both maps show a core component and both a constant flux density within the errors. The elongated emission, however, is once symmetric and at the other time asymmetric and also changes direction at milliarcsecond scales between both runs. The difference in orientation adds up to a change in position angle of $\mathrm{PA} \approx 12^\circ \pm 3^\circ$. These changes in emission morphology let the authors favour the interpretation of LS 5039 as a non-accreting pulsar.

So at the end, there are still two possible interpretations of the radio emission: On the one hand, the interpretation as radio-emitting mildly relativistic jets, $v \approx 0.2\mathrm{c}$, (McSwain & Gies 2002; Paredes et al. 2000, 2002) leads to the generally respected opinion of LS 5039 being a microquasar system. But on the other hand, the radio emission could also arise from a cometary tail structure, and thus LS 5039 would be a pulsar (Mirabel 2007).

For a final clarification of the nature of the radio emission and consequently also the nature of the compact object, precise phase-referenced VLBI observations that cover a whole orbital cycle, are necessary.

IR, optical and UV

The optical part of the spectral energy distribution (SED, see Figure 5.6 at the end of this chapter) is dominated by the bright and hot optical component,

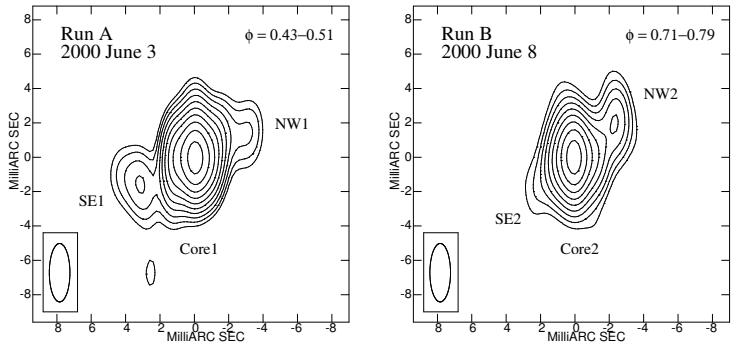

Figure 5.2: Radio images of LS 5039 at $\lambda = 5\,\mathrm{GHz}$. Shown are VLBA and phased VLA self-calibrated images (Moldon et al. 2009).

the star LS 5039. This star is listed in the catalogue of Luminous Stars in the Southern Milky Way (Stephenson & Sanduleak 1971) as OB+R star with $V = 11.4$.

Subsequent optical observations enabled Motch et al. (1997) to correct this value, first, to a brightness of $V \sim 11.2$ and a spectral type of O7V((f)); later the spectral type was determined more precisely to O6.5V((f)) (Clark et al. 2001), where ((f)) indicates strong He II absorption accompanied by weak N III emission lines.

In addition, McSwain et al. (2004) and Casares et al. (2005b) fitted optical and UV spectra (the first and only observations with HST STIS) with calculated line-blanketed model spectra of non-LTE, spherical, and mass-losing model atmospheres,[6] which are optimised for massive OBA stars in consideration of reddening and extinction. From this analysis it was possible, first, to determine values for effective temperature, gravity, and projected rotational velocity, and second, perform a more precise spectral classification of the optical companion star, ON6.5V((f)) (McSwain et al. 2004), and parameters of the system.

The stellar parameter determination reveals an effective temperature of $T_{\mathrm{eff}} = 39\,000 \pm 1\,000\,\mathrm{K}$ and a surface gravity of $\log g = 3.85 \pm 0.10$ (cgs units) for the optical companion and a strong contamination of the photosphere by CNO-burning products. The spectrum of LS 5039 shows strong N and weak C lines

[6]The authors used the atmosphere model code FASTWIND (Santolaya-Rey et al. 1997; Puls et al. 2005).

as compared to stars of similar spectral type. According to empirical studies, particularly stars of this spectral type that are a component of a HMXRB show in general no nitrogen enrichment. This could arise from ejection of mass by the supernova progenitor (McSwain et al. 2004).
These authors also gave a possible explanation for the enrichment of nitrogen in LS 5039. During a time interval at the beginning of the common-envelope phase (see Section 2.4), CNO-enriched gas can be transferred from the progenitor of the compact object to the O star. Under certain circumstances, this can be a relatively stable process, and the massive donor star, which has a radiative envelope, loses mass via Roche-lobe overflow. The transferred material can reach an amount of several solar masses and is enriched in carbon, nitrogen, and oxygen according to the chemical composition of the evolved donor. Other explanations like wind feeding or wind accretion are in principle also possible, but the bulk of transferred material is, in these scenarios, most likely too small to affect the characteristics in the observed spectrum of the O star in LS 5039.

Several photometric campaigns with telescopes in the Canary Islands and at Calar Alto revealed no or only little optical variations appearing on timescales of years. The star is optically very stable within $m \pm 0.01$ mag during different orbital cycles separated by several years (Clark et al. 2001; Martí et al. 2004). In the infrared H and K bands Clark et al. (2001) found significant photometric variability ($m \approx 0.4$ mag), but gave no explanation for the origin of this variability. Martí et al. (2004), in addition, reported on variations in the J band at a later date. The stability gives strong additional evidence that the O star does not fill its Roche lobe and the X-ray binary is powered by wind accretion.
Periodic ellipsoidal variations are a common phenomenon among HMXRBs due to tidal distortions of the optically bright star, provided it reaches a high Roche-lobe filling factor. For LS 5039 neither periodicity nor ellipsoidal modulations have been found up to now (Martí et al. 2004).
While Marti et al. (1998) did not exclude a possible day-to-day variation and Paredes et al. (2002) claimed variations of a few hundredths of a magnitude within one night, Martí et al. (2004) found no reliable evidence of intra-night variability and finally stated that a significant orbital modulation does not exist in the optical light curve of LS 5039. Nevertheless, they considered it possible that short-term fluctuations could be a phase-dependent phenomenon, taking into account the significant eccentricity of the binary system. A possible alternative explanation is that fast variability could be related to accretion and ejection events in this microquasar. An extrapolation of the moderately variable radio spectrum to optical wavelengths shows that variability as expected

from the jets is not likely in the optical range. The constant luminosity of the ON6.5V((f)) star dominates the extrapolated synchrotron emission by four orders of magnitude.

Two additional features occur in LS 5039, which will be explained in the following paragraph. First, the stability of optical flux is in contrast to the occasional variability of LS 5039 when observing the source in optical polarised light (Combi et al. 2004). Second, long-term variations in the X-ray flux appear to be correlated with the variations observed in the Hα equivalent width (Reig et al. 2003). The latter could be interpreted as variations in the mass-loss rate.

Optical polarimetric observations were carried out by Combi et al. (2004). They measured a large amount ($\approx 5\,\%$) of polarised emission in the direction towards LS 5039 and determined the intrinsic polarisation for the object to about $3\,\%$, which is much higher than the expected value from the jet emission in the optical band. They proclaimed that "the intrinsic polarisation in X-ray binary systems can result from non-thermal emission processes due to the presence of high energy electrons in the relativistic jet or, alternatively, by an accretion disc or a stellar envelope. The intrinsic polarisation could change with the binary phase, due to the polarising mechanism, to the distribution and physical state of the material, or by geometric factors such as the inclination angle" (Combi et al. 2004). So they suggested that in this case, the polarised light is generated via electron Thomson scattering in the stellar envelope of the companion star, because, as mentioned above, the non-thermal emission from the jets is not high enough to generate the polarised optical emission, and the luminosity of a possible accretion disc is not very high either. However, based on optical spectropolarimetric observations performed in 2006, Nagae et al. (2009) suggested that the mentioned value of the intrinsic polarisation was overestimated and the observed polarisation was dominated by the typical interstellar polarisation.

Based on the analysis of the Hα line profile, Casares et al. (2005b) determined an upper limit for the mass-loss rate of $\dot{m}_{\rm loss} \lesssim 1.0 \times 10^{-6}\,{\rm M}_\odot\,{\rm yr}^{-1}$. The system was in a high state during the observation and approximately by a factor of four to eight higher than derived by McSwain et al. (2004). But the established values are well comparable to a typical average mass-loss rate of O6.5V stars.

X-ray

The X-ray counterpart of LS 5039, RX J1826.2−1450, was observed in 1990 with ROSAT, included in the ROSAT All-Sky Bright Source Catalogue (1RXS) (see Voges et al. 1999) since 1996, and identified as a HMXRB by Motch et al. (1997), when searching for possible OB/X-ray associations using cross-correlation between the ROSAT catalogue and the SIMBAD OB stars. The source was one of the hardest X-ray sources in the OB/X-ray correlation sample they inspected.

The X-ray source was observed by several X-ray satellites (a summary can be found in Martocchia et al. 2005) and has in general a modest X-ray flux (McSwain & Gies 2002). Regarding all these observations, the flux varies in a range of $F_{\rm X} \sim (5-50) \times 10^{-12}\,{\rm erg\,cm^{-2}\,s^{-1}}$ and thus the luminosity in the range $L_{\rm X} \sim (0.5-5) \times 10^{-34}\,{\rm erg\,s^{-1}}$ (distance estimate: 2.9 kpc, Bosch-Ramon et al. 2005). For instance, during the BeppoSAX observation, a flux of $F_{\rm X}(1-10\,{\rm keV}) = 4.7 \times 10^{-12}\,{\rm erg\,cm^{-2}\,s^{-1}}$ (Reig et al. 2003) was measured. Therefore, the source was supposed to be in a low state, because the flux determination from the former RXTE observations in 1998 resulted in a flux value about one order of magnitude higher. In comparison to classical HMXRBs accreting via Roche-lobe overflow, the luminosity is about a factor of 1000 lower in this observation. Although comparable to the luminosity of Be/X-ray binaries in low state, the luminosity of LS 5039 is at the low end of the distribution of wind accreting massive binaries (Martocchia et al. 2005).

Since a star with spectral type B5 or earlier emits soft X-rays, especially in the energy range $0.2-4.0\,{\rm keV}$, a calculation of the bolometric to X-ray luminosity ratio can reveal information about the fraction of the X-ray emission emitted by the companion star and by the compact object. Normal stars have ratios that are roughly constant and independent of luminosity class and age (Motch et al. 1997). The comparison between bolometric and X-ray luminosity for LS 5039 reveals a high ratio: $L_{\rm X}/L_{\rm bol} = 3.7 \pm 0.9 \times 10^{-5}$. This value is higher than the value expected for a normal O star (Motch et al. 1997). In addition, the optical to X-ray luminosity ratio, $L_{\rm X}/L_{\rm opt} = 6 \times 10^{-5}$, is much lower than typical values of other classical massive XRBs ($L_{\rm X}/L_{\rm opt} = 10^{-1} - 10^{-4}$, McSwain & Gies 2002). Furthermore, the γ-ray luminosity measured for the associated EGRET source is higher than the X-ray luminosity.

The X-ray light curve shows three main features. First, the source is variable in X-rays, second, no X-ray pulsations are detected and, third, there is no evidence of X-ray eclipses. First searches for an orbital period in RXTE

PCA/ASM data were not successful. Actually, an absence of pulses and of periodic emission on timescales between 0.02 and $2\,000\,\mathrm{s}$ was proclaimed (Ribó et al. 1999). More detailed studies of flux changes revealed that the flux is variable at energies higher than $E \approx 3\,\mathrm{keV}$ and fairly constant below that value (Reig et al. 2003). Since the orbital period had been determined by McSwain et al. (2001), the analyses focus on possible phase-dependent effects. Although the RXTE observations did not continuously cover the whole orbit, Bosch-Ramon et al. (2005) established two main variabilities of the flux: the variation with the orbital period[7] of $P_{\mathrm{orb}} = 3.9\,\mathrm{d}$, and miniflares of much shorter duration of about 1 hr. The orbital variation exhibits two maxima: A longer lasting maximum at phase $\phi = 0.8$, which is near the inferior conjunction,[8] and a short maximum at phase $\phi = 0.16$ (Bosch-Ramon et al. 2005). If a Bondi-Hoyle accretion model is assumed, the X-ray variability should feature a sharp increase at periastron passage, which corresponds to the phase interval $\phi \approx 0.9 - 1.1$.

Optical photometry and spectroscopy of the companion star, performed simultaneously to the RXTE observations in July 2003, revealed that the companion star emission was stable, while the X-ray flux showed variability (Bosch-Ramon et al. 2005). These authors discovered on the one side, a correlation between measured $EW(\mathrm{H}\alpha)$ and observed X-ray flux (BeppoSAX observations by Reig et al. 2003), and on the other side they found evidence of an anticorrelation between flux variability and photon index on timescales of days. While the reasons for the observed variability are not completely understood, yet, the variability is clearly related to the orbital motion of the compact object. This is evident, because the eccentric orbit leads to a change in the accretion rate during an orbital cycle. However, if this were the only reason, one would expect the maximum of the X-ray flux right before the periastron passage (Bosch-Ramon et al. 2005). Considering all X-ray flux determinations up to 2003, Reig et al. (2003) suggested that a simple Bondi-Hoyle accretion model is unlikely to explain the flux variability observed. Hence, these authors assumed a decrease in the mass-loss rate from the primary on longer timescales as an alternative or additional factor. Changes in the mass-loss rate would induce changes in the mass accretion rate onto the compact object, and, hence, changes in the observed X-ray flux (Reig et al. 2003; McSwain et al. 2004; Bosch-Ramon et al. 2005).

---

[7] Bosch-Ramon et al. (2005) used the ephemeris determined by Casares et al. (2005b).

[8] Bosch-Ramon et al. (2005) concluded the maximum to be close to the periastron passage, which would be in agreement with an accretion scenario. In fact, the periastron passage is at $\phi = 1.0$, while the inferior conjunction appears at phase $\phi \approx 0.7$.

In addition, the existence of an accretion disc was and still is discussed, because a comparison of observations with simple wind accretion model calculations resulted in a discrepancy of a factor of four in the flux variability (Bosch-Ramon et al. 2005). The short flux variations, miniflares at hour-timescales, are probably related to fluctuations in the stellar wind (Bosch-Ramon et al. 2005). Typical wind accretors show aperiodic fluctuations, which are nothing else than flaring with flux changes of a factor of about five over timescales of a few hundred seconds. But for LS 5039, no such flaring activities were observed (Martocchia et al. 2005).

Anticorrelated to the unabsorbed power-law flux, the photon index varies with the orbit. At the time of highest flux close to phase $\phi = 0.8$, the spectrum exhibits a hardening at phase $\phi = 0.9$ (Bosch-Ramon et al. 2005; Martocchia et al. 2005). This correlation is clear and general, but not too strict. Changes in the hydrogen column density and variations in the diffuse background, are possible explanations for this behaviour. But, when applying a diffuse background model[9] to the spectrum, one needs to exclude both possibilities within the energy range $E = 3 - 30\,\mathrm{keV}$ in order to obtain the anticorrelation. Thus, the changes in flux and photon index may have an intrinsic origin (Bosch-Ramon et al. 2005).

The X-ray spectrum is hard, and no cutoff is present up to $E \approx 30\,\mathrm{keV}$ (Combi et al. 2004; Bosch-Ramon et al. 2005). Above $E \approx 30\,\mathrm{keV}$, the background dominates (Bosch-Ramon et al. 2005). The BeppoSAX data can be fitted in the energy range $E = 0.1 - 10\,\mathrm{keV}$ with an absorbed power-law continuum with a photon-number spectral index of $\Gamma = 1.8 \pm 0.2$ and a hydrogen column density of $N_\mathrm{H} = 1.0^{+0.4}_{-0.3} \times 10^{22}\,\mathrm{cm}^{-2}$ (Reig et al. 2003). The *Chandra* observation yields the hardest photon index, $\Gamma \approx 1.1$, while the *XMM-Newton* observations require a slightly lower photoelectric absorption, $N_\mathrm{H} = 0.70 \pm 0.05 \times 10^{22}\,\mathrm{cm}^{-2}$ (Martocchia et al. 2005). A simple power-law model can fit nearly all observed data sufficiently well (Martocchia et al. 2005), although Bosch-Ramon et al. (2005) fitted the RXTE spectrum with an absorbed power law plus a Gaussian emission line and a disc blackbody component. Martocchia et al. (2005) have found no evidence of edges or fluorescent lines nor evidence of disc emission in the spectrum. The mean hard photon

[9]The diffuse X-ray background is diffuse distributed emission, which contains mainly two components. First, emission which is caused by hot thermal plasma with a temperature of about $10^6\,\mathrm{K}$ and is located in the plane and the halo of the Galaxy. This component primarily emits in the energy range below $0.3\,\mathrm{keV}$. The second component is the sum of all unresolved X-ray sources. These are mainly extragalactic sources like AGNs or quasars (Grupen 2000).

index of about $\Gamma = 1.4 - 1.6$ is similar to the photon index of most XRBs in hard/low state and, in addition, similar to the 'twin' system LS I $+61°303$ while in a stage of radio outburst.

Even though only the fits to the RXTE spectra from 1998 (Bosch-Ramon et al. 2005) were improved when adding a Gaussian to the absorbed power-law model, the different studies of the iron line in LS 5039 are worth mentioning, because an iron line detection would provide knowledge on the accretion flow and the jet.[10] The line is present at $E = 6.7 \pm 0.1\,\mathrm{keV}$ in the RXTE observation, but was already suggested by Ribó et al. (1999) to be probably a diffuse background feature coming from the Galactic ridge emission. This interpretation was confirmed e. g. by Martocchia et al. (2005) and Takahashi et al. (2009), who found no evidence of iron line emission.

Information from the hard X-ray energy range in comparison to the behaviour in the soft X-ray and the VHE γ-ray regime are crucial to clarify the nature of the source and the energy of the accelerated particles. Also, only the modelling of the broad band spectrum can answer open questions and reveal the yet unknown physical properties of the source, i. e. the magnetic field in the jets or the dominating emission processes (synchrotron or inverse Compton).

LS 5039, though, is faint in the hard X-ray domain and is located in a crowded field. Observations with BATSE (Earth occultation data) show only a slight excess in the range from $20 - 400\,\mathrm{keV}$: $F\,(20 - 40\,\mathrm{keV}) = 2.4 \pm 0.5 \times 10^{-11}\,\mathrm{erg\,cm^{-2}\,s^{-1}}$, $F\,(40 - 70\,\mathrm{keV}) = 2.9 \pm 0.4 \times 10^{-11}\,\mathrm{erg\,cm^{-2}\,s^{-1}}$, $F\,(70 - 160\,\mathrm{keV}) = 2.0 \pm 0.6 \times 10^{-11}\,\mathrm{erg\,cm^{-2}\,s^{-1}}$, and $F\,(160 - 430\,\mathrm{keV}) = 3.7 \pm 1.2 \times 10^{-11}\,\mathrm{erg\,cm^{-2}\,s^{-1}}$ (Harmon et al. 2004). A first detection with *INTEGRAL* was proposed by Goldoni et al. (2007), and subsequently the source had been listed in the Third IBIS/ISGRI Soft Gamma-Ray Survey Catalog (Bird et al. 2007). The first mentioned authors revealed a flux of $F = 5.9 \pm 1.6 \times 10^{-12}\,\mathrm{erg\,cm^{-2}\,s^{-1}}$ in the energy range $E = 20 - 40\,\mathrm{keV}$ and an upper flux limit of $F < 9.5 \times 10^{-12}\,\mathrm{erg\,cm^{-2}\,s^{-1}}$ within $E = 40 - 100\,\mathrm{keV}$ in a $300\,\mathrm{ks}$ observation. This value is lower than the one determined from the BATSE observations, but it is consistent with an extrapolation of the results of the RXTE data analysis.

[10] The Kα fluorescent line of iron is a narrow line and appears in rest frame at an energy of $6.40 - 6.97\,\mathrm{keV}$ depending on the ionisation state. It is a powerful tool for exploration of the accretion mechanism, because it originates in rotating material in the accretion disc. Therefore, the line shape can be broadened and gives some information on the accretion geometry and the spin of the compact object (Fritz 2008).

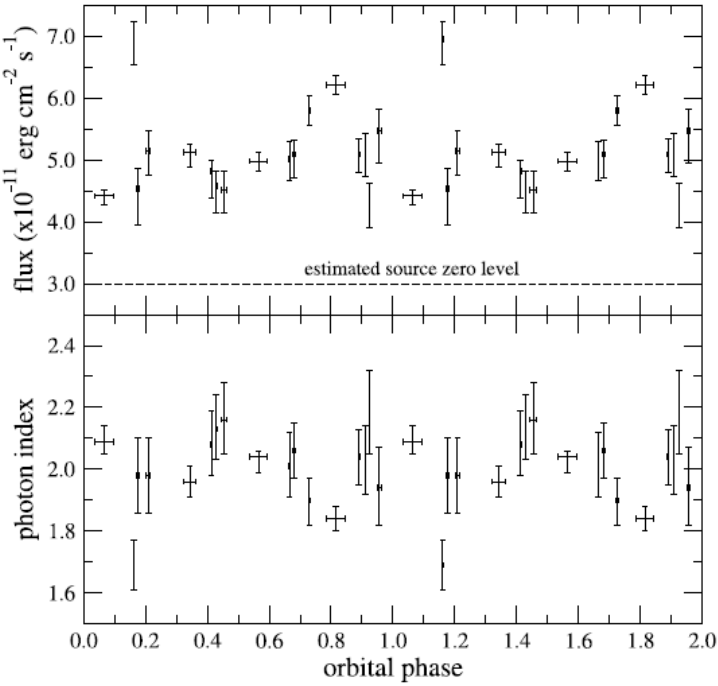

Figure 5.3: Phase dependence of the unabsorbed power-law fluxes and the photon index in the energy range $E = 3 - 30\,\mathrm{keV}$. From Bosch-Ramon et al. (2005).

γ-ray

The X-ray spectrum of LS 5039 gives no hint of a cutoff at energies above $E = 100 - 200\,\mathrm{keV}$. A cutoff would be a typical sign of emission produced via thermal Comptonisation, for example in a corona (Bosch-Ramon et al. 2005). The absence of the cutoff is confirmed by observations with instruments working in the hard X/soft γ-ray regime like *INTEGRAL* (see Chapter 6) and the instruments on board the Compton Gamma Ray Observatory (CGRO): the Burst and Transient Source Experiment[11] (BATSE), the Imaging

[11] For information on the BASTE catalogue see Harmon et al. (2004).

Compton Telescope[12] (COMPTEL), and the Energetic Gamma Ray Experiment Telescope[13] (EGRET).

Paredes et al. (2000) were the first, who suggested that LS 5039 was also a γ-ray source. Among the most significant and strongest sources detected with COMPTEL, the extended so-called 'COMPTEL l=18 source' (also named GRO J1823−12) remained unidentified, but it was suggested it is a superposition of unresolved point sources (Strong et al. 2001). The COMPTEL source can be disentangled into three known γ-ray EGRET sources, one of them 3EG 1823−1514 was associated with LS 5039 (Paredes et al. 2000, 2002). The MeV spectrum of this source is hard with a photon index of $\Gamma \approx 2$. No significant time variability is detected (Collmar 2004). This association is important, because it reinforces the idea that microquasars are in principle able to emit radiation in the MeV −GeV energy range and, in particular, that multi-GeV particles are present in the source LS 5039.

Recent observations with the Large Area Telescope (LAT) on board the Fermi-GLAST satellite confirmed the detection of HMXRBs in the MeV −GeV range. Abdo et al. (2009b) were able to proclaim the first orbital variability found for a GeV source, LS I $+61°303$. The analysis for the LS 5039 observation is in progress, but the source has already been listed in the Fermi-GLAST satellite Bright Gamma-Ray Source List (Abdo et al. 2009a) with a $2\,\sigma$ upper limit of $F(100\,\mathrm{MeV} - 1\,\mathrm{GeV}) = 67.6 \times 10^{-8}\,\mathrm{cm^{-2}s^{-1}}$ in the lower energy band and a flux of $F(1\,\mathrm{GeV} - 100\,\mathrm{GeV}) = 2.47 \pm 0.27 \times 10^{-8}\,\mathrm{cm^{-2}s^{-1}}$ in the higher energy band.

VHE γ-ray

The interest in LS 5039 grew when Aharonian et al. (2005b) observed the source in very high energetic γ-rays with *H.E.S.S.* The observation shows a point-like emission at position α(J2000)=18h 26m 15s and $\delta = -14°\,49'\,30''$ (with a statistical uncertainty of ± 32 arcsec and a systematic uncertainty of ± 30 arcsec in the position)[14] with an upper limit for the extent of 50 arcsec ($1\,\sigma$). This position is consistent with the position of the observation with

[12] See Schönfelder et al. (2000) for information on the COMPTEL catalogue. The observation of LS 5039 can be found in Strong et al. (2001).

[13] Further information on the EGRET catalogue including 3EG 1823−1514 see Hartman et al. (1999).

[14] The position in galactic coordinates is $l = 16.879°$, $b = -1.285°$ with statistical and systematic uncertainties of ± 12 arcsec and ± 20 arcsec, respectively.

VLBA (Figure 5.4) within $1\,\sigma$ statistical uncertainty. A search for possible counterparts in the radio and X-ray energy range provided that only the high-mass X-ray binary LS 5039 may be associated with the VHE γ-ray source (also called HESS J1826-148, Aharonian et al. 2005b). Nevertheless, Martocchia et al. (2005) noted on the basis of the asynchronicity of the observations that it would be, in principle, possible that the VHE γ-ray is a long episode flaring blazar.

The average integrated flux for energies above $250\,\mathrm{GeV}$ is $F\,(>250\,\mathrm{GeV}) = 5.1(\pm 0.8_{\mathrm{stat}} \pm 1.3_{\mathrm{syst}}) \times 10^{-12}\,\mathrm{photons\,cm^{-2}\,s^{-1}}$ and is detectable up to energies of $E \approx 4\,\mathrm{TeV}$. The statistics of the observation prove the reliability of the detection. A total of 1960 observed γ-ray events match a significance of $+40\sigma$ above background.

The timing analysis of the observations shows that the VHE γ-ray flux is quite stable at $E \approx 0.2\,\mathrm{TeV}$, but has a modulation at higher energies, which is strongest at a few TeV. This modulation is clearly correlated with the orbital phase and varies in the range of $L = (4-10) \times 10^{33}\,\mathrm{erg\,s^{-1}}$.[15] A Lomb-Scargle periodogram and normalised Rayleigh statistics reveal the highest peak at $P_{\mathrm{orb}} = 3.9078 \pm 0.0015\,\mathrm{d}$,[16] which is consistent with the orbital period obtained from optical observations.

Based on the timing behaviour, an analysis of phase-resolved energy spectra showed that the VHE γ-ray emission is essentially confined to a half of the orbit. In the energy range between $0.2\,\mathrm{TeV}$ and a few TeV, the flux peaks and the energy spectrum hardens around the inferior conjunction epoch of the compact object. Aharonian et al. (2006c) fitted the average VHE spectrum in the range from 0.2 to 10.0 TeV with a power law ($\mathrm{d}N/\mathrm{d}E \sim E^{-\Gamma}$) and determined a photon power-law index of $\Gamma = 2.23$. Exploring the integral fluxes at energies $E > 1\,\mathrm{TeV}$ versus the orbital phase ϕ revealed that the flux reaches the maximum around the inferior conjunction ($\phi = 0.716$). The flux minimum appear at phase $\phi \approx 0.2$, which is just after the superior conjunction ($\phi = 0.058$). Therefore, Aharonian et al. (2006c) split the observations into two parts: the epoch around the inferior conjunction (INFC, $0.45 < \phi \leq 0.9$) and the epoch around the superior conjunction (SUPC, $0.9 < \phi \leq 1.45$). The observed spectra are shown in Figure 5.5.

[15] Assuming a distance of 2.5 kpc and integrated over the energy range from 0.2 to 10 TeV.
[16] The statistic for this period is good. The post-trial chance probability is $P < 10^{-5}$.

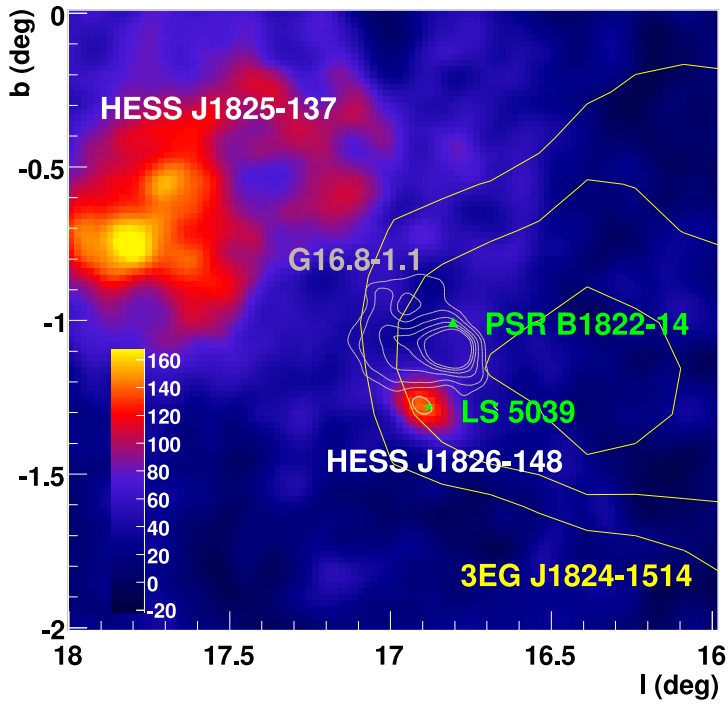

Figure 5.4: HESS J1826−148, associated with LS 5039, observed in VHE γ-rays by *H.E.S.S.* The map shows the excess in units of counts and has been smoothed by the point spread function. The grey contours represent the radio emission observed within the Parkes-MIT-NRAO 6cm radio survey, which originated from the supernova remnant G16.8−1.1 (gray). The yellow contours give the confidence levels of the EGRET source 3EG J1824−1514. Green marks are the positions of radio sources: the pulsar PSR B1822−14 and the source associated with LS 5039. Figure from Aharonian et al. (2005b).

The photon index apparently varies within the orbital cycle. During the SUPC phase interval, the differential photon energy spectrum can be fitted with a relatively steep pure power law with photon index $\Gamma = 2.53 \pm 0.07_{\rm stat} \pm 0.1_{\rm syst}$. In contrast, the fit for the INFC interval of the energy spectrum is a hard power law with $\Gamma = 1.85 \pm 0.06_{\rm stat} \pm 0.1_{\rm syst}$ and an exponential cut-off at $E_0 = 8.7 \pm 2.0\,\mathrm{TeV}$ (Aharonian et al. 2006c). A harder spectral shape

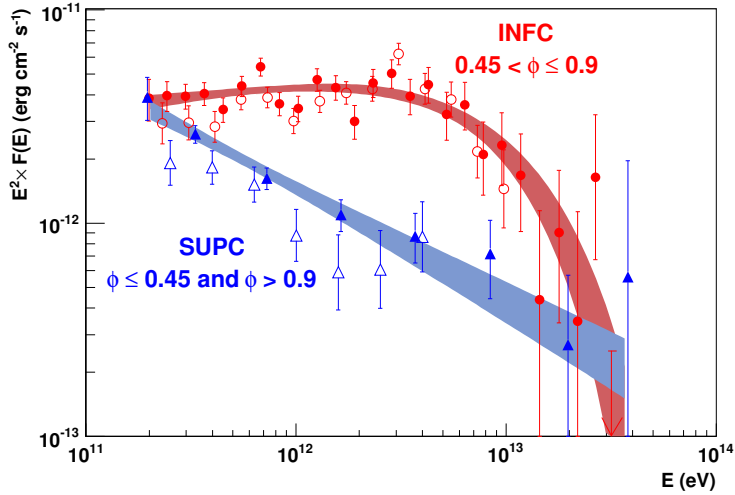

Figure 5.5: The spectrum of LS 5039 in VHE γ-rays for two different phase intervals. Red circles show the spectrum in the phase interval around inferior conjunction (INFC, $0.45 < \phi \leq 0.9$) and blue triangles show the spectrum in the phase interval around superior conjunction (SUPC, $0.9 < \phi \leq 1.45$). The shaded regions are $1\,\sigma$ confidence bands on the fitted functions. Figure from Aharonian et al. (2006c).

coincides with an enhanced flux. This is even more interesting, since a corresponding spectral hardening with increasing flux is also observed at X-ray energies between $E = 3\,\mathrm{keV}$ and $30\,\mathrm{keV}$ (Bosch-Ramon et al. 2005). If the soft γ-ray regime ($E = 25 - 200\,\mathrm{keV}$) is considered in addition, it is remarkable that all observations from X-rays up to TeV γ-rays show a higher flux at $\phi \approx 0.8$ in the phase-resolved light curves (see Section 6.2).

Yet, the detailed production mechanism of VHE γ-rays in LS 5039 is still under discussion (see Section 7.3), but one basic idea is that optical photons from the stellar companion can be boosted to γ-ray energies by inverse Compton scattering on VHE electrons (Bosch-Ramon & Paredes 2004). In particular the origin of the orbital modulation of the VHE γ-ray emission is unclear. Absorption and changes in the production processes may play an important role (Aharonian et al. 2005b).

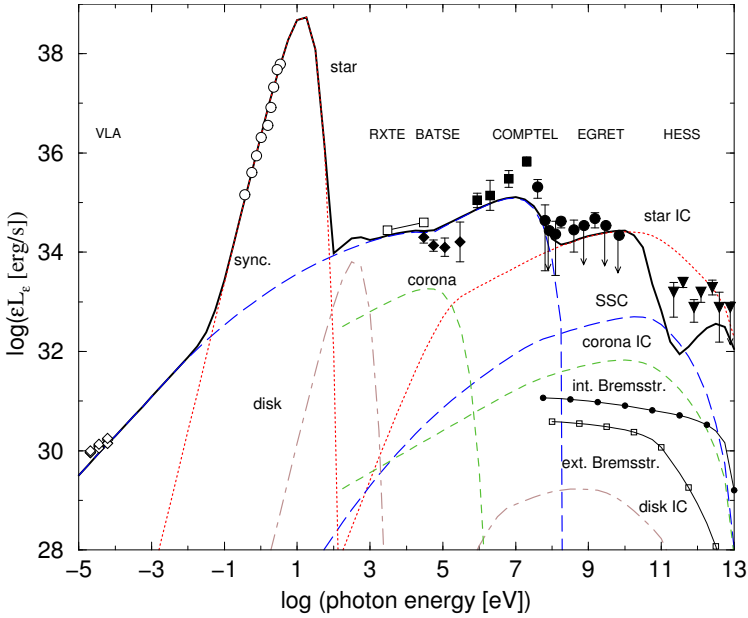

Figure 5.6: Broad-band spectral energy distribution for LS 5039. Shown are observations up to the year 2006 and in addition the most important radiation components contributing to the total emission (*black line*). The spatial resolution of COMPTEL did not allow resolution of the three EGRET sources at the position of GRO J1823−12. So their superposition is in fact shown in the SED. Figure from Paredes et al. (2006). References for the data points can be found therein.

CHAPTER 6

INTEGRAL Observations of LS 5039

To study the hard X-ray emission of LS 5039, we use data from the satellite *INTEGRAL* from the beginning of scientific operation in 2003 until October 2007. A general overview of the satellite is presented in Section 4.3. Searching the data archive available at the *INTEGRAL* Scientific Data Centre (ISDC),[1] including public data as well as data from the Key Programme, results in a total of 1648 science windows (ScWs) in the region that includes LS 5039. These ScWs were preselected by choosing an off-axis angle of the source smaller than 10 degrees and by choosing only pointing observations that had a nominal observation time of more than 1000 seconds. In the end, 1627 ScWs are successfully processed through the analysis with Off-line Scientific Analysis (OSA) version 7.0 up to the image step IMA.

6.1 Data selection

Especially for faint sources in crowded fields as it is for LS 5039, *INTEGRAL* data suffer from the statistical effects of a coded mask instrument. A further selection of "good science windows" was necessary to reduce these statistical effects, so only those ScWs that fulfil the following criteria were included in the analysis :

1. The effective exposure time after extraction is larger than $1000\,\mathrm{s}$.
2. The number of good time intervals (GTI) does not exceed 10.

[1] The *INTEGRAL* Scientific Data Centre (ISDC) and the data archive is available at `http://isdc.unige.ch/`

Table 6.1: Summary of selected and analysed *INTEGRAL* data for LS 5039. The data for the analysis are taken from 69 revolutions, i. e. from revolution 0050 (03-11-2003) to revolution 0614 (10-25-2007).

Number of all extracted ScWs	1648
Number of ScWs after selection	1393
Number of ScWs in phase SUPC	721
Number of ScWs in phase INFC	672
final total analysed exposure time	$\approx$ 2.99 Ms
split in the SUPC phase	$\approx$ 1.56 Ms
and in the INFC phase	$\approx$ 1.43 Ms

3. The mean background intensity level of a single ScW in the energy range $25-60$ keV falls within $3\,\sigma$ of the distribution of the mean background intensity levels of all other ScWs in the same energy band.

The resulting 1393 science windows cover the time range from 03-11-2003 (ScW: 005000080010) to 10-25-2007 (ScW: 061400950010). In Table 6.1, the number of observational data of the source LS 5039 taken by the *INTEGRAL* satellite are listed. In addition, the selection and partitioning made for this analysis is described (see Section 6.2). We focus our analysis on the data of the *Integral Soft Gamma-Ray Imager* (*IBIS*/*ISGRI*), because only in less than 10 % of the selected ScWs, is LS 5039 in the fully coded field of view of JEM-X. Concerning, in addition, the sensitivity of JEM-X[2] and the amount of available data, a JEM-X analysis for this source shapes up as being not suitable.

6.2 Analysis

The special circumstances of the *INTEGRAL* observations of this source – a faint source in combination with a crowded field and a coded mask instrument – require a very careful analysis. So, we use the OSA version 7.0 provided by the ISDC to analyse the ISGRI data, but cross-check the results and also generate the light curve for the timing analysis with the analysis package developed by

[2]The User Manual to the OSA can be found at:
`http://isdc.unige.ch/?Support+documents`
See page 15 of the JEM-X Analysis User Manual for a JEM-X sensitivity plot.

the INAF-IFC Palermo[3] (Segreto & Ferrigno 2006), in addition. According to the authors of this software, it is suitable to produce reliable results even in the case of the presence of a larger number of sources in the FoV.

In addition a special handling of the OSA is used for this analysis. First, we use a user catalogue which includes 115 sources, i. e. all sources listed in the *INTEGRAL* General Reference Catalog[4] which are in the field of view (FoV) and which turned out to be as bright as or brighter than RX J1826.2−1450 (≡ LS 5039). This is required, because the source of interest is quite faint and the crowded field produces too many ghost images if the known sources are not subtracted. Second, the spectrum is produced with the help of the OSA tool MOSAIC_SPEC[5] from 13 mosaics, each covering one energy bin in the $13 - 250\,\mathrm{keV}$ range. The binning chosen is identical to the default energy binning the OSA uses for the spectrum calculation step (SPE). This procedure is needed, due to the fact that the source is faint and the FoV is too crowded, and provides more reliable results than the standard OSA pipeline does. Section 4.3.2 gives further reasons for this approach.

We also check our results using the standard SPE and the light curve creation (LCR) steps of the OSA. In this case, we use a special catalogue including all sources with a detection significance greater than $6\,\sigma$ in the energy band $20 - 60\,\mathrm{keV}$. The catalogue includes 65 sources. According to the User Manual of the *INTEGRAL IBIS/ISGRI* data analysis, this is beyond the standard method (see the *IBIS* Analysis Manual[1] for details). However, our results show that a careful treatment of this standard method provides a comparable result, in spite of the restrictions (see Figure 6.3).

To estimate new findings and to compare them with results in other wavelength ranges, the data sample is split, first, into two orbital phase intervals for imaging analysis, and, second, into 10 smaller orbital phase intervals to analyse the flux dependence on orbital phase.

Imaging

All ScWs fulfilling the selection criteria are added up to one mosaic. The

[3]The *INTEGRAL* software developed at INAF-IFC Palermo is available at `http://www.pa.iasf.cnr.it/~ferrigno/INTEGRALsoftware.html`

[4]The *INTEGRAL* General Reference Catalogue is available at ISDC: `http://isdc.unige.ch/index.cgi?Data+catalogs`

[5]The tool MOSAIC_SPEC is provided by the ISDC at `http://isdc.unige.ch/Soft/download/osa/osa_doc/osa_doc-5.0/osa_um_ibis-5.0/node108.html#mosaspec`

FITS-file which the OSA produces contain, apart from an intensity and an exposure map, a significance map. When analysing the source position of LS 5039, the source is clearly seen at a significance level of $7.7\,\sigma$ in the lower energy band of $25 - 60\,\mathrm{keV}$. To compare the hard X-ray observation with the emission in γ-rays observed with *H.E.S.S.* (see Section 5.2, paragraph on VHE γ-rays), we divide the data set into two phase intervals, which are defined in Aharonian et al. (2006c) for the *H.E.S.S.* data: the superior conjunction passage at the orbital phase $0.9 < \phi \leq 1.45$ (SUPC), and the inferior conjunction at the orbital phase $0.45 < \phi \leq 0.9$ (INFC). Figures 5.1 and 6.3 clarify the choice of the intervals. The two significance maps in the energy range $25 - 60\,\mathrm{keV}$ are shown in Figure 6.1. The open boxes display source positions. These positions are provided by the latest *INTEGRAL* General Reference Catalog.[4] For the total sample and the total energy band $25 - 200\,\mathrm{keV}$, the source is detected at the position fitted by the OSA ($\mathrm{RA} = 276.517\,\mathrm{deg}$, $\mathrm{DEC} = -14.812\,\mathrm{deg}$) with $7.4\,\sigma$. Within the errors, this is consistent with the source position determined by Bird et al. (2007). Looking at the significances in the orbital resolved intervals, one can clearly see that the flux of the source varies with the orbital phase. The exposure times, approximately $1.43\,\mathrm{Ms}$ for the INFC phase interval and $1.56\,\mathrm{Ms}$ for the SUPC phase interval, are almost the same. During the INFC phase interval, the source is detected by the OSA with a significance of $\approx 7.8\,\sigma$ (Figure 6.1, *lower* panel), while during the SUPC phase interval no source is identified by the standard OSA procedure. When analysing the source position with the help of the additional tool MOSAIC_SPEC, an excess at the level of $2.8\,\sigma$ can be detected at the source position (Figure 6.1, *upper* panel).

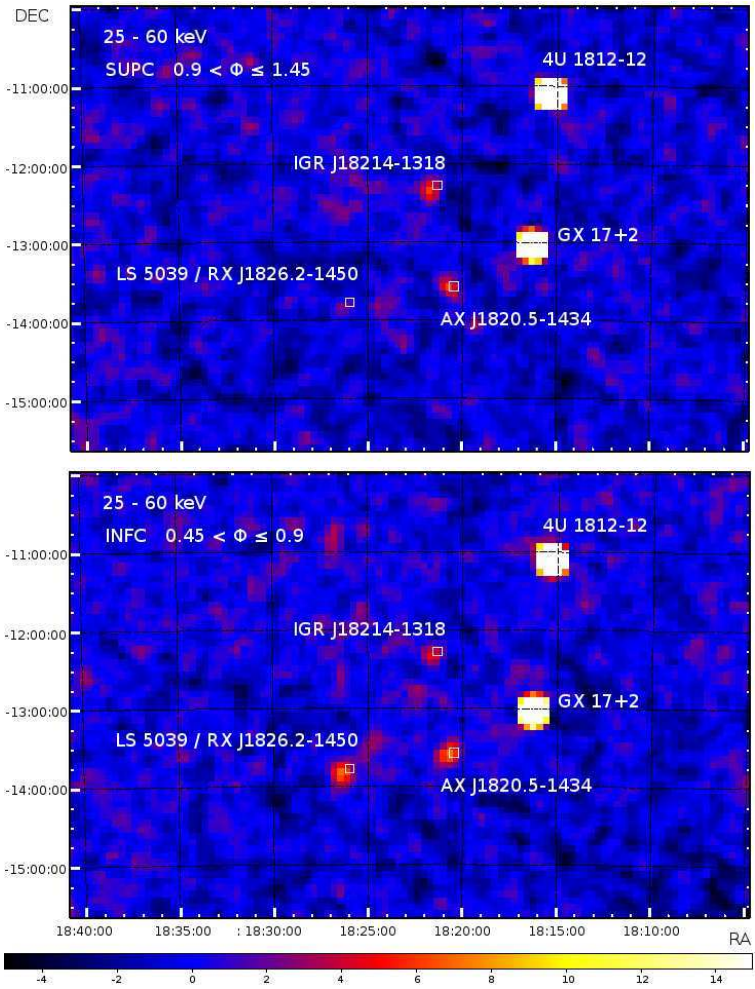

Figure 6.1: *INTEGRAL* mosaics of LS 5039 observations. Both panels show significance maps in the energy range $25 - 60\,\mathrm{keV}$. The open boxes are known source positions. For the SUPC phase interval (*upper* panel), the source appears in a very faint state. Comparable exposure times and a higher significance for LS 5039 in the INFC phase interval (*lower* panel) indicate variability of the hard X-ray emission with orbital phase (Figure 6.3). The inferior conjunction is the phase which corresponds to the maximum flux of the source.

Timing analysis

As described in Section 4.3.2, a light curve for LS 5039 provided by the standard OSA could be difficult to rely on. For this reason, we also produced a light curve with the INAF-IFC data analysis software (Segreto & Ferrigno 2006). This light curve is used to search for periodicity. Unfortunately, low statistics and large gaps in the sample of observations yield a search failure for an unambiguous period. Nevertheless, epoch folding produces a periodogram (see Figure 6.2), which shows a peak at a period of $P_{\rm orb} = 3.903\,\mathrm{d}$. Within the uncertainties, this is in good agreement with the orbital period in the optical band. To explore the behaviour of the hard X-ray flux related to the orbital phase, we produce a ten bin orbital phase profile. The light curve is, therefore, folded using the known orbital period of $P_{\rm orb} = 3.90603\,\mathrm{d}$ with HJD $(T_0) = 2\,451\,943\overset{\mathrm{d}}{.}09 \pm 0\overset{\mathrm{d}}{.}10$ ($\equiv$ phase $\phi = 0.0$ and periastron passage) determined by Casares et al. (2005b). To exclude again the dependence on the many sources in the crowded FoV, ten mosaics corresponding to each of the ten orbital phase intervals are produced, in addition. Subsequently, the count rates at the source positions given by the catalogue are determined. A 2D-Gaussian fit with fixed width (HWHM $= 6.0$ arcmin) and fixed source position provides the flux values. Both methods yield (within errors) comparable results: The hard X-ray emission is clearly modulated with the orbital phase and appears to be in phase with the TeV emission (Figure 6.3). The *H.E.S.S.* data points in the figure are from Aharonian et al. (2006c).

Spectral analysis

For the orbital phase interval corresponding to the INFC it is possible to generate a statistically significant *IBIS/ISGRI* spectrum of LS 5039. This spectrum is shown in Figure 6.4. The data are fitted using XSPEC version 11.3 (Arnaud 1996) with a pure power-law model with a photon index of $\Gamma = 2.0^{+0.2}_{-0.2}$ (90% confidence level). The quality of the fit is given by a reduced $\chi^2 = 1.4$ (9 degrees of freedom).

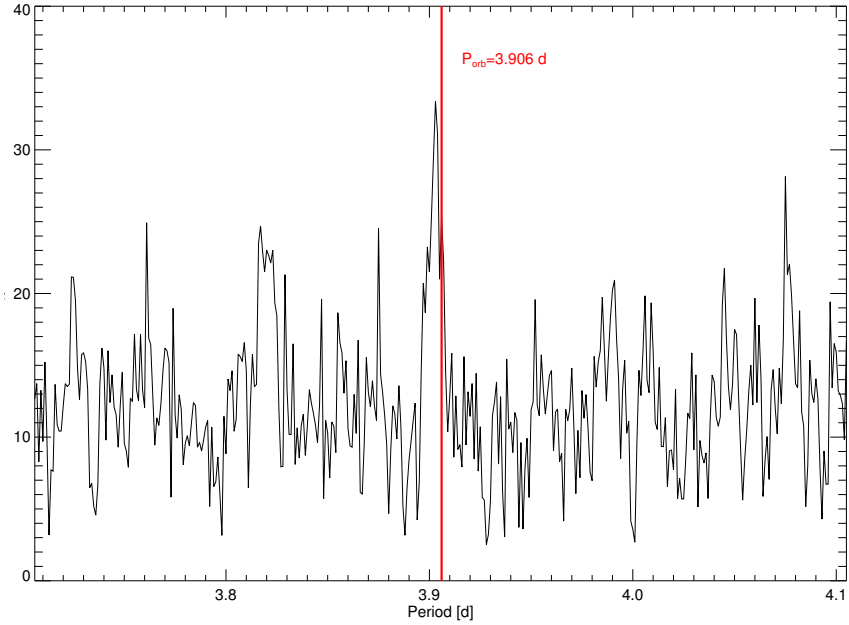

Figure 6.2: An epoch folding on the *INTEGRAL* light curve shows a peak at a period which is nearly identical to the orbital period determined from optical observation of the system (red line, Casares et al. 2005b). All other peaks are likely beat frequencies due to the large gaps in the sample of observations.

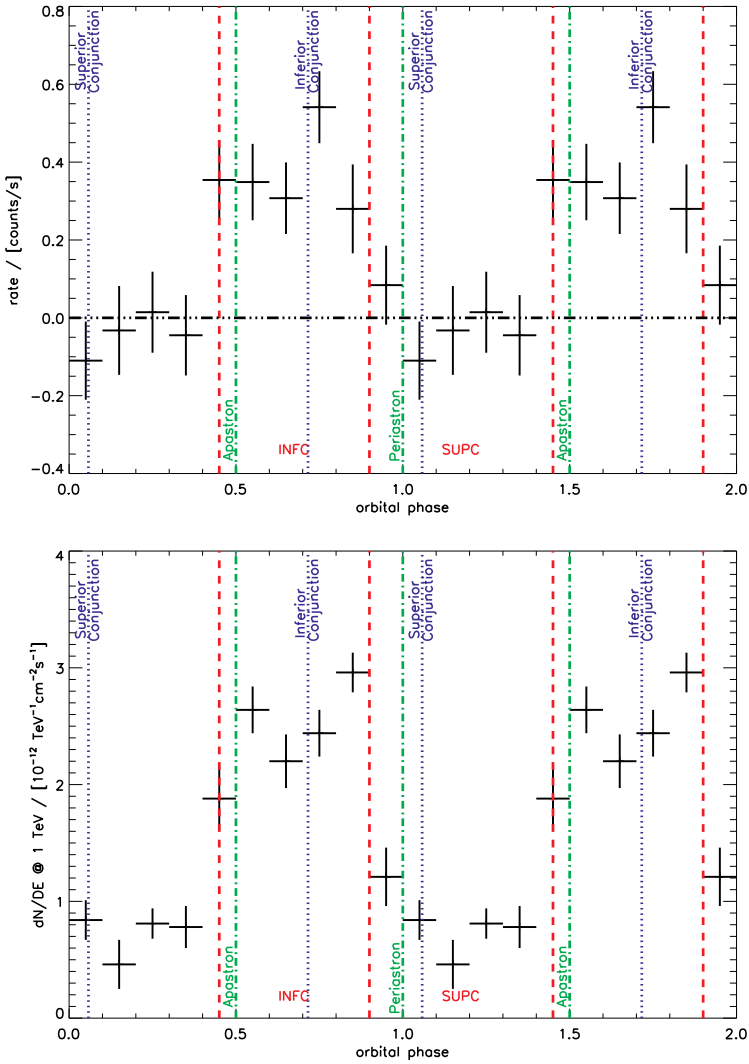

Figure 6.3: *T*op: Orbital profile for LS 5039 in the energy range $25-200$ keV observed by *INTEGRAL*. The light curve is folded with the orbital period of $P_{\rm orb} = 3.90603$ d. *B*ottom: Orbital profile for LS 5039 for the energy range above 1 TeV observed by *H.E.S.S.* (Aharonian et al. 2006c). The hard X-ray emission is in phase with the TeV γ-rays.

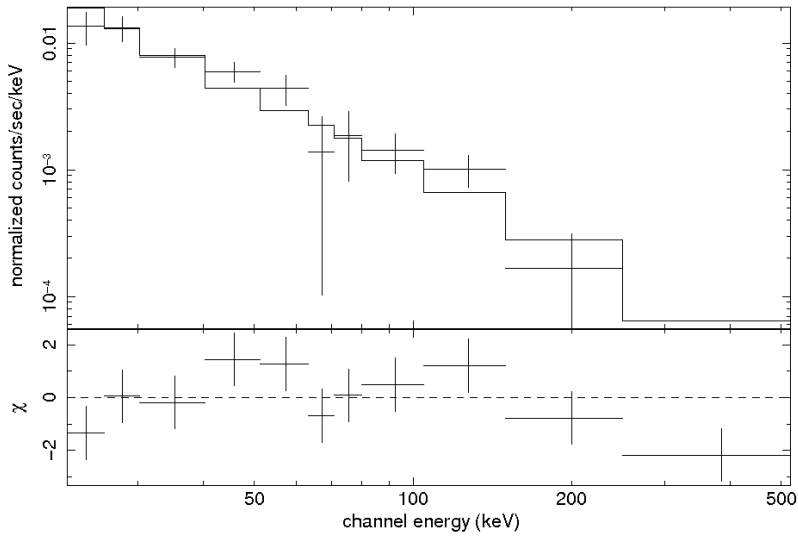

Figure 6.4: Spectrum and power-law model for LS 5039 at the inferior conjunction. The fitted model is a pure power law with a spectral index of $\Gamma = 2.0 \pm 0.2$.

CHAPTER 7

Results and Interpretation

7.1 Results of the analysis of the *INTEGRAL* observation of LS 5039

The faintness of the source and the very crowded sky region – near to the Galactic centre – required a very careful, non-standard handling of the *INTEGRAL* data. Moreover, the analysis described in Chapter 6 was cross-checked with INAF-IFC Palermo Software which provided consistent results. For that reason, reliable results were obtained with standard OSA tools. These results show that LS 5039 emits in the hard X-ray energy range. For two phase dependent epochs a flux rate and a flux upper limit respectively, are determined: for the INFC phase interval a flux rate of $(3.54 \pm 2.30) \times 10^{-11}$ erg cm^{-2} s^{-1} (90 % conf. level) is measured and for the SUPC phase interval the flux upper limit is 1.45×10^{-12} erg cm^{-2} s^{-1} (90 % conf. level). Both values are estimated from mean count rates in the energy range $25 - 200$ keV for a total exposure time of about 3 Ms. In addition, a spectrum for the inferior conjunction phase is obtained and found to be well described by a power law with a photon index of $\Gamma = 2.0 \pm 0.2$. At the superior conjunction the hard X-ray emission, if any, is below the sensitivity of *INTEGRAL*. The second main result of the *INTEGRAL* analysis is that the hard X-ray emission is modulated with the orbital phase and this modulation is found to be in phase with the TeV emission.

7.2 Results of the analysis of *Suzaku* observations

After our findings were published, an analysis of the *Suzaku* observation of LS 5039 was performed and the results were published. These observations

were performed with the X-ray Imaging Spectrometer (XIS) and the Hard X-ray Detector (HXD) instruments. The *Suzaku* observation covers about one and a half orbital cycles of LS 5039 continuously and enables Takahashi et al. (2009) to reveal new findings.

These authors detected X-ray emission in the range from $E \sim 1\,\mathrm{keV}$ up to $70\,\mathrm{keV}$. The emission shows modulation by a factor of two of the count rate, correlated with the orbital phase, in the energy ranges $E = 1 - 20\,\mathrm{keV}$ and $E = 15 - 40\,\mathrm{keV}$. The main features are a minimum at phase $\phi = 0.0 - 0.3$ and a maximum at phase $\phi = 0.5 - 0.8$. In addition, the *Suzaku* light curve shows some short time variability, i. e. two peaks with very short duration at phase $\phi = 0.48$ and $\phi = 0.7$. The total observation time of one and a half orbital cycles leads to an overlap of observed data of the same orbital phase. Hence, it is possible to study these short time fluctuations in two different cycles.

This comparison shows that a short dip only appears in the second observed cycle at phase $\phi = 0.35$ (according to that, this is phase $\phi = 1.35$ in Figure 7.1), and, therefore, these short timescale fluctuations are thought to be caused by a changing environment of the X-ray emitting region, which is not a periodic and orbital dependent phenomenon. The determined flux varies between $F\,(1 - 10\,\mathrm{keV}) = 5.18 \pm 0.03 \times 10^{-12}\,\mathrm{erg\,cm^{-2}\,s^{-1}}$ and $F\,(1 - 10\,\mathrm{keV}) = 12.05 \pm 0.02 \times 10^{-12}\,\mathrm{erg\,cm^{-2}\,s^{-1}}$.

The observed spectrum shows no cutoff up to the energy $E \approx 70\,\mathrm{keV}$ and no phase dependent spectral variation. The spectrum can be fitted by a hard power law with photoelectric absorption. The derived photon indices vary between values of $\Gamma = 1.61$ around phase $\phi = 0.95 - 1.15$ (close to SUPC) and $\Gamma = 1.45$ around phase $\phi = 0.45 - 0.65$ (near apastron). A search for emission lines in the spectrum reveals no evidence for significant lines.

The *Suzaku* results are in agreement with the *INTEGRAL* results presented in Section 7.1 and Chapter 6.

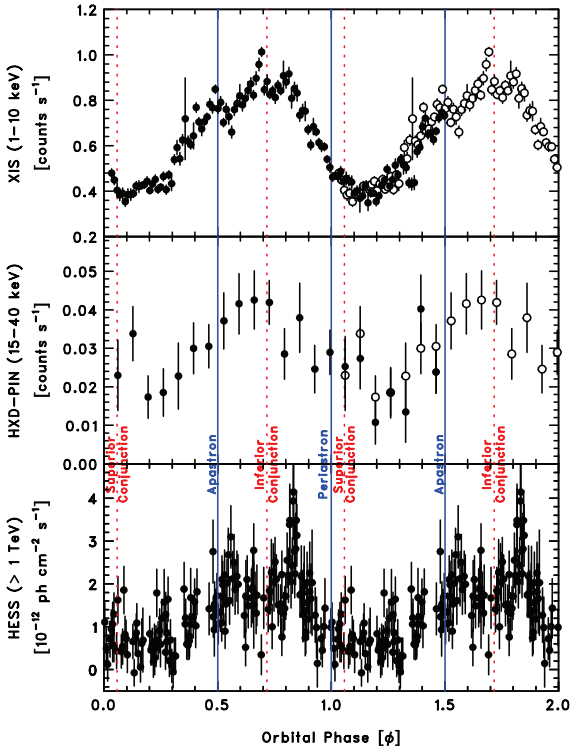

Figure 7.1: Orbital profiles observed by the instruments on board the *Suzaku* satellite compared to the TeV light curve obtained by *H.E.S.S.*. To make the orbital dependence more clearly visible, two orbital cycles are plotted. The filled circles in the two *Suzaku* data samples are the data points of the 200 ks observation during one and a half orbital cycles, whereas the open circles are the same data points but shifted by one orbital period. Two different instruments were used. In the *top* panel data observed by the X-ray Imaging Spectrometer (XIS) in the energy range $1 - 10$ keV are shown and the data observed by the hard X-ray detector (PIN/HXD) in the energy range $15 - 40$ keV are plotted in the *middle* panel. In the *bottom* panel the TeV light curve observed by Aharonian et al. (2006c) at energies larger than 1 TeV is given. The *H.E.S.S.* data are the same (but unbinned) as the data plotted in Figure 6.3. Figure from Takahashi et al. (2009).

7.3 Interpretation

The current most pressing and still open questions on LS 5039 can be summarised as follows:

- How are TeV γ-rays produced in this source?
- Why are they modulated with the orbital phase?
- Why are X-ray and VHE γ-ray emission in phase with each other?
- What is the nature of the compact object?
- What kind of system is LS 5039? Is LS 5039 a microquasar system or a system containing a young non-accreting pulsar?

In the next sections, these questions are looked at closely and different observable features are discussed. But to answer, and even to discuss these questions, we should first introduce the two major models discussed in the literature: the microquasar scenario and the non-accreting pulsar model. Differences are features like accretion and jets in the microquasar model, and, in contrast, a shock front and pulsations in the non-accreting pulsar model.

7.3.1 Accretion mechanism in LS 5039

The underlying accretion mechanism occurring in the LS 5039 binary system, if any, is not yet understood. The geometry of the system (duration of orbital cycle, masses of the components, and separation between them) and the behaviour of HMXRBs in general, suggest that LS 5039 is a wind accreting system (Bosch-Ramon et al. 2005). Actually, the properties of the orbit, the observation of the optical light curve, which shows no periodic ellipsoidal variations (Martí et al. 2004), and the low X-ray luminosity (McSwain et al. 2004), allow Martocchia et al. (2005) to exclude a Roche-lobe overflow. But, whether the radiation driven wind is directly accreted or if the accreted matter is transferred through an accretion disc onto the compact object is unclear (Martocchia et al. 2005).

Accretion rate

The connection between the mass-loss rate[1] of the primary and the mass accretion rate onto the compact object was confirmed by Reig et al. (2003) and Martocchia et al. (2005). They revealed the correlation between optical emission of the Hα line and X-ray flux intensity. However, the latter authors noted that the variability due to orbital motion cannot be clearly distinguished from possibly long-term wind variability. Furthermore, the accretion rate will vary with orbital phase due to the eccentric orbit. Therefore, the variability of the equivalent width of the Hα line, the X-ray luminosity variability, and also the correlation between them, may just be an orbital dependent feature. Moreover, Bosch-Ramon et al. (2005) associated the correlation of the X-ray flux with the spectral hardening in the X-ray spectrum, which they found in the RXTE observation, with an increase in the accretion rate. These authors predict, hence, a shift of the electron energy distribution towards higher energies due to a more efficient acceleration of electrons in the jets caused by the increase in the accretion rate. Nevertheless, a direct correlation of mass accretion rate and X-ray flux would lead to a rather sharp increase in the X-ray flux at periastron passage when assuming a pure Bondi-Hoyle accretion model. This predicted X-ray flux peak is in contrast to the observations which show a quite smooth increase at this orbital phase. One explanation could be an accretion disc, that smoothes the flux changes and, therefore, the changes in the accretion rate along the orbit.

Accretion disc

There is, however, no typical observational evidence for the existence of an accretion disc around the compact object in this system. In general, the existence of an accretion disc goes along with a significant continuum flux in the optical light curve and the appearance of optical emission lines in the spectrum that exhibit variations of radial velocity.

This was not observed in the case of LS 5039 (McSwain & Gies 2002). Nevertheless, this does not exclude the existence of a large accretion disc. A strong photospheric continuum of the star can cover the emission of the accretion disc. In the X-ray domain, based on RXTE observations, no typical disc signatures, like e. g. a broad iron line, are found. However, this is not unusual for X-ray binaries in the low/hard state and was observed in other XRBs, too. On the

[1] For a wind accretion system, variations in the primary mass-loss rate are changes in the mean wind density.

other hand, the smoothing of the X-ray light curve through an accretion disc, which would soften the emission bumps in strength and duration around periastron passage as well as the existence of possible jets (assuming the radio outflows are due to jets), are strong indications for the existence of an underlying accretion disc. The accretion disc is most likely small and transient, and a disc that potentially rotates in different directions, rather than being large and stable (Martocchia et al. 2005). Nevertheless, if an accretion disc exists, it is very faint. Furthermore, it is not clear, which kind of accretion disc could be present in such circumstances (Bosch-Ramon et al. 2005). Martocchia et al. (2005) also argued that, when assuming the classical theory of accretion, the formation of a stable accretion disc is impossible in a binary system with the orbital properties of LS 5039, because the angular momentum carried by the transferred material is too small.

Direct accretion from wind

The non-observation of clear and typical features of accretion discs, reinforced the idea that the compact object in LS 5039 possibly accretes matter directly from the stellar wind. The accretion itself is basically favoured due to the ionisation of the matter in the wind by the X-ray source, because the wind consequently becomes slower and denser (McSwain & Gies 2002). Direct accretion from the wind varies with the orbit, but comparison with the light curve of GX 301−2,[2] which is similar to the light curve of LS 5039, suggested applying a Bondi-Hoyle accretion model in the case of LS 5039 also (Bosch-Ramon et al. 2005).

The assumption of the presence of jets in the system and the potentially non-existence of an accretion disc can be problematic in the view of the common understanding of jet formation, wherein jets are linked to an accretion disc. Because the accretion disc causes the ejection of material, jets are formed (Mirabel & Rodríguez 1999). Nevertheless, taking into account the radio observations which show clearly relativistic outflows and assuming direct accretion from the stellar wind, LS 5039 could be a rare case of a binary system which forms jets without having a stable accretion disc (Martocchia et al. 2005).

[2]GX 301−2 is a system, where the compact object accretes the non-spherically symmetric stellar wind (Leahy 2002).

7.3.2 Possible production mechanisms of TeV γ-ray emission in LS 5039

Particle acceleration

With the detection and identification of LS 5039 in the TeV energy range (Aharonian et al. 2005b), it was proved that X-ray binaries are able to accelerate particles to the TeV range. The jets and/or the regions where the ejected material interacts with the surrounding interstellar medium forming shock fronts are perfect and classical environments for accelerating particles to high and very high energies. The peculiarity of particle acceleration regions in binaries is the possible dependence on the orbital motion. By revealing such orbital dependences, one can draw conclusions about the location and the nature of the particle acceleration processes taking place (Aharonian et al. 2006c). There are ongoing intense discussions about whether the VHE γ-rays observed in LS 5039 are produced by primary leptonic or hadronic particle distribution. The leptonic scenario was mainly presented by Aharonian & Atoyan (1998) and Paredes et al. (2006), while the hadronic solution was pushed forward by Distefano et al. (2002) and Romero et al. (2003). Of course, a mixture of electrons and protons is also conceivable, and actually, would likely be the case when particle acceleration takes place in a jet. It is suspected that acceleration of protons in jets is possible due to the much larger magnetic fields, in particular, at the base of the jets.[3]

Production of electromagnetic emission in different wavelength ranges

The accelerated particles generate electromagnetic emission in different wavelength ranges. The major processes were discussed in Section 3.2. While it is indisputable that the radio emission is synchrotron radiation, produced by the accelerated particles which are probably injected into the relativistic jets, the X-ray emission is thought to be a result of inverse Compton and/or synchrotron processes within the jets (Bosch-Ramon et al. 2005). A much more difficult task is the identification of the production mechanism of the VHE γ-ray emission. To produce VHE γ-rays, it is necessary to have particles that are accelerated to very high energies and a dense target. The latter could be a dense stellar photon field or shock front.

For LS 5039 three different VHE γ-ray emission production mechanisms were discussed extensively during recent years. The first possibility is the up-

[3]Magnetic fields of $B \sim 10^5$ G are expected at the base of jets (Aharonian et al. 2006c).

scattering via inverse Compton processes of low energetic photons, mostly optical and UV photons from the optical companion star, by accelerated electrons which are non-thermal, relativistic, and, furthermore, responsible for the radio emission (Combi et al. 2004; Moldon et al. 2009).

The second possibility to produce the VHE γ-rays is due to neutral pion decay. The neutral pions are generated in interactions of accelerated and, therefore, high energetic hadrons, mostly protons, with surrounding X-ray photons and particles present in the stellar wind (Aharonian et al. 2005b, 2006c). In this case the X-ray emission is originated from the region, where accretion is taking place. This could be e. g. an accretion column or an accretion disc.

However, when a VHE γ-ray is produced near to the very intense stellar photon field, it can be absorbed by an optical photon via electron-positron pair production. The cross section for this process depends on the angle Θ between the two photons and also the energy threshold has a dependence on that angle of $1/(1-\cos\Theta)$ (see Section 3.2.4 and in particular Figure 3.4). This means that for head-on collisions the absorption is maximal and the resulting VHE γ-ray flux is low, while for VHE γ-rays that are parallel to the optical photons the absorption is minimal and the observable VHE γ-ray flux is high. Hence, this dependence is connected to the system geometry and the alignment between the VHE γ-ray production region, the stellar photon field, and the observer. It is expected that the VHE γ-ray flux is highest at the phase of inferior conjunction and has a minimum at superior conjunction (Aharonian et al. 2006c). The TeV observation corresponds to this behaviour, for which reason absorption was suggested as taking place in LS 5039. The efficiency of absorption depends on the energy of the VHE γ-rays and is expected to be strongest in the energy range of 0.2 to $2\,\mathrm{TeV}$. The observation that the flux at about $0.2\,\mathrm{TeV}$ appears to be stable, is in contrast to an interpretation of VHE γ-ray flux variation that is caused purely by VHE γ-ray absorption effects.

A third explanation for the appearance of a large amount of VHE γ-rays is the generation of electromagnetic cascades,[4] wherein electron-positron pairs and VHE γ-rays are generated and annihilated many times. Following the first absorption of a VHE γ-ray, an electron-positron cascade forms (Aharonian et al. 2006f; Bednarek 2006), if the magnetic field is lower than about $10\,\mathrm{G}$ (Aharonian et al. 2006c). For the binary LS 5039 a magnetic field of the order of $1\,\mathrm{G}$ is expected (Aharonian et al. 2006c). These cascades can only

[4]The principle of e^+e^--cascades is described in Section 4.2.1 in the context of electromagnetic showers.

form in an optically thick environment ($\tau_{\gamma\gamma} \approx 1$), i. e. the photosphere of the optical star and, for this reason, the acceleration site needs to be close to the compact object (Aharonian et al. 2005b). But, if an electromagnetic cascade is formed, it will reduce the absorption (Aharonian et al. 2006c) and will produce secondary electrons that should be observable in the X-ray energy range. Hence, the fraction of absorption, in principle, can be determined via the ratio of VHE γ-rays to X-rays.

Apart from the variability of the VHE γ-ray flux, an adequate model explaining the VHE γ-ray emission needs to take into account also, the phase dependence of the spectrum in this energy range. Three possible reasons for this variation are conceivable. First, in the leptonic scenario the maximum energy of the accelerated electrons can change with the phase, due to changes in the acceleration site or efficiency (Aharonian et al. 2006c). Second, the dominant radiation process can change. As a third possible reason for the spectral change, the angle dependence on IC scattering should be mentioned. Of course, a mixture of all three possibilities mentioned is possible, too.

H.E.S.S. observations show a hard VHE γ-ray spectrum ($\Gamma \sim 2.5$) at the superior conjunction phase interval, while at inferior conjunction phase interval the spectrum hardens even more ($\Gamma \sim 1.9$) and shows an exponential cutoff. The hard spectral index of $\Gamma \approx 2$ indicates that the electrons lose their energy mainly via inverse Compton scattering. If IC is the dominant process, the maximum electron energy is $E_{\max} \propto (B/\omega)^{3.3} \propto d^{3.3}$ (Aharonian et al. 2006f), where ω is the target photon density, B the magnetic field, and d the binary separation.[5]

A change in the crossover energy below which inverse Compton scattering dominates compared to synchrotron radiation, is the second possibility for changes in the VHE γ-ray spectral shape in LS 5039. This transition depends also on the magnetic field B and the binary separation d. For magnetic fields expected in the binary system ($B \sim 1\,\mathrm{G}$) and electron energies higher than a specific energy, synchrotron cooling is the dominant process, which is responsible for the X-ray radiation. The cause of the dominance of synchrotron losses for higher energetic electrons is a steepening of the VHE γ-ray spectrum (Moderski et al. 2005). The specific crossover electron energy mentioned, depends, finally, on the magnetic field B and the binary separation d and is the energy where the cooling times of IC energy losses and losses via synchrotron

[5] Both the magnetic field and the target photon density depend on the binary separation d: $B \propto 1/d$ and $\omega \propto 1/d^2$.

radiation are equal.

7.3.3 Neutron star or black hole?

The nature of the compact object is one of the key questions that arises when discussing LS 5039. Thus, if the compact object mass could be determined to be greater than $3\,\mathrm{M}_\odot$, the compact object would be a black hole, which would consequently rule out the pulsar wind scenario. But in principle, the optical and X-ray observations, and the orbital parameters determined by Casares et al. (2005b) and by Aragona et al. (2009) allow both possibilities: NS or BH. Also the determined mass function is too small to allow straight constraints. This uncertainty is also caused by the imprecisely known inclination angle. So, the system would have a high inclination orbit, if the compact object is a $1.4\,\mathrm{M}_\odot$ neutron star and a low inclination orbit, if the compact object is massive, i. e. $i \approx 30^\circ$ for $M_\mathrm{co} > 3\,\mathrm{M}_\odot$. The latter would lead to a constraint for the jet. It would be pointed close to the line-of-sight (Dubus 2006).

The wind accretion models prefer a NS as compact object with an inclination angle between $i = 40^\circ$ and $i = 60^\circ$ (McSwain et al. 2004). The NS is suggested as having a mass between 1 and $3\,\mathrm{M}_\odot$ (McSwain & Gies 2002). Casares et al. (2005b) estimate a lower limit of $M_\mathrm{co} = 1.49 \pm 0.11\,\mathrm{M}_\odot$ and prefer, with the assumption of so-called pseudo-synchronisation,[6] a solution as BH with a mass of $M_\mathrm{co} = 3.7^{+1.3}_{-1.0}\,\mathrm{M}_\odot$. But this assumption is far from being solid. These authors based their assumption on measurements of rotational broadening, and presume then that the circularisation and synchronisation might be relatively advanced in the system LS 5039. In fact, HMXRBs do not show corotation systematically (Conti 1978).

On the other hand, there are some other observational features that point to a BH as compact object, such as the lack of X-ray pulsations and the persistence of the non-thermal emission (Reig et al. 2003; Ribó et al. 1999).

7.3.4 Microquasar versus non-accreting pulsar

Based on the radio observations and their interpretation as jets, it was suggested that this source was a microquasar. But in principle, the powering source of the observed emission in the energy ranges from radio to TeV can be, first,

[6] Pseudo-synchronisation means, according to Casares et al. (2005b), that the rotational and orbital angular velocities are synchronised at the periastron passage or in other words the massive star is corotating at the angular orbital velocity at periastron.

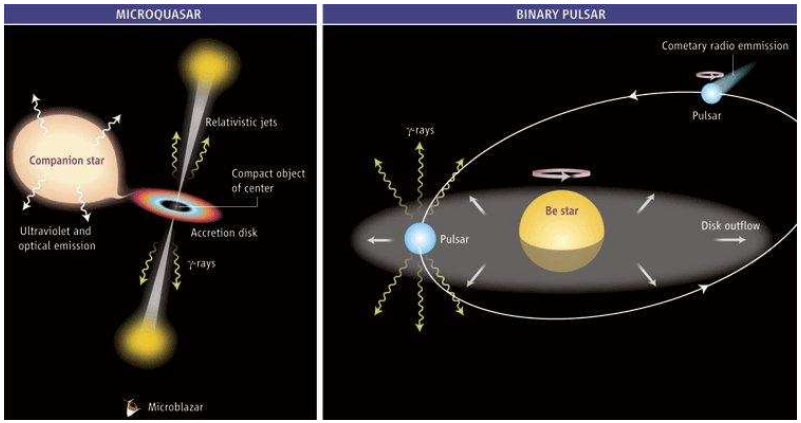

Figure 7.2: The two possible scenarios for LS 5039. *Left* panel: Microquasar model. If LS 5039 is a microquasar, then the accretion disc is very faint. The observed radio outflows are interpreted as relativistic jets. *Right* panel: Young pulsar model. A young non-accreting model of LS 5039 consist of an O star with a strong wind and a pulsar orbiting this optical component. Radio outflows are produced due to the strong stellar wind as a kind of cometary tail. Although, the figure shows a Be star with an outflowing material disc around it the picture is very similar compared to the model of LS 5039. Figure from Mirabel (2007).

accretion in a microquasar scenario or, second, wind interaction in a young non-accreting pulsar scenario. Both scenarios predict orbital changes of flux and spectral shape, but could basically be distinguished because of different morphologies and flux peak positions along the orbit (Moldon et al. 2009).

Microquasar scenario

Microquasars are XRBs that behave like a kind of scaled-down active galactic nuclei (AGN, Mirabel et al. 1992), especially because they have powerful, relativistic outflows, observable as resolved radio emission in high-resolution radio maps, which look like jets in AGN. In these jets particles are accelerated to large energies up to the TeV range (Perucho & Bosch-Ramon 2008). The radio emission morphology is composed of a central core and extended jet-like outflows. The latter can appear as a symmetric double-sided jet or as an asymmetric one-sided jet due to projection effects and Doppler boosting (Mirabel &

Rodríguez 1999). The jets can precess, can be bent and/or can be disrupted, when interacting with the clumpy or dense stellar wind of the bright stellar companion (Perucho & Bosch-Ramon 2008).

Young pulsar scenario

Alternatively, it was suggested that the source was a non-accreting pulsar binary system (Dubus 2006). This is a reasonable assumption, even so no pulsation has been observed in the radio and the X-ray bands. The VHE γ-ray emission then arises from the pulsar wind material shocked by the interaction with the stellar companion wind and afterwards flowing away in a 'bow' shaped nebula extending away from the stellar companion (Maraschi & Treves 1981; Tavani & Arons 1997; Moldon et al. 2009). The appearance is comparable with a comet-shaped tail with a peak of emission a few AU behind the pulsar. It is expected that the emission morphology and direction change periodically with orbital motion of the pulsar, since the relative positions between the pulsar and the companion star changes along the orbit (Dubus 2008). The strength of this direction variability depends on the inclination angle. If the orbit is seen under an inclination nearly edge on, almost no changes would be observable. For example, a change of morphology and, hence, an identification as non-accreting pulsar was proposed by (Dhawan et al. 2006) for the system LS I $+61^{\circ}303$. Actually, LS I $+61^{\circ}303$ is the only HMXRB which is proposed as a pulsar system and shows no pulsation, neither in radio nor in X-rays. Accordingly, Moldon et al. (2009) estimate for LS 5039 that it is much easier to fit the mentioned results with the features predicted for a non-accreting pulsar, than with the features of a simple microquasar scenario. A pulsar in LS 5039 is young or at least middle aged (Martocchia et al. 2005), because the elapsed time since the supernova explosion that created the binary system is calculated to only about $1.1\,\mathrm{Myr}$ (Ribó et al. 2002). Martocchia et al. (2005) also provide an alternative idea how to produce the radio outflows. If the pulsar rotates very fast, it would be impossible for the compact object to accrete matter and the matter is, instead of being accreted, ejected in a propeller-like mechanism. How this mechanism works exactly, or if this mechanism is possible considering the influence of the strong stellar wind, and, finally, if it would be able to generate collimated jets, is not yet clear.

Discussion – Is LS 5039 a microquasar or a non-accreting pulsar system ?

Up to now, observations have not been able to solve the question, whether LS 5039 is a microquasar or a non-accreting pulsar system. Both possible interpretations are discussed, observations are fitted with corresponding models, and no clear evidence of one or the other interpretation is found. For example Bosch-Ramon et al. (2005) interpret the data as accretion, which would be a hint against the young non-accreting pulsar scenario. In contrast, Moldon et al. (2009) explain the observed changes in morphology to be hardly consistent with a simple and shockless microquasar scenario. Only further observations, simultaneously performed with the best available satellites nowadays in the keV to TeV energy range, like *Suzaku*, Fermi-GLAST and *H.E.S.S.*, can hopefully solve the open questions on this exceptional source.

7.3.5 Possible production sites of TeV γ-ray emission in LS 5039

The obvious production sites of TeV VHE γ-rays are the jets or the region where the pulsar wind and the wind from the stellar component collide and a shock is formed. The *H.E.S.S.* observations reveal clearly a point source, thus the size of the VHE γ-ray production area is limited by the angular resolution of *H.E.S.S.*. In fact, the production region is expected to be much smaller. Under the assumption of a distance of $2.5\,\mathrm{kpc}$, this limits the size to about $0.3\,\mathrm{pc}$ (Aharonian et al. 2006c), while the radio outflows have a maximal size of about $1\,000\,\mathrm{AU}$ (Casares et al. 2005b).

If a jet is present in LS 5039, the particle acceleration can take place directly inside the jet, along the jet, and at the region where the jet collides with the ambient matter (Heinz & Sunyaev 2002). The VHE γ-rays can have q leptonic or a hadronic origin, because electrons and protons are both accelerated in the high magnetic fields present in the jets. The accelerated particles can generate VHE γ-rays. In addition X-rays are emitted as a result of inverse Compton scattering events between relativistic electrons and photons, which are either generated as secondaries in synchrotron processes or coming from the optical stellar wind (see Bosch-Ramon et al. (2005) and references therein e. g. Kaufman Bernadó et al. 2002 and Georganopoulos et al. 2002). The accelerated particles interacting with the photons of the stellar wind can generate VHE γ-rays via several radiation processes, like inverse Compton scattering (Bosch-Ramon & Paredes 2004; Bosch-Ramon et al. 2005; Martocchia et al. 2005) or neutral pion generation and decay (Aharonian et al. 2006c). Hence, the VHE γ-ray production can

be located also in the jet or can be in each region, where the particles, which are accelerated in the jet, interact with the photons of the stellar wind.

In the case of the non-accreting pulsar scenario the acceleration site is the shock, which forms due to the interaction of the pulsar wind and the wind of the bright optical star. This region separates the binary into two parts. In the region between pulsar and shock dominates the pusar wind. The relativistic electrons initiate cascading processes. But assuming that the relativistic electrons are frozen into the magnetised pulsar wind, Sierpowska-Bartosik & Torres (2007) considered only inverse Compton cascades in their calculation. However, secondary γ-rays generated along the way can propagate through the shock into the region of the dense stellar wind, where absorption can take place.[7] The parameters of the LS 5039 binary system are such, that VHE γ-ray variations are expected, due to separation changes between the components. The varying distance between the components has influence on the efficiency of the ongoing processes, but the separation is, even at apastron, small enough to maintain the particle acceleration as well as the VHE γ-ray production (Sierpowska-Bartosik & Torres 2007; Dubus et al. 2008).

7.3.6 The keV– TeV connection in LS 5039

In most XRBs, the main X-ray emission fraction originates from a hot thermal comptonised plasma, which is accreted onto the compact object. In LS 5039 this is not the case, because the hard spectral index and the missing emission lines in the X-ray domain indicate a non-thermal origin of the X-ray emission (Takahashi et al. 2009)

The correlation in the light curves of X-ray and VHE γ-rays supports the non-thermal origin of the X-ray emission and, in addition, suggests a single parent electron distribution. This could be concluded both from the *Suzaku* observation (see Takahashi et al. (2009) and Section 7.2) and the *INTEGRAL* observation (see Hoffmann et al. (2009) and Section 7.1). The energy distribution of the parent electron population needs to be rather hard. The observed power-law index in the X-rays of about $\Gamma \approx 1.5$ and the condition that the X-rays are produced by synchrotron radiation, require a power-law index for the underlying electron distribution of about $\Gamma \approx 2$. This is also in agreement with the interpretation, that the TeV emission is generated by inverse Compton scattering of stellar photons.

[7] Absorption can only be effective within the photosphere of the stellar companion which is in the case of LS 5039 at a distance of about 1 AU (Aharonian et al. 2006c).

The region, where the parent particle population is located, must have a larger distance from the compact object, because otherwise the TeV γ-rays would be absorbed in the dense stellar photon field. This absorption would be followed by the generation of electron-positron pairs and the subsequently emitted X-ray emission would be too intense, compared to the observations. In additon, a spectral break would have to be seen in the spectrum observed with *Suzaku*, which is not the case (Takahashi et al. 2009). This spectral break would be caused by the photon energy dependence on the pair production cross section. The spectral break could only be prevented for magnetic field values inconceivably high in the VHE γ-ray emission region ($B \geq 1\,\mathrm{kG}$). Instead, the magnetic field strength in LS 5039 is calculated by Takahashi et al. (2009) to be a few Gauss.

The suggestion that both the X-ray variability and the TeV modulation, and also the correlation between each other, are originated by emission induced by the same high energetic electron population, disregards an interpretation of TeV variability based on the interaction of the electrons and VHE γ-rays with the stellar photons from the massive star. As already mentioned, the two main possibilities to explain the TeV variability are anisotropic IC scattering and photon-photon pair production (Khangulyan et al. 2008a; Dubus et al. 2008). But, both possibilities prevent the primary particle or photon from contributing to the X-ray flux and consequently to the X-ray modulation.

An alternative interpretation, which was already suggested for the binary system PSR B1259−63 by Khangulyan et al. (2007), was suggested also for LS 5039 by Takahashi et al. (2009). The authors suggested a dominance of adiabatic losses as the reason for the changes in the synchrotron generated X-ray fluxes. The circumstances in which such adiabatic cooling of electrons can take place in a massive binary system are caused by "complex (magneto)hydrodynamical processes" like they occur in regions where the jet or the pulsar wind interacts with the dense wind of the stellar companion (see e. g. Bogovalov et al. 2008; Perucho & Bosch-Ramon 2008). The variability of the fluxes would then simply be the modulation of the adiabatic cooling of the electrons and a result of the orbital motion (see e. g. Khangulyan et al. 2008b). Two characteristics of adiabatic losses should be mentioned here. The initial spectrum is not changed by adiabatic losses and the timescales for adiabatic cooling are about 1 s (Takahashi et al. 2009).

In addition to the modulation caused by the adiabatic losses, the VHE γ-rays can be modulated by photon-photon absorption (e. g. Böttcher 2007) and anisotropic IC scattering. Therefore, the order of modulation in this energy

range can be significantly increased compared to the variability seen in X-rays. Furthermore, the spectrum in the TeV range can become harder due to the IC scattering (Khangulyan & Aharonian 2005).

Takahashi et al. (2009) present a model in which the electron energy distribution is a power law with an index of $\alpha_{\mathrm{e}} = 2\Gamma_{\mathrm{X}} - 1 \approx 2$. To fit the observed hard TeV spectra ($\Gamma \sim 2$, Aharonian et al. 2006c), it is necessary to include anisotropic IC scattering into the model spectrum at the INFC phase interval. For SUPC phase interval it is, in addition, essential to restrict the emission location to a distance about $2 \times 10^{12}\,\mathrm{cm}$ away from the compact object in a direction perpendicular to the orbital plane. This is of course in contradiction with the standard pulsar scenario.

7.4 Conclusions from *INTEGRAL* observations

The *INTEGRAL* observations do not have the ability to distinguish between the microquasar or pulsar scenario as well as to identify the nature of the compact object. But the results give indications how to interpret the X-ray emission of the source and fitting the results into the multi-wavelength picture of the source, can insert an additional issue to the multi-wavelength behaviour of the source. Thus, e. g. one would expect a rather sharp flux maximum near periastron if accretion is the main production mechanism of the hard X-ray emission. Our result does not favour this explanation. Furthermore, the variability of hard X-rays is in phase and in correlation with the VHE γ-ray emission. This suggests that the emission in both energy ranges originate in the same region and possibly originates from particles produced in the same acceleration process. Altogether this reveals that a simple explanation of TeV variability as a consequence of only γ-γ absorption (Aharonian et al. 2006c) cannot be true. More complicated scenarios that involve γ-γ absorption (e. g. Dubus 2008) are still conceivable, but one would expect X-ray synchrotron emission generated by secondary electrons (Bednarek 1997). The secondary electrons are produced in cascades, which are initiated through γ-γ absorption processes. The amount of absorption involved can be constrained, due to the soft and hard X-ray flux levels. Our result of a low flux upper limit at SUPC in connection with the TeV emission detected in this phase interval casts doubt on models including only one emission region close to the compact object (Bosch-Ramon et al. 2008). Although some predictions of X-ray variability (Paredes et al. 2006) seem not in agreement with our observations, it is not possible to emphasise just one sce-

nario with respect to others. Hadronic scenarios (Romero et al. 2003; Romero & Vila 2008) can still take place in this source.

CHAPTER 8

TeV plerions

Together with the TeV binaries a second group of Galactic sources emitting VHE γ-rays is very interesting. Several VHE γ-ray sources are associated with pulsar wind nebulae (PWN) and, therefore, are called "TeV plerions". In the following section the object class of PWNs is described. Afterwards the VHE γ-ray / X-ray connection in these sources is introduced and finally three sources, so-called middle-aged rotation-powered pulsar wind nebulae, and their appearances in VHE γ- and hard X-ray are described in detail. The whole section is closed with a short conclusion. This chapter is based on Hoffmann et al. (2007).

8.1 Rotation-powered pulsar wind nebulae (RPWN)

Rotation-powered pulsar wind nebulae (RPWN) are a special subclass of supernova remnants (see Section 2.1) and contain an isolated neutron star that drives a relativistic wind of particles into the ambient medium. The powering source is the rotational energy of the neutron star which is partially transformed into the highly relativistic wind of particles. This particle flow diffuses in the ambient medium and fuels an extended non-thermal emission region. If the RPWN is middle aged ($t \approx 10\,\mathrm{kyrs}$), the wind hits the reverse shock of the supernova remnant ejecta and thus is modified (Blondin et al. 2001). A relativistic standing shock forms. Generally this shock is located at a distance of typically $10^{16} - 10^{17}\,\mathrm{cm}$ from the central object and is believed to be the site of particle acceleration. Among the possible ways of accelerating particles, the Fermi acceleration mechanism (see Section 3.1.1) has been considered to be

a good candidate to explain the broad band power-law distribution of the pair plasma in the downstream region.

8.1.1 VHE γ-ray / X-ray connection in RPWN

As described above a standing shock forms in the PWN environment and constitutes the site of particle acceleration (see Section 3.1). To explore the acceleration of particles, the hard X-ray band ($20 - 100\,\mathrm{keV}$) and the γ-ray band ($0.1 - 100\,\mathrm{MeV}$) are the crucial observational windows, because synchrotron emission of accelerated electrons is expected to be the dominant radiation process in these energy ranges. Moreover, the life-time of the electrons emitting in the hard X-ray band is rather limited

$$t_{1/2} \approx 8.4\,\mathrm{yrs}(B_{-4})^{-3/2}(\epsilon/20\,\mathrm{keV})^{-1/2} \tag{8.1}$$

with $B_{-4} = B/(10^{-4}\,\mathrm{G})$. Additionally, unpulsed hard X-rays should be emitted only in a very confined volume close to the acceleration site in general.

The archetypal RPWN, the Crab nebula, is well studied and an example of a young ($t \ll 10\,\mathrm{kyrs}$) RPWN. It is bright and therefore observations in a wide energy range are possible to determine the emitted power. In contrast to young RPWN, middle-aged RPWN are less bright and, hence, similar detailed energy spectra have not yet been obtained for this object class. A sketch of a rotation-powered pulsar wind nebula showing the regions of the emitted radiation in the different energy ranges is given in Figure 8.1.

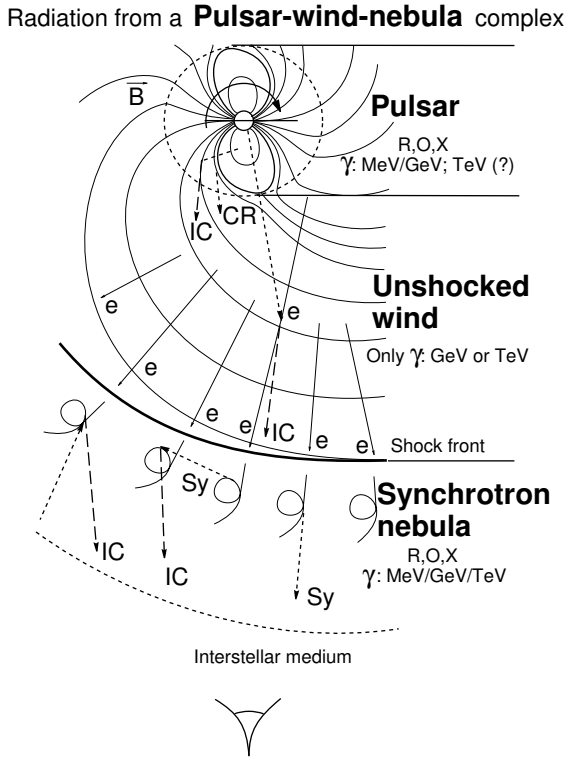

Figure 8.1: Sketch of a rotation-powered pulsar wind nebula. The surroundings of a pulsar wind nebula can be distinguished into three regions of different physical conditions. First, the direct environment of the pulsar, where radio, optical and X-ray radiation is emitted. The VHE γ-rays are generated due to curvature, synchrotron and inverse Compton processes within the light cylinder. This emission is pulsed. The second region is the area between pulsar and shock, which is dominated by the pulsar wind. In this unshocked wind region only VHE γ-rays are produced due to relativistic bulk-motion Comptonisation. When the particles reach the third region, the synchrotron nebula, they emit broad-band (in the radio, optical, and X-ray band), synchrotron and inverse Compton radiation. Figure from Aharonian & Bogovalov (2003).

8.2 Analysis of selected RPWN

As described in Section 4.3.1 a regular observation, performed with the *INTEGRAL* instruments, was the survey of the Galactic plane. For the two mosaics presented in the following, public *INTEGRAL* observations were used.

The mosaic centred on the region of the "Kookaburra" incorporates all public *INTEGRAL* data from January 2003 until August 2005 (these are 378 ScWs from ScW 003000120010 to 034700120010, respectively) up to a maximal distance of 10° to the source position of the Kookaburra region. The total exposure time for this mosaic is about $940\,\mathrm{ks}$. In this mosaic MSH 15−52 can also be found due to the large FoV of the *INTEGRAL* satellite. But there are more public data for this pulsar available in the archive. The other mosaic uses all public *INTEGRAL* data available from April 2003 until November 2005 (these are 562 ScWs from ScW 005800090010 to 038000100010, respectively) for a maximal distance of 4.5° from the position of the Vela pulsar. The total exposure time for this mosaic is $\approx 1.3\,\mathrm{Ms}$. Both mosaics were generated using the standard *INTEGRAL* Off-line Scientific Analysis 5.0.

8.2.1 PSR J1513–5908 (MSH 15–52)

PSR J1513−5908 is a young RPWN with an age of about 1500 years only. It is associated with the MSH 15−52 supernova remnant. The spin period is about 150 ms and the powerful pulsar is seen in the X-ray, gamma-ray and radio energy band.

MSH 15−52 was observed with *H.E.S.S.* in 2005. The observation method used was the so-called *wobble* mode, in which the observation is performed with a small angular distance, here 0.5°, from the centre of the field of view. The analyses were made on a data sample with a total live time of $22.1\,\mathrm{h}$ and a mean zenith angle of 37°. The excess sky map of MSH 15−52 is shown in Figure 8.3 (Aharonian et al. 2005d).

Figure 8.2 shows the *INTEGRAL* mosaic for the region around the pulsar PSR J1513−5908. It is interesting to note that the emission seen by *INTEGRAL* is possibly spatially resolved and seems to be extended.

8.2.2 PSR J0835–4510 (Vela)

The *H.E.S.S.* observations were performed in 2004 and 2005 via the *wobble* method with an angular distance of 0.5° from the Vela pulsar position ($\alpha = 09^\mathrm{h}35^\mathrm{m}20^\mathrm{s}, \delta = -45^\circ 10' 35''$ J2000.0). A total observation time of $16.4\,\mathrm{h}$ was

analysed (Aharonian et al. 2006a) and the average zenith angle was 30.2°. The sky image seen with *H.E.S.S.* is shown in Figure 8.5 (Aharonian et al. 2006a).

The detection level of the Vela pulsar for the analysed *INTEGRAL*/ *IBIS* image is about $44.2\,\sigma$ (Figure 8.4). In total an exposure time of $\approx$ 1.3 Ms is analysed in the revealed mosaic. Most of the emission above $20 - 60\,\mathrm{keV}$ is unpulsed (Hermsen et al., priv. communication). No indication for an extended emission in hard X-rays from the Vela X region is observed (Horns et al. 2006). Combining spectral data of the ASCA satellite with the non-detection, we conclude that there exists a spectral cut-off in the energy range between $10 - 20\,\mathrm{keV}$.

8.2.3 PSR J1420–6048 (Kookaburra)

TeV emission in this sky region was discovered by *H.E.S.S.* (Aharonian et al. 2006d) and was associated with two radio wings of the Kookaburra complex. This confirms the non-thermal nature of these sources and establishes the connection between VHE γ- and X-rays due to the association with the two X-ray pulsar wind nebulae candidates.

The observations of the Kookaburra region with *H.E.S.S.* were part of the extended Galactic plane survey performed in 2005, which range in galactic longitudes from $300^\circ < l < 330^\circ$ and in galactic latitudes from $-3^\circ < b < +3^\circ$. Some additional observations of this sky region were performed in May and August 2005. Finally, a total of 18.1 h with a *wobble* offset angle of 0.7° from the Kookaburra position ($\alpha = 14^\mathrm{h}20^\mathrm{m}00^\mathrm{s}, \delta = -60^\circ45'00''$ J2000.0) and an average zenith angle of 35.3° were analysed. The resulting sky image is shown in Figure 8.7 (Aharonian et al. 2006d).

Inverse Compton scattering of accelerated electrons on the Cosmic Microwave Background is assumed to be an explanation for the Very High Energy γ-rays.

The *INTEGRAL* mosaic for the energy range of $20 - 40\,\mathrm{keV}$ shows a faint signal of $5\,\sigma$ at the position of the PSR J1420−6048 (Figure 8.6). The pulsar PSR J1420−6048 belongs to the class of middle-aged pulsars where the RPWN interacts with the reverse shock of the supernova remnant.

Interestingly, there is no *INTEGRAL* counterpart to the "Rabbit" RPWN candidate (Roberts et al. 1999; Ng et al. 2005). This object is presumably powered by a young pulsar. This pulsar is not yet clearly detected. While the two TeV plerions show a similar morphology and energy spectrum, their X-ray properties appear to be very different.

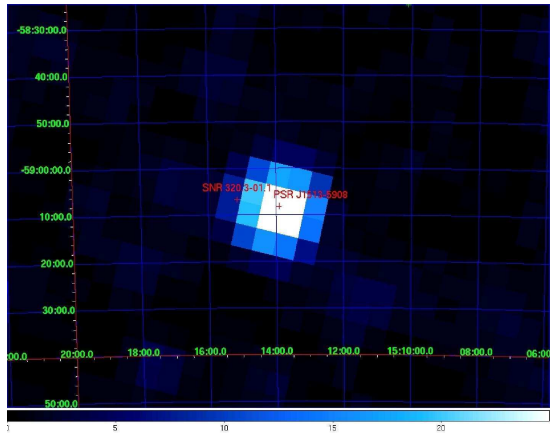

Figure 8.2: PSR J1513−5908 seen with *INTEGRAL*. The colour scale indicates the significance in the range from $0 - 25\ \sigma$.

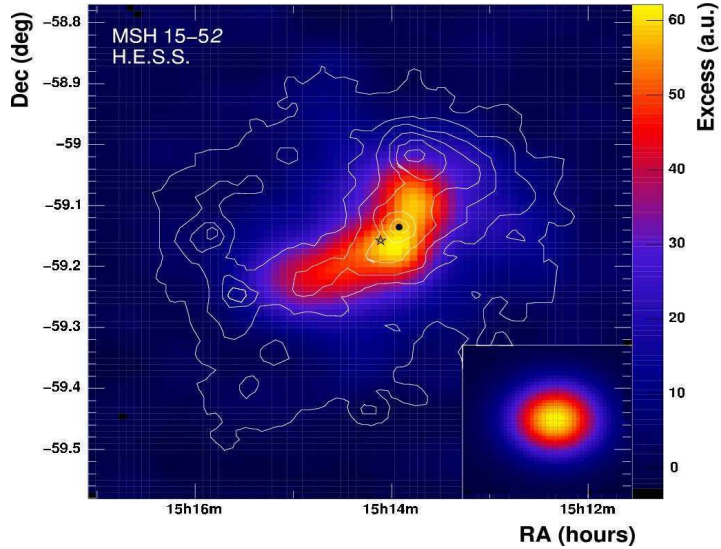

Figure 8.3: PSR J1513−5908 seen with *H.E.S.S.* (Aharonian et al. 2005d). Overlaid (white contour) is the *ROSAT* X-ray ($0.6 - 2.1$ keV) count rate.

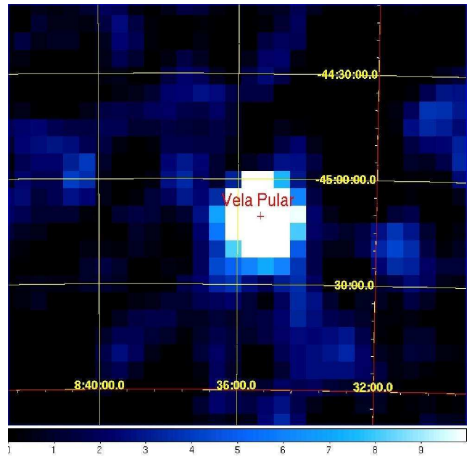

Figure 8.4: Vela pulsar seen with *INTEGRAL*. The mosaic shows the significance map for the energy band between $20 - 40\,\mathrm{keV}$. The scale is truncated below 0 and above $10\,\sigma$.

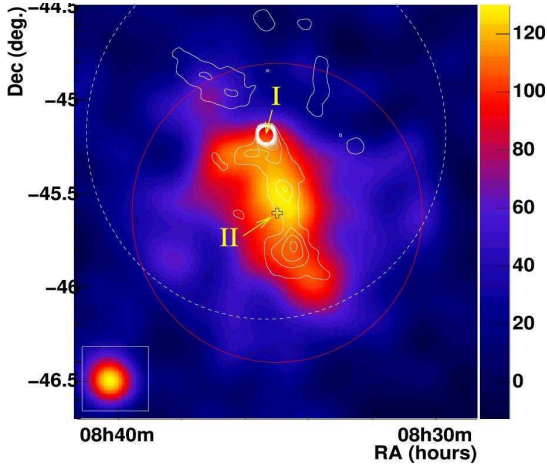

Figure 8.5: PSR J0835−4510 seen with *H.E.S.S.* (Aharonian et al. 2006a). The sky image is smoothed with a Gaussian of width 0.09°. The position of PSR J0835−4510 is marked with I. The white contours belong to the X-ray emission observed by *ROSAT*. The left bottom corner shows the size a point source would appear, when the same method of analysis is used.

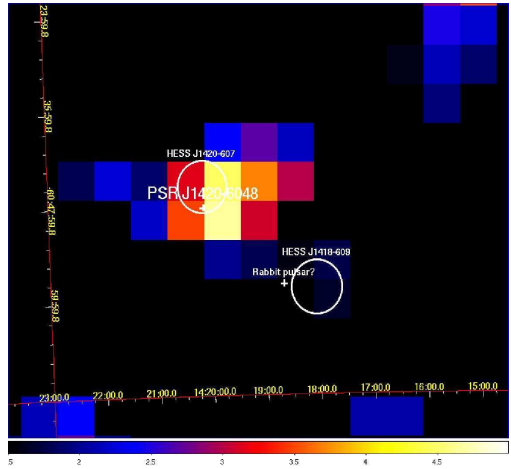

Figure 8.6: *IBIS* significance map in the energy range $20 - 40\,\mathrm{keV}$ of the Kookaburra region. The colour scale is truncated below $+1.5\,\sigma$.

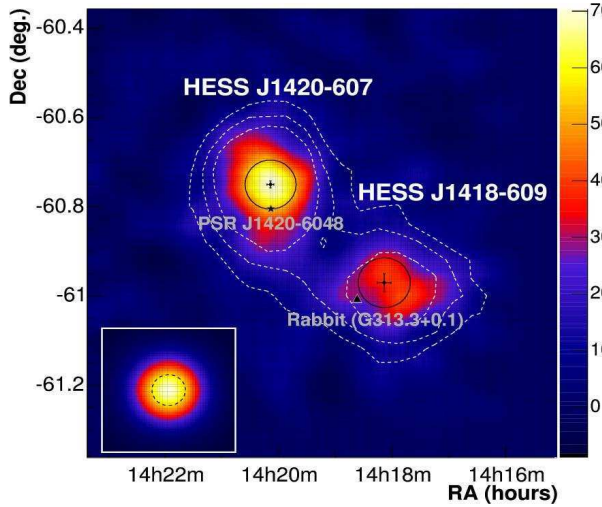

Figure 8.7: The Kookaburra region seen with *H.E.S.S.* (Aharonian et al. 2006d). Shown as colour scale is the smoothed excess map overlaid by the significance contour. The inlaid box in the bottom left shows the point spread function for the *H.E.S.S.* observation.

8.3 Results

Amongst the sources detected by the *INTEGRAL* satellite only a rather small fraction of a few per cent have been identified as young or middle-aged RPWN (see Table 8.1). Focussing on RPWN which have been detected as TeV plerions,[1] the analysis of archival *INTEGRAL* data reveals, in addition to already known *INTEGRAL* sources, an evidence of hard X-ray emission from the "Kookaburra" TeV plerion G313.3+0.6.

8.4 Conclusions

The comparison between detected TeV plerions and their possible counterparts in hard X-rays reveals that some of the pulsars associated with these TeV plerions are *INTEGRAL* sources including young and middle-aged RPWN. This correlation can reveal additional and interesting information on these sources, since the *INTEGRAL* observations are complementary to the TeV observations: The unpulsed hard X-rays are presumably tracing the on-going particle acceleration at the relativistic standing shock. In the frame of ion induced acceleration, the observed hard X-ray spectrum constrains the bulk Lorentz factor of the relativistic wind and its composition.

[1] The number of TeV sources identified as PWN is 14 on the actual list of *H.E.S.S.* and MAGIC sources. (For reference see the footnote 13 in Section 4.2.4).

Table 8.1: Some parameters of young – PSR J0534+2200 and PSR J1513−5908– and middle-aged – PSR J0835−4510 and PSR J1420−6048– pulsars seen with *INTEGRAL* and *H.E.S.S.*. With the exception of VHE and X-ray luminosities, all values are from Manchester et al. (2005). The luminosities in the very high energy range are calculated based on the power-law values given in the following references: [a] (Masterson & et al. 2005), [b] (Aharonian et al. 2005d), [c] (Aharonian et al. 2006a), [d] (Aharonian et al. 2006d). The X-ray luminosities – except for PSR J1420−6048– are based on the power-law values given in the *INTEGRAL* Reference Catalog Version 26 (Bird et al. 2006).
(*) Due to the faint detection for PSR J1420−6048 only an estimation for the X-ray flux and thus for the X-ray luminosity is possible. The second VHE source in the Kookaburra region, G313.3+0.1, is not seen with *INTEGRAL* and therefore not listed in the table.

Name	PSR J0534+2200 (Crab Nebula)	PSR J1513−5908 (MSH 15−52)	PSR J0835−4510	PSR J1420−6048 (G313.3+0.6)
P / [ms]	33	151	89	68
$\dot{P}$ / [s/s]	$4.23 \cdot 10^{-13}$	$1.54 \cdot 10^{-12}$	$1.25 \cdot 10^{-13}$	$8.32 \cdot 10^{-14}$
$\log_{10} \dot{E}$ / [erg/s]	38.7	37.2	36.8	37
τ / [kyrs]	1.24	1.55	11.37	13
distance / [kpc]	2.0	4.4	0.29	7.69
$\log_{10} L_{\mathrm{VHE}}$ / [erg/s] $(1\,\mathrm{TeV} - 10\,\mathrm{TeV})$	34.4 ([a])	34.6 ([b])	32.9 ([c])	34.9 ([d])
$\log_{10} L_{\mathrm{X}}$ / [erg/s] $(20 - 40\,\mathrm{keV})$	36.6	35.2	32.7	≈ 34.6 (*)

CHAPTER 9

Other sources in the FoV

9.1 A very crowded field

The analysis of LS 5039 was difficult due to of the many other sources in the field of view and the coded mask technique of the *INTEGRAL* instrument. This combination is, on the other hand, a gain, because due to the analysis procedure it is necessary, when analysing a faint source, to extract spectra and light curves from all brighter sources then the one, the user is interested in. The details of analysis are described in Chapter 6. The sky image is centred on LS 5039 and a total exposure time is about $2.99\,\mathrm{Ms}$ in maximum. In the following description, we concentrate on sources in the central FoV with an extent of about 9° by 9° and an exposure time of more than $2.5\,\mathrm{Ms}$.

9.1.1 *H.E.S.S.* sources

All *H.E.S.S.* sources located in the part of the sky image shown in Figure 9.1 are listed in Table 9.2. Names, positions and source types are from the HESSCAT, the *H.E.S.S.* Source Catalog.[1] The catalogue is the reference for positions, VHE γ-ray fluxes, and possible counterparts in Table 9.2. The source types are from the references listed in Table 9.1. The *INTEGRAL* significance given in the table are taken from the significance map provided by the *INTEGRAL* analysis. They are not integrated over the pixels contributing to the possible source. Instead of that, the values of the pixel the *H.E.S.S.* source position falls into is quoted. So, they need to be understood as a lower limit. The values in

[1] The *H.E.S.S.* Source Catalog is provided by the *H.E.S.S.* collaboration at `http://www.mpi-hd.mpg.de/hfm/HESS/pages/home/sources/`

Table 9.1: References of *H.E.S.S.* source types listed in Table 9.2.

H.E.S.S. name	References
HESS J1800-240A	(Aharonian et al. 2008b)
HESS J1800-240B	(Aharonian et al. 2008b)
HESS J1800-240C	(Aharonian et al. 2008b)
HESS J1801-233	(Aharonian et al. 2008b)
HESS J1804-216	(Aharonian et al. 2005a, 2006b)
HESS J1809-193	(Aharonian et al. 2007)
HESS J1813-178	(Aharonian et al. 2005a, 2006b)
HESS J1825-137	(Aharonian et al. 2005a, 2006b, 2005e, 2006e)
HESS J1826-148	(Aharonian et al. 2005b, 2006e; de Naurois 2007)
HESS J1834-087	(Aharonian et al. 2005a, 2006b)
HESS J1837-069	(Aharonian et al. 2005a, 2006b)
HESS J1841-055	(Aharonian et al. 2008a)

brackets indicate a neighbouring pixel with a higher significance value, which would certainly be included, if we integrate over several pixels.

9.1.2 *INTEGRAL* sources

All *INTEGRAL* sources located in the part of the sky image shown in Figure 9.2 are listed in table Table 9.3. Names, position and source types are from the ISDC *INTEGRAL* Reference Catalog.[2] The last column shows, if the source is detected with a significance level of at least $3\,\sigma$.

In Table 9.4 and Table 9.5 all detected *INTEGRAL* sources with a significance larger than $3\,\sigma$ are listed. Of course, only sources with a significance larger than approximately $6\,\sigma$ can be claimed as detections. The positions of the sources are fitted and both values, the ISDC reference catalogue position and the fitted position are listed (Table 9.4). The determined count rates and detection significance in the energy ranges $25 - 60\,\mathrm{keV}$ and $60 - 200\,\mathrm{keV}$ are given (Table 9.5). Sources listed in Table 9.4 and Table 9.5 but not in Table 9.3 are detected in the FoV, but have an exposure time shorter than $2.5\,\mathrm{Ms}$.

[2]The *INTEGRAL* Reference Catalog is provided by the ISDC at
`http://isdc.unige.ch/Data/cat/27/catalog.html`

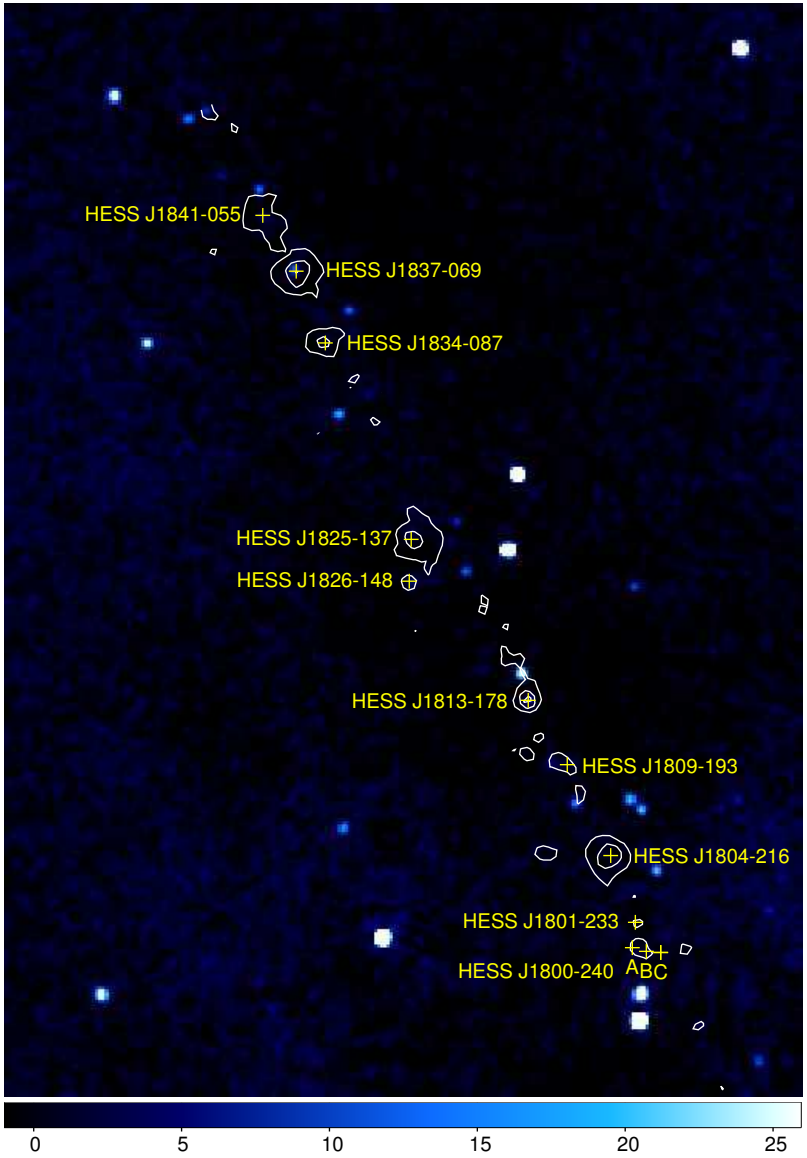

Figure 9.1: *INTEGRAL* mosaics of LS 5039 in the energy range $25 - 60\,\mathrm{keV}$. The positions of the centre of gravity of known *H.E.S.S.* sources are marked in yellow. The white contours show the extension of these *H.E.S.S.* sources.

Table 9.2: *H.E.S.S.* sources in the explored *INTEGRAL* FoV. All public *H.E.S.S.* sources, which are on the official source list and have an exposure time in this FoV with more than 2.5 Ms are listed.

H.E.S.S. name HESS ...	RA (J2000) [h]	DEC (J2000) [deg]	Gal. long. [deg]	Gal. lat. [deg]	Flux (max) [C.U.]	Rad. ["]	Counterpart or other name(s) of source	type	*INTEGRAL* excess? signif. (25-60 keV)
J1800-240A	18:01:58	-23:57:43	6.14	-0.63	0.03	9	G006.1-006 (W 28)	SNR /	0.6
J1800-240B	18:00:26	-24:02:20	5.90	-0.37	0.03	9	W 28-A2	molecular	2.0
J1800-240C	17:58:52	-24:03:07	5.71	-0.06	0.018	1	(W 28)	clouds	1.0
J1801-233	18:01:42	-23:20:06	6.66	-0.27	0.03	10	W 28		-1.5
J1804-216	18:04:31	-21:42:00	8.40	-0.03	0.25	12	GRO J1801-2320 G8.7-0.1 / W30 ? PSR J1803-2137 ?	SNR (shell) PWN?	0.1
J1809-193	18:09:21	-19:27:00	10.92	0.08	0.14	32	PSR J1809-1917 ?	PWN?	1.4
J1813-178	18:13:36	-17:50:24	12.81	-0.03	0.06	2.2	G12.8-0.02; AX J1813-178	SNR (shell)	7.1
J1825-137	18:26:02	-13:45:36	17.82	-0.74	0.17	9.6	PSR J1826-1334; 3EG J1826-1302 ?	PWN? unidentified	1.2
J1826-148	18:26:15	-14:49:30	16.90	-1.28	0.03	0	LS 5039	binary / MQ? Pulsar?	6.4
J1834-087	18:34:46	-8:45:36	23.24	-0.31	0.08	5.4	G23.3-0.3 / W41?	SNR (shell)	1.5
J1837-069	18:37:38	-6:57:00	25.18	-0.12	0.132	7.2	G25.5+0.0 ?; AX J1838.0-0655 ?	SNR? unidentified?	8.1 (13.2)
J1841-055	18:40:55	-5:33:00	26.80	-0.20	0.13	25		unidentified / binary? / PWN? SNR?	4.1 (4.9)

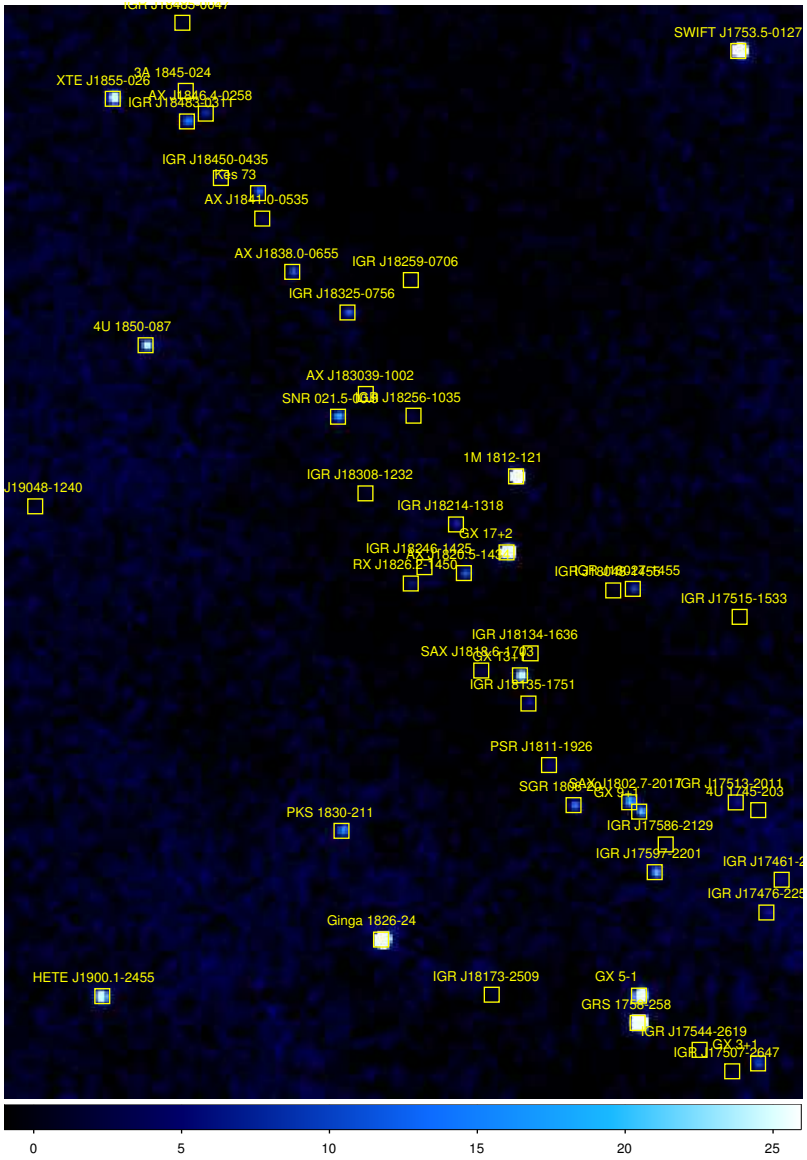

Figure 9.2: *INTEGRAL* mosaics produced for LS 5039 in the energy range from 25 keV to 60 keV. All *INTEGRAL* sources listed in the ISDC *INTEGRAL* Reference Catalog version 27 are marked.

Table 9.3: *INTEGRAL* sources in the explored *INTEGRAL* FoV. All *INTEGRAL* sources, which are on the ISDC *INTEGRAL* Reference Catalog version 27 and have an exposure time in this FoV with more than 2.5 Ms are listed.

Source name	RA (J2000) [°]	DEC (J2000) [°]	Source type	signif. $> 3\sigma$ [25 − 60 keV]
IGR J17461-2204	266.5333	-22.05889	X-ray binary	yes
IGR J17476-2253	266.9042	-22.88694	X-ray binary	yes
GX 3+1	266.9833	-26.56361	LMXRB showing QPO and bursts	yes
H 1745-203	267.2229	-20.36722	LMXRB Globular cluster, hard transient	
IGR J17507-2647	267.6750	-26.79194	X-ray binary	
IGR J17513-2011	267.8068	-20.20405	Seyfert galaxy type 2	
IGR J17515-1533	267.8833	-15.54389	X-ray binary, hard transient	
SWIFT J1753.5-0127	268.3677	-1.451694	LMXRB, QPO and BH, hard transient	yes
IGR J17544-2619	268.6053	-26.33128	HMXRB supergiant, hard transient	
IGR J17586-2129	269.6583	-21.32694	X-ray binary	
IGR J17597-2201	269.9404	-22.02750	LMXRB, burster, dipper	yes
GX 5-1	270.2842	-25.07917	LMXRB	yes
GRS 1758-258	270.3029	-25.74056	LMXRB, BH	yes
GX 9+1	270.3846	-20.52889	LMXRB, QPO	yes
IGR J18027-2016	270.6750	-20.28833	HMXRB supergiant, X-ray pulsar	yes
IGR J18027-1455	270.6974	-14.91522	Seyfert galaxy type 1	yes
IGR J18048-1455	271.1623	-14.94647	HMXRB	
SGR 1806-20	272.1638	-20.41097	Gamma-ray source, burst, soft repeater, pulsar	yes
PSR J1811-1926	272.8718	-19.42433	SNR, radio pulsar	
IGR J18134-1636	273.3500	-16.59806	X-ray binary	
IGR J18135-1751	273.3625	-17.84889	SNR	yes
GX 13+1	273.6315	-17.15742	LMXRB, QPO and bursts	yes
4U 1812-12	273.7758	-12.09642	LMXRB, burster	yes
GX 17+2	274.0058	-14.03639	LMXRB, QPO and bursts	yes
IGR J18173-2509	274.3292	-25.15111	X-ray binary	

Table 9.3 continued ...

Source name	RA (J2000) [deg]	DEC (J2000) [deg]	Source type	signif. $> 3\sigma$ $[25 - 60\,\mathrm{keV}]$
SAX J1818.6-1703	274.6579	-17.04664	HMXRB supergiant, hard transient	
AX J1820.5-1434	275.1229	-14.57333	HMXRB Be star, X-ray pulsar, hard transient	yes
IGR J18214-1318	275.3417	-13.30806	X-ray binary, hard transient	yes
IGR J18246-1425	276.1625	-14.41806	X-ray binary, hard transient	
IGR J18256-1035	276.4042	-10.58694	X-ray binary	
IGR J18259-0706	276.4833	-7.106111	X-ray binary	
RX J1826.2-1450	276.5627	-14.84822	HMXRB supergiant, BH	yes
Ginga 1826-24	277.3675	-23.79139	LMXRB, BH	yes
AX J1830.6-1002	277.6625	-10.04500	X-ray binary	yes
IGR J18308-1232	277.6958	-12.53194	X-ray binary	
IGR J18325-0756	278.1167	-7.940000	X-ray binary, hard transient	yes
SNR 021.5-00.9	278.3958	-10.55806	SNR Crab-like, radio pulsar	yes
PKS 1830-211	278.4162	-21.06106	BL Lac	yes
AX J1838.0-0655	279.5083	-6.903889	SNR	yes
IGR J18410-0535	280.2523	-5.596333	HMXRB Be star, hard transient	
AX J1841.3-0455	280.3306	-4.936444	Anomalous X-ray pulsar	yes
IGR J18450-0435	281.2579	-4.566111	HMXRB supergiant, hard transient	yes
PSR J1846-0258	281.6021	-2.974444	SNR, radio pulsar	yes
IGR J18483-0311	282.0625	-3.168889	X-ray binary, hard transient	yes
3A 1845-024	282.0738	-2.420278	HMXRB Be star, X-ray pulsar, hard transient	
IGR J18485-0047	282.1167	-0.778889	X-ray binary	
3A 1850-087	283.2703	-8.705667	LMXRB Globular cluster, burster	yes
XTE J1855-026	283.8804	-2.606667	HMXRB supergiant, X-ray pulsar, hard transient	yes
HETE J1900.1-2455	285.0407	-24.90119	LMXRB, pulsar and bursts, hard transient	
IGR J19048-1240	286.2042	-12.66111	X-ray binary, hard transient	

Table 9.4: *INTEGRAL* sources which are detected (source significance larger than 3σ) in our mosaic with both positions, the one listed in the catalogue and the positions fitted during the analysis.

Name	RA [deg] (J2000)	DEC [deg] (J2000)	$\mathrm{RA_{fitted}}$ [deg]	$\mathrm{DEC_{fitted}}$ [deg]	error in position [deg]
			energy range $25-60\,\mathrm{keV}$		
IGR J17461-2204	266.533	-22.059	266.567	-22.035	0.119
IGR J17476-2253	266.904	-22.887	266.897	-22.866	0.085
GX 3+1	266.983	-26.564	266.999	-26.549	0.044
1RXS J175113.3-20121	267.854	-20.202	267.854	-20.188	0.075
SWIFT J1753.5-0127	268.368	-1.452	268.369	-1.452	0.006
IGR J17597-2201	269.940	-22.028	269.924	-22.021	0.022
GX 5-1	270.284	-25.079	270.284	-25.081	0.009
GRS 1758-258	270.303	-25.741	270.301	-25.744	0.005
GX 9+1	270.385	-20.529	270.403	-20.553	–
IGR J18027-2016	270.675	-20.288	270.670	-20.238	0.023
IGR J18027-1455	270.697	-14.915	270.679	-14.911	0.040
SGR 1806-20	272.164	-20.411	272.163	-20.417	0.028
IGR J18135-1751	273.363	-17.849	273.394	-17.852	0.053
GX 13+1	273.632	-17.157	273.630	-17.153	0.014
4U 1812-12	273.776	-12.096	273.776	-12.095	0.005
GX 17+2	274.006	-14.036	274.006	-14.036	0.006
AX J1820.5-1434	275.123	-14.573	275.108	-14.571	0.033
IGR J18214-1318	275.342	-13.308	275.351	-13.323	0.050
RX J1826.2-1450	276.563	-14.848	276.514	-14.834	0.055
Ginga 1826-24	277.368	-23.791	277.366	-23.797	0.004
AX J1830.6-1002	277.663	-10.045	277.636	-10.045	0.091
IGR J18325-0756	278.117	-7.940	278.117	-7.950	0.033
SNR 021.5-00.9	278.396	-10.558	278.402	-10.570	0.024
PKS 1830-211	278.416	-21.061	278.408	-21.059	0.028
AX J1838.0-0655	279.508	-6.904	279.496	-6.917	0.033
AX J1841.3-0455	280.331	-4.936	280.326	-4.922	0.031
IGR J18450-0435	281.258	-4.566	281.257	-4.563	0.060
PSR J1846-0258	281.602	-2.974	281.626	-2.961	0.048
IGR J18483-0311	282.063	-3.169	282.064	-3.168	0.028
3A 1850-087	283.270	-8.706	283.264	-8.706	0.018
XTE J1855-026	283.880	-2.607	283.879	-2.604	0.014

Table 9.5: Count rates and detection significances of the detected *INTEGRAL* sources in the FoV. For the sources detected in the higher energy band, $60 - 200\,\mathrm{keV}$, the respective values are given.

Name	Count rate [count/s]	Detect. signif.	Count Rate [count/s]	Detect. signif.
	Energy range $25 - 60\,\mathrm{keV}$		Energy range $60 - 200\,\mathrm{keV}$	
IGR J17461-2204	0.122 ± 0.036	3.35		
IGR J17476-2253	0.180 ± 0.037	4.83		
GX 3+1	0.470 ± 0.047	9.98		
1RXS J175113.3-20121	0.170 ± 0.031	5.53		
SWIFT J1753.5-0127	5.560 ± 0.045	122.30	2.572 ± 0.046	55.43
IGR J17597-2201	0.679 ± 0.031	22.07		
GX 5-1	2.587 ± 0.037	70.08		
GRS 1758-258	9.915 ± 0.039	257.38	4.369 ± 0.037	116.79
GX 9+1	0.602	21.54		
IGR J18027-2016	0.575 ± 0.027	21.03		
IGR J18027-1455	0.267 ± 0.024	11.16	0.147 ± 0.024	6.15
SGR 1806-20	0.450 ± 0.027	16.97	0.183 ± 0.026	6.98
IGR J18135-1751	0.191 ± 0.024	8.07		
GX 13+1	0.934 ± 0.023	40.30		
4U 1812-12	4.170 ± 0.022	186.47	1.282 ± 0.023	56.93
GX 17+2	3.687 ± 0.023	163.62	0.162 ± 0.023	7.19
AX J1820.5-1434	0.303 ± 0.022	13.73		
IGR J18214-1318	0.189 ± 0.022	8.64		
RX J1826.2-1450	0.170 ± 0.022	7.72		
Ginga 1826-24	12.297 ± 0.032	383.45	2.751 ± 0.031	87.51
AX J1830.6-1002	0.103 ± 0.023	4.48		
IGR J18325-0756	0.342 ± 0.025	13.93		
SNR 021.5-00.9	0.472 ± 0.023	20.43	0.154 ± 0.023	6.59
PKS 1830-211	0.460 ± 0.028	16.58	0.285 ± 0.027	10.41
AX J1838.0-0655	0.362 ± 0.026	13.81	0.210 ± 0.027	7.87
AX J1841.3-0455	0.434 ± 0.029	14.79	0.313 ± 0.030	10.46
IGR J18450-0435	0.218 ± 0.031	7.05		
PSR J1846-0258	0.317 ± 0.035	9.09		
IGR J18483-0311	0.586 ± 0.035	16.61		
3A 1850-087	0.847 ± 0.029	29.30	0.211 ± 0.029	7.21
XTE J1855-026	1.559 ± 0.041	38.48	0.213 ± 0.041	5.19

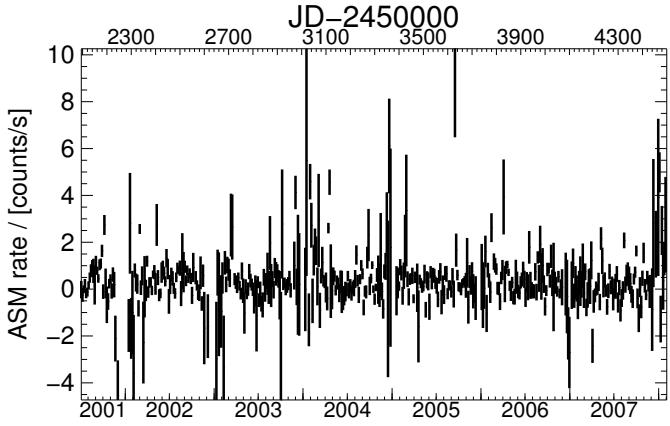

Figure 9.3: RXTE ASM light curve of AX J1820.5−1434.

9.2 AX J1820.5–1434

AX J1820.5−1434 close to LS 5039 is an accreting pulsating neutron star. The spin period of the pulsar is $P_{\rm spin} = 152.26\,{\rm s}$,[3] while the orbital period is not yet known. The pulsar was discovered by Kinugasa et al. (1998). While in the time interval March/April 2003 the source was observed by *INTEGRAL IBIS* with a flux $F(18-60\,{\rm keV}) \approx 8\,{\rm mCrab}$, it was not seen in September/October 2003 (Filippova et al. 2005). Negueruela & Schurch (2007) looked for an optical counterpart for the pulsar, and supposed a mid or early type B-star as possible association, although the transient characteristic suggested that the source could be a Be/X-ray binary.

This source seems to vary in the two phase intervals defined for LS 5039 (Figure 6.1). The light curve of AX J1820.5−1434 reveals that this source was bright in the two time intervals (from MJD = 53839.77 to 53845.94 and from MJD = 53846.01 to 53848.12), which by chance mostly coincide with the phases of the inferior conjunction of RX J1826.2−1450 (respectively LS 5039).

[3] At `http://pulsar.sternwarte.uni-erlangen.de/gps/targettable.cgi` a list of accreting pulsating neutron stars, which were regularly observed in the *INTEGRAL* Galactic plane survey.

CHAPTER 10

Summary & outlook

10.1 LS 5039

The binary system LS 5039 / RX J1826.2−1450 is a mysterious source. The nature of the compact object and the nature of the system are still unknown, although the source has been observed in several energy ranges from the radio to the very high energy γ-ray regime. The observation in the hard X-ray/soft γ-ray energy range, together with observations in other wavelength regimes, can give new insights into the acceleration process of the underlying particle distribution and the radiation processes, which generate the γ-ray emission.

INTEGRAL observations of all public data, including the Galactic plane survey (GPS) and Key Programme data, until October 2007 were analysed. In total, a deep sky image of 3×10^6 s exposure time was created. The analysis of this very crowded field of view (FoV) needed a very careful handling of the Off-line Scientific Analysis (OSA) package and multiple cross-checks. The results obtained were checked, first, in comparison with results obtained with the INAF-Palermo package for the image itself, the light curve and the spectrum. Second, a cross-check was performed between the standard creation of the spectrum, the light curve, and the phaseogram and a spectrum, light curve, and phaseogram produced directly from the mosaics.

After the confirmation of the reliability of the results, the science analysis has been carried out. The data set was split into two parts depending on the orbital phase interval. The two orbital phase intervals, defined on the basis of the *H.E.S.S.* observations by Aharonian et al. (2006c), split the orbital cycle into the part around inferior conjunction (INFC) and around superior conjunction (SUPC). A period search on the light curve was performed. The light curve was folded with the orbital period taken from Casares et al. (2005b) into

phaseograms. A search for a possible correlation of the flux modulation with the variability of the TeV flux observed by *H.E.S.S.* was performed. The main results of this analysis are:

- The source is clearly detected at a significance level of $7.7\,\sigma$ in the energy band of $25 - 60\,\mathrm{keV}$ by *INTEGRAL*.
- For INFC, a flux rate of $(3.54 \pm 2.30) \times 10^{-11}\,\mathrm{erg\,cm^{-2}\,s^{-1}}$ within the 90 % confidence level is determined.
- For SUPC, an upper flux limit of $1.45 \times 10^{-12}\,\mathrm{erg\,cm^{-2}\,s^{-1}}$ within the 90 % confidence level is calculated.
- The period search on the light curve reveals no clear period, but an epoch folding of the light curve reveals a peak at $P_{\mathrm{orb}} = 3.906\,\mathrm{d}$. This is the same position, which Casares et al. (2005b) and Aragona et al. (2009) determine by optical radial velocity measurements.
- Folding the light curve with this orbital period, reveals a clear modulation with the orbital period of the hard X-ray energy emission in the energy range from $25\,\mathrm{keV}$ up to $200\,\mathrm{keV}$.
- A spectrum for the INFC phase interval is extracted and fitted with a power-law model with absorption. The photon index is $\Gamma = 2.0 \pm 0.2$.
- The modulation of the hard X-ray flux found with *INTEGRAL* is in correlation with the TeV emission found by *H.E.S.S.*.

In addition, the detected modulation in the hard X-ray range was verified by comparison with the behaviour of other nearby sources. The reference sources show no modulation with the orbital period of LS 5039. The correlation between hard X-ray and TeV emission was later confirmed by observations of *Suzaku* (Takahashi et al. 2009).

Our result lead to the two main conclusions:

1. The explanation of absorption as the only reason for the TeV emission modulation is not applicable. An alternative explanation is that the correlated modulation is caused by adiabatic cooling of the electrons and is then simply a result of the orbital motion. Additional

processes like photon-photon absorption and anisotropic IC scattering can enhance the TeV modulation up to the magnitude which is observed.

2. No final conclusions are possible on the nature of the compact object as well as on the nature of the entire system.

To solve these questions, further observations, simultaneously performed in the keV to TeV energy range with instruments like *Suzaku*, Fermi-GLAST, and *H.E.S.S.* are necessary.

10.2 TeV plerions

Amongst the sources seen in very high γ-rays, several are associated with Pulsar Wind Nebulae. The study of hard X-ray/soft gamma-ray emission is providing an important insight into the energetic particle population present in these objects.

Two mosaics of public *INTEGRAL* data of known TeV plerions detected by ground based Čherenkov telescopes were generated. The first contained the pulsar wind nebulae named Kookaburra and MSH 15−52 and had an exposure time of 940 ks. The second mosaic had an exposure time of 1.3 Ms and included the region around the Vela pulsar. The main aim of the analysis was the search for a possible correlation between *INTEGRAL* and *H.E.S.S.* sources.

The main results of this analysis are:

- The analyses indicate a deeper link between these TeV plerions and *INTEGRAL* detected pulsar wind nebulae.
- The TeV plerion in the northern wing of the Kookaburra region, which is G313.3+0.6 powered by the middle-aged PSR J1420−6048, is found to have a previously unknown *INTEGRAL* counterpart. This is, apart from the Vela pulsar, the only middle-aged pulsar detected with *INTEGRAL*.
- For the TeV plerion associated with the X-ray pulsar wind nebula "Rabbit" (G313.3+0.1), no *INTEGRAL* counterpart is found. This pulsar wind nebula is possibly powered by a young pulsar.

To confirm a possible link between VHE γ-ray and *INTEGRAL* observations of TeV plerions a larger methodical study is necessary.

10.3 AX J1820.5–1434

The analysis of the crowded FoV of LS 5039 provides light curves and spectra as byproducts for several interesting sources. One of these sources is the accreting pulsar AX J1820.5−1434. This source is an accreting pulsating neutron star with a yet unknown orbital period. AX J1820.5−1434 strikes the eye, because this source also appears to be modulated, when splitting the data set into the two phase intervals described above. To verify the flux dependence on the orbital phase of LS 5039, the RXTE ASM light curve of AX J1820.5−1434 has been studied.

The results of this analysis are:

- AX J1820.5−1434 was only bright in two time intervals during the total of 3 Ms of the *INTEGRAL* observation.
- These intervals correspond by chance with the INFC phase interval of LS 5039, hence, the source apparently shows the same modulation as LS 5039.

Further *INTEGRAL* studies on this source is desirable. The produced *INTEGRAL* FoV provides interesting information, especially a long timing baseline, on many sources. To look at the *INTEGRAL* observations of these sources in detail is worthwhile, too.

BIBLIOGRAPHY

Abdo, A. A., Ackermann, M., Ajello, M., et al. 2009a, ApJS, 183, 46

Abdo, A. A., Ackermann, M., Ajello, M., et al. 2009b, ApJ, 701, L123

Acciari, V. A., Aliu, E., Arlen, T., et al. 2009, ApJ, 698, L94

Achterberg, A., Gallant, Y. A., Kirk, J. G., Guthmann, A. W. 2001, MNRAS, 328, 393

Aharonian, F., Akhperjanian, A. G., Aye, K.-M., et al. 2005a, Science, 307, 1938

Aharonian, F., Akhperjanian, A. G., Aye, K.-M., et al. 2005b, Science, 309, 746

Aharonian, F., Akhperjanian, A. G., Aye, K.-M., et al. 2005c, A&A, 442, 1

Aharonian, F., Akhperjanian, A. G., Aye, K.-M., et al. 2005d, A&A, 435, L17

Aharonian, F., Akhperjanian, A. G., Barres de Almeida, U., et al. 2008a, A&A, 477, 353

Aharonian, F., Akhperjanian, A. G., Bazer-Bachi, A. R., et al. 2008b, A&A, 481, 401

Aharonian, F., Akhperjanian, A. G., Bazer-Bachi, A. R., et al. 2007, A&A, 472, 489

Aharonian, F., Akhperjanian, A. G., Bazer-Bachi, A. R., et al. 2006a, A&A, 448, L43

Aharonian, F., Akhperjanian, A. G., Bazer-Bachi, A. R., et al. 2006b, ApJ, 636, 777

Aharonian, F., Akhperjanian, A. G., Bazer-Bachi, A. R., et al. 2006c, A&A, 460, 743

Aharonian, F., Akhperjanian, A. G., Bazer-Bachi, A. R., et al. 2006d, A&A, 456, 245

Aharonian, F., Akhperjanian, A. G., Bazer-Bachi, A. R., et al. 2006e, A&A, 460, 365

Aharonian, F., Anchordoqui, L., Khangulyan, D., Montaruli, T. 2006f, Journal of Physics Conference Series, 39, 408

Aharonian, F. A. 2004, Very High Energy Cosmic Gamma Radiation – A Crucial Window on the Extreme Universe (New Jersey London Singapore Beijing Shanghai Hong Kong Taipei Chennai: World Scientific Publishing Co. Pte. Ltd.)

Aharonian, F. A., Akhperjanian, A. G., Bazer-Bachi, A. R., et al. 2005e, A&A, 442, L25

Aharonian, F. A., Atoyan, A. M. 1998, New Astronomy Review, 42, 579

Aharonian, F. A., Bogovalov, S. V. 2003, New Astronomy, 8, 85

Albert, J., Aliu, E., Anderhub, H., et al. 2006, Science, 312, 1771

Albert, J., Aliu, E., Anderhub, H., et al. 2007, ApJ, 665, L51

Aragona, C., McSwain, M. V., Grundstrom, E. D., et al. 2009, ApJ, 698, 514

Arnaud, K. A. 1996, in Astronomical Data Analysis Software and Systems V, ed. G. H. Jacoby and J. Barnes, Astronomical Society of the Pacific Conference Series, 101, 17

Arons, J., Tavani, M. 1994, ApJS, 90, 797

Bednarek, W. 1997, A&A, 322, 523

Bednarek, W. 2006, MNRAS, 368, 579

Bernlöhr, K. 2000, Astroparticle Physics, 12, 255

Bird, A. J., Barlow, E. J., Bassani, L., et al. 2006, ApJ, 636, 765

Bird, A. J., Malizia, A., Bazzano, A., et al. 2007, ApJS, 170, 175

Blondin, J. M., Chevalier, R. A., Frierson, D. M. 2001, ApJ, 563, 806

Blumenthal, G. R., Gould, R. J. 1970, Reviews of Modern Physics, 42, 237

Bogovalov, S. V., Khangulyan, D. V., Koldoba, A. V., Ustyugova, G. V., Aharonian, F. A. 2008, MNRAS, 387, 63

Bondi, H. 1952, MNRAS, 112, 195

Bondi, H., Hoyle, F. 1944, MNRAS, 104, 273

Bosch-Ramon, V., Khangulyan, D., Aharonian, F. 2008, ArXiv e-prints, (astro-ph:0810.4494v1)

Bosch-Ramon, V., Paredes, J. M. 2004, A&A, 417, 1075

Bosch-Ramon, V., Paredes, J. M., Ribó, M., et al. 2005, ApJ, 628, 388

Böttcher, M. 2007, Astroparticle Physics, 27, 278

Bradt, H. 2008, Astrophysics Processes – The Physic of Astronomial Phenomena (Cambridge New York: Cambridge University Press)

Bridle, A. H., Perley, R. A. 1984, ARA&A, 22, 319

Casares, J., Ribas, I., Paredes, J. M., Martí, J., Allende Prieto, C. 2005a, MNRAS, 360, 1105

Casares, J., Ribó, M., Ribas, I., et al. 2005b, MNRAS, 364, 899

Charles, P. A., Seward, F. D. 1995, Exploring the X-ray Universe (Cambridge: Cambridge University Press)

Clark, J. S., Reig, P., Goodwin, S. P., et al. 2001, A&A, 376, 476

Collmar, W. 2004, in Proceedings of The fourth AGILE Science Workshop: X-ray and gamma-ray astrophysics of galactic sources

Combi, J. A., Cellone, S. A., Martí, J., et al. 2004, A&A, 427, 959

Conti, P. S. 1978, A&A, 63, 225

de Naurois, M. 2007, Ap&SS, 309, 277

Dhawan, V., Mioduszewski, A., Rupen, M. 2006, in VI Microquasar Workshop: Microquasars and Beyond

Distefano, C., Guetta, D., Waxman, E., Levinson, A. 2002, ApJ, 575, 378

Döring, M., Bernlöhr, K., Hermann, G., Hofmann, W., Lampeitl, H. 2001, ArXiv Astrophysics e-prints, (astro-ph:0107149v2)

Dubus, G. 2006, A&A, 456, 801

Dubus, G. 2008, New Astronomy Review, 51, 778

Dubus, G., Cerutti, B., Henri, G. 2008, A&A, 477, 691

Esposito, P., Caraveo, P. A., Pellizzoni, A., et al. 2007, A&A, 474, 575

Farrell, S. A., Sood, R. K., O'Neill, P. M., Dieters, S. 2008, MNRAS, 389, 608

Fermi, E. 1949, Physical Review, 75, 1169

Filippova, E. V., Tsygankov, S. S., Lutovinov, A. A., Sunyaev, R. A. 2005, Astronomy Letters, 31, 729

Fritz, S. 2008, PhD thesis, (University of Tübingen)

Georganopoulos, M., Aharonian, F. A., Kirk, J. G. 2002, A&A, 388, L25

Giacconi, R., Gursky, H., van Speybroeck, L. P. 1968, ARA&A, 6, 373

Ginzburg, V. L., Syrovatskii, S. I. 1965, ARA&A, 3, 297

Goldoni, P., Ribó, M., di Salvo, T., et al. 2007, Ap&SS, 309, 293

Goldwurm, A., David, P., Foschini, L., et al. 2003, A&A, 411, L223

Goldwurm, A., Goldoni, P., Gros, A., et al. 2001, in Exploring the Gamma-Ray Universe, ed. A. Gimenez, V. Reglero, and C. Winkler, ESA Special Publication, 459, 497

Gottesman, S. R., Fenimore, E. E. 1989, Appl. Opt., 28, 4344

Grove, J. E., Tavani, M., Purcell, W. R., et al. 1995, ApJ, 447, L113+

Grupen, C. 2000, Astroteilchenphysik – Das Universum im Licht der kosmischen Strahlung (Braunschweig/Wiesbaden: Vieweg Verlag)

Harding, A. K., Lai, D. 2006, Reports on Progress in Physics, 69, 2631

Harmon, B. A., Wilson, C. A., Fishman, G. J., et al. 2004, ApJS, 154, 585

Hartman, R. C., Bertsch, D. L., Bloom, S. D., et al. 1999, ApJS, 123, 79

Heinz, S., Sunyaev, R. 2002, A&A, 390, 751

Heitler, W. 1954, Quantum theory of radiation, 3rd edn. (Oxford: Clarendon)

Hinton, J. A., Skilton, J. L., Funk, S., et al. 2009, ApJ, 690, L101

Hoffmann, A. I. D., Horns, D., Santangelo, A. 2007, Ap&SS, 309, 215

Hoffmann, A. I. D., Klochkov, D., Santangelo, A., et al. 2009, A&A, 494, L37

Hofmann, W., The H. E. S. S. Collaboration. 2001, in International Cosmic Ray Conference, International Cosmic Ray Conference, 7, 2785

Horns, D., Aharonian, F., Santangelo, A., Hoffmann, A. I. D., Masterson, C. 2006, A&A, 451, L51

Hoshino, M., Arons, J., Gallant, Y. A., Langdon, A. B. 1992, ApJ, 390, 454

Howarth, I. D., Prinja, R. K. 1989, ApJS, 69, 527

Jogler, T., Puchades, N., Blanch Bigas, O., et al. 2009, ArXiv e-prints, (astro-ph:0907.0992)

Kaler, J. 1994, Sterne und ihre Spektren (Heidelberg Berlin Oxford: Spektrum Akademischer Verlag)

Kaper, L. 2001, in The Influence of Binaries on Stellar Population Studies, ed. D. Vanbeveren, Astrophysics and Space Science Library, 264, 125

Karttunen, H., Kröger, P., Oja, H., Poutaneu, M., Donner, K. 2007, Fundamental Astronomy, 5th edn. (Berlin: Springer Verlag)

Kaufman Bernadó, M. M., Romero, G. E., Mirabel, I. F. 2002, A&A, 385, L10

Kawachi, A., Naito, T., Patterson, J. R., et al. 2004, ApJ, 607, 949

Khangulyan, D., Aharonian, F. 2005, in High Energy Gamma-Ray Astronomy, ed. F. A. Aharonian, H. J. Völk, and D. Horns, American Institute of Physics Conference Series, 745, 359

Khangulyan, D., Aharonian, F., Bosch-Ramon, V. 2008a, MNRAS, 383, 467

Khangulyan, D., Hnatic, S., Aharonian, F., Bogovalov, S. 2007, MNRAS, 380, 320

Khangulyan, D. V., Aharonian, F. A., Bogovalov, S. V., Koldoba, A. V., Ustyugova, G. V. 2008b, International Journal of Modern Physics D, 17, 1909

Kinugasa, K., Torii, K., Hashimoto, Y., et al. 1998, ApJ, 495, 435

Kirk, J. G., Ball, L., Skjaeraasen, O. 1999, Astroparticle Physics, 10, 31

Kirk, J. G., Schneider, P. 1987, ApJ, 315, 425

Klapdor-Kleingrothaus, H. V., Zuber, K. 1997, Teilchenastrophysik (Stuttgart: B.G. Teubner)

Kretschmar, P., Wilms, J., Staubert, R., Kreykenbohm, I., Heindl, W. A. 2004, in 5th INTEGRAL Workshop on the INTEGRAL Universe, ed. V. Schoenfelder, G. Lichti, and C. Winkler, ESA Special Publication, 552, 329

Leahy, D. A. 2002, A&A, 391, 219

Lebrun, F., Leray, J. P., Lavocat, P., et al. 2003, A&A, 411, L141

Lemoine, M., Pelletier, G., Revenu, B. 2006, ApJ, 645, L129

Liu, Q. Z., Yan, J. Z., Li, X. D., Hang, H. R. 2006, Ap&SS, 305, 133

Longair, M. S. 1992, High Energy Astrophysics, Vol. 1: Particles, Photons, and their Detection, 2nd edn. (Cambridge University Press)

Longair, M. S. 1994, High Energy Astrophysics, Vol. 2: Stars, the Galaxy and the interstellar medium, 2nd edn. (Cambridge University Press)

Lund, N., Budtz-Jørgensen, C., Westergaard, N. J., et al. 2003, A&A, 411, L231

Manchester, R. N., Hobbs, G. B., Teoh, A., Hobbs, M. 2005, AJ, 129, 1993

Maraschi, L., Treves, A. 1981, MNRAS, 194, 1P

Martí, J., Luque-Escamilla, P., Garrido, J. L., Paredes, J. M., Zamanov, R. 2004, A&A, 418, 271

Marti, J., Paredes, J. M., Ribo, M. 1998, A&A, 338, L71

Martocchia, A., Motch, C., Negueruela, I. 2005, A&A, 430, 245

Mas-Hesse, J. M., Giménez, A., Culhane, J. L., et al. 2003, A&A, 411, L261

Masterson, C., et al. 2005, in International Cosmic Ray Conference, International Cosmic Ray Conference, 4, 143

McSwain, M. V., Gies, D. R. 2002, ApJ, 568, L27

McSwain, M. V., Gies, D. R., Huang, W., et al. 2004, ApJ, 600, 927

McSwain, M. V., Gies, D. R., Riddle, R. L., Wang, Z., Wingert, D. W. 2001, ApJ, 558, L43

Mirabel, I. F. 2007, Ap&SS, 309, 267

Mirabel, I. F., Rodríguez, L. F. 1994, Nature, 371, 46

Mirabel, I. F., Rodríguez, L. F. 1999, ARA&A, 37, 409

Mirabel, I. F., Rodriguez, L. F., Cordier, B., Paul, J., Lebrun, F. 1992, Nature, 358, 215

Moderski, R., Sikora, M., Coppi, P. S., Aharonian, F. 2005, MNRAS, 363, 954

Moldon, J., Ribo, M., Paredes, J. M., Marti, J., Massi, M. 2009, ArXiv e-prints, (astro-ph:0902.3866)

Morris, D. J., Hobbs, G., Lyne, A. G., et al. 2002, MNRAS, 335, 275

Motch, C., Haberl, F., Dennerl, K., Pakull, M., Janot-Pacheco, E. 1997, A&A, 323, 853

Nagae, O., Kawabata, K. S., Fukazawa, Y., et al. 2009, AJ, 137, 3509

Negueruela, I., Schurch, M. P. E. 2007, A&A, 461, 631

Neronov, A., Chernyakova, M. 2007, Ap&SS, 309, 253

Ng, C.-Y., Roberts, M. S. E., Romani, R. W. 2005, ApJ, 627, 904

Niemiec, J., Ostrowski, M. 2006, ApJ, 641, 984

Ostrowski, M. 1991, MNRAS, 249, 551

Paredes, J. M., Bosch-Ramon, V., Romero, G. E. 2006, A&A, 451, 259

Paredes, J. M., Martí, J., Ribó, M., Massi, M. 2000, Science, 288, 2340

Paredes, J. M., Ribó, M., Ros, E., Martí, J., Massi, M. 2002, A&A, 393, L99

Perucho, M., Bosch-Ramon, V. 2008, A&A, 482, 917

Puls, J., Kudritzki, R.-P., Herrero, A., et al. 1996, A&A, 305, 171

Puls, J., Urbaneja, M. A., Venero, R., et al. 2005, A&A, 435, 669

Rees, M. J., Gunn, J. E. 1974, MNRAS, 167, 1

Reig, P., Ribó, M., Paredes, J. M., Martí, J. 2003, A&A, 405, 285

Reynolds, S. P. 1982, ApJ, 256, 13

Ribó, M., Paredes, J. M., Romero, G. E., et al. 2002, A&A, 384, 954

Ribó, M., Reig, P., Martí, J., Paredes, J. M. 1999, A&A, 347, 518

Rieger, F. M., Bosch-Ramon, V., Duffy, P. 2007, Ap&SS, 309, 119

Roberts, M. S. E., Romani, R. W., Johnston, S., Green, A. J. 1999, ApJ, 515, 712

Romero, G. E., Torres, D. F., Kaufman Bernadó, M. M., Mirabel, I. F. 2003, A&A, 410, L1

Romero, G. E., Vila, G. S. 2008, A&A, 485, 623

Rosswog, S., Brüggen, M. 2007, Introduction to High-Energy Astrophysics (Cambridge: Cambridge University Press)

Rothschild, R. E., Blanco, P. R., Gruber, D. E., et al. 1998, ApJ, 496, 538

Rybicki, G. B., Lightman, A. P. 1979, Radiative Processes in Astrophysics (New York Chichester Brisbane Toronto: A Wiley – interscience publication, John Wiley & sons)

Saito, T. Y., Zanin, R., Bordas, P., et al. 2009, ArXiv e-prints, (astro-ph:0907.1017)

Santolaya-Rey, A. E., Puls, J., Herrero, A. 1997, A&A, 323, 488

Schoenfelder, V., Aarts, H., Bennett, K., et al. 1993, ApJS, 86, 657

Schönfelder, V., Bennett, K., Blom, J. J., et al. 2000, A&AS, 143, 145

Segreto, A., Ferrigno. 2006, in Proc. of the 6th *INTEGRAL* Workshop 'The Obscured Universe', Moscow on 2-8 July 2006, ed. S. Grebenev, R. Sunyaev, and C. Winkler, p.633

Shu, F. H. 1991, The Physics of Astrophysics, I. Radiation (Mill Valley, CA: University Science Books)

Sierpowska-Bartosik, A., Bednarek, W. 2008, MNRAS, 385, 2279

Sierpowska-Bartosik, A., Torres, D. F. 2007, ApJ, 671, L145

Spitkovsky, A. 2005, in Astrophysical Sources of High Energy Particles and Radiation, ed. T. Bulik, B. Rudak, and G. Madejski, American Institute of Physics Conference Series, 801, 345

Stephenson, C. B., Sanduleak, N. 1971, Publications of the Warner & Swasey Observatory, 1, 1

Stöker, H. 2000, Taschenbuch der Physik, 4th edn. (Thun Frankfurt am Main: Verlag Harri Deutsch)

Strong, A. W., Collmar, W., Bennett, K., et al. 2001, in Gamma 2001: Gamma-Ray Astrophysics, ed. S. Ritz, N. Gehrels, and C. R. Shrader, American Institute of Physics Conference Series, 587, 21

Sturner, S. J., Skibo, J. G., Dermer, C. D., Mattox, J. R. 1997, ApJ, 490, 619

Takahashi, T., Kishishita, T., Uchiyama, Y., et al. 2009, ApJ, 697, 592

Tauris, T. M., van den Heuvel, E. 2003, ArXiv Astrophysics e-prints, (astro-ph/0303456)

Tavani, M., Arons, J. 1997, ApJ, 477, 439

Ubertini, P., Lebrun, F., Di Cocco, G., et al. 2003, A&A, 411, L131

Uchiyama, Y., Tanaka, T., Takahashi, T., Mori, K., Nakazawa, K. 2009, ApJ, 698, 911

Unsöld, A., Baschek, B. 1999, Der neue Kosmos – Einführung in die Astronomie und Astrophysik, 6th edn. (Berlin Heidelberg New York: Springer Verlag)

Vedrenne, G., Roques, J.-P., Schönfelder, V., et al. 2003, A&A, 411, L63

Voges, W., Aschenbach, B., Boller, T., et al. 1999, A&A, 349, 389

Weekes, T. C. 1992, Space Science Reviews, 59, 315

Weekes, T. C., Cawley, M. F., Fegan, D. J., et al. 1989, ApJ, 342, 379

White, N. E., Swank, J. H. 1984, ApJ, 287, 856

Winkler, C. 2001, in Exploring the Gamma-Ray Universe, ed. A. Gimenez, V. Reglero, and C. Winkler, ESA Special Publication, 459, 471

Winkler, C., Courvoisier, T. J.-L., Di Cocco, G., et al. 2003, A&A, 411, L1

Wolter, H. 1952a, Annalen der Physik, 445, 94

Wolter, H. 1952b, Annalen der Physik, 445, 286

Zdziarski, A. A., Neronov, A., Chernyakova, M. 2008, ArXiv e-prints, (astro-ph:0802.1174)

ACKNOWLEDGEMENTS

Many people have helped me and accompanied me during the last years, and I'd like to thank them.

First of all, I'd like to thank Andrea Santangelo for advice, supervision, and motivation during the working for and writing of this thesis.

Further thanks go to Rüdiger Staubert for being the "backup" professor and to Dima Klochkov for their help with the period searching stuff.

Gerd Pühlhofer and Dieter Horns, I'd like to thank for their helping and for constructive discussions.

Handling and understanding the OSA and using some tricks would not have been possible without the help of Ingo Kreykenbohm, Sonja Fritz, and Jörn Wilms. I would like to thank, in addition, Laura Barragan for her altruistic help with the *Suzaku* analysis and the Bamberg group for their kindness during my one week visit.

I thank all my colleagues at the IAAT, who created a social atmosphere, which was productive and characterised by mutual respect and friendship.
I'd like to name and thank a few of them in particular:
– Sonja Fritz for her help, the discussions and many other things,
– Elke Reiff and Dorothee Jahn for the shelter in A207,
– Stefan Schwarzburg for the time we spent together in the *H.E.S.S.* Collaboration, in particular several Collaboration meetings, and for his desk on loan for two and a half weeks,
– Thorsten Nagel for his sympathetic ear during many 11 pm tea breaks, and
– Michael Martin for sharing the motivation during the last weeks of writing.

A special thank to the "AIT branch office" in Göttingen to Sonja Schuh and Iris Traulsen for all answered questions, discussions, style files, accommodation during my stays, the proofreading and many, many other things.

I'd like to thank with all my heart my "english aunt" Gail Vickers for proofreading and for going through all the "complicated" astrophysical stuff.

Last but not least, I want to thank my family. My parents have assisted me until today and have let my dream come true. I'd like to thank also my sisters and brothers-in-law – Regine and Matthias, Edith and Patrick – for the many motivating words. Thanks for your love and support. Thanks that you are there!

This work was supported by the Deutsches Zentrum für Luft- und Raumfahrt (DLR) under grant number 50OR0302. This work is based on observations with *INTEGRAL*, an European Space Agency (ESA) project with instruments and science data centre funded by ESA member states (especially the PI countries: Denmark, France, Germany, Italy, Switzerland, Spain), Czech Republic and Poland, and with the participation of Russia and the USA.

CURRICULUM VITAE

17.08.1979	geboren in Solingen
1985 – 1989	Grundschule: Dorfschule Reutlingen-Ohmenhausen
Sept. 1989 – Juni 1998	Friedrich-List-Gymnasium Reutlingen
1998	Abitur
1998 – 2005	Eberhard-Karls-Universität Tübingen, Studium der Physik
26.03.2001	Vordiplom
2000 – 2004	wissenschaftliche Hilfskraft am Institut für Astronomie und Astrophysik, Universität Tübingen
Dez. 2003 – März 2005	Diplomarbeit unter Anleitung von Prof. Klaus Werner 'Eisengruppenelemente in heißen wasserstoffreichen Zentralsternen Planetarischer Nebel'
30.04.2005	Diplom
Juni 2005 – März 2009	wissenschaftliche Angestellte, IAAT
Sept. 2005 – Sept. 2009	Anfertigung der Dissertation mit dem Titel 'Analysis of hard X-ray emission from selected very high energy γ-ray sources observed with INTEGRAL' an der Universität Tübingen, IAAT, Abt. Astronomie, unter Anleitung von Herrn Prof. Dr. A. Santangelo

Meine wichtigsten akademischen Lehrer waren die folgenden Professoren und Dozenten:

Astronomie und Astrophysik : S. Dreizler, J. Frauendiener, E. Kendziorra, W. Kley, U. Kraus, H. Ruder, A. Santangelo, R. Staubert, K. Werner, J. Wilms

Experimentalphysik : H. Clement, F. Gönnenwein, P. Grabmayr, O. Lutz, R. Kleiner, A. Schwenk, G. Wagner, D. Wharam, C. Zimmermann

Chemie: E. Lindner

Informatik : W. Küchlin

Mathematik : H. Fischer, H. Kaul

Theoretische Physik : A. Fäßler, T. Gutsche, H. Müther